A FUNDAMENTAL STUDY OF MINI-TURBINE BLADES FOR URBAN APPLICATIONS

A Thesis

Presented to the Faculty of the Graduate School

of Cornell University

in Partial Fulfillment of the Requirements for the Degree of

Master of Science in Mechanical Engineering

Stacey Chan

January 2014

Abstract

Urban environments contain high densities of wind energy that are inaccessible to large wind turbines of the classical “windmill” design. By exploring small-scale vertical-axis wind turbines (VAWTs), wind energy can possibly be harvested from the constrained spaces within cities.

A thorough and detailed investigation of offset pitch angle, relative blade size, camber, thickness, and sweepback angle for straight blades was done in a wind tunnel. Mini-turbines with chordlength to diameter ratios (c/D) equivalent to commercial VAWTs do ***not*** operate at the small scales of mini-turbines. On the other hand, mini-turbines with large c/D produce the most power. The standard NACA 0015 straight blade with zero offset pitch angle produces the highest coefficient of power, C_P. Adding sweepback reduces C_P but improves self-starting capability. Other unconventional designs and numerical models are investigated.

Although the design and behavior of large-scale VAWTs has been documented in previous literature, mini-turbines show significantly different properties which indicate promise for practical application in the urban environment.

Biographical Sketch

S. Chan received her Bachelor of Science in Mechanical Engineering degree from The University of Texas at Austin in May 2011. She proceeded to enroll in the graduate school program at Cornell University in August 2011.

Chan is a Clare Boothe Luce graduate research fellow, receiving four semesters of funding from the generous Clare Boothe Luce Program of the Henry Luce Foundation. The project was funded in part by the Cornell University David R. Atkinson Center for a Sustainable Future (ACSF) and Engineering Learning Initiatives. Chan won 1st place in the 2013 Trustee Council Annual Meeting ACSF sustainability poster and oral competition. She is an Engineer-In-Training and a LEED Green Associate.

Chan presented her work at the 2013 American Physical Society Division of Fluid Dynamics conference in Pittsburgh, Pennsylvania.

Acknowledgements

I would like to thank my adviser Professor Charles “Skipper” Williamson for his constant guidance and mentorship throughout this project. An additional thank you goes to Professor Edwin “Todd” Cowen for collaborating on the project and being a member of my committee. I also thank my labmates Dan Asselin, Riley Shutt, and Andrew Mackowski for their support in various laboratory and graduate school aspects.

Special thanks go to Jesse Greene, Mike Romanko, Masaki Endo, and Natali Vannoy for their collaboration, dedication, and enthusiasm on this project. I could not have asked for better undergraduates to work with.

Personal thanks go to my close family and friends who have supported me throughout my entire degree program.

Finally, this project would not have been possible without the support from the Clare Boothe Luce Program, Engineering Learning Initiatives, and the David R. Atkinson Center for a Sustainable Future. I am grateful to you all.

Table of Contents

1. Introduction

1.1 Layout of Thesis

This thesis contains some fundamental work on the design and experimentation of mini-turbines. Section 1 of this thesis gives a background on the history of wind turbines, the motivation for this project, and a literature review of the field. Section 2 describes the experimental methods and designs of mini-turbines tested. The results of the experiments are discussed in Sections 3-7, and some numerical modeling tools are described in Section 8. Finally, the thesis concludes with Section 9.

1.2 Vertical-Axis and Horizontal-Axis wind turbines

Wind turbines were first used by ancient Persians, utilizing a vertical-axis wind turbine (VAWT) for grinding grain (MacPhee & Beyene 2012). Horizontal-axis wind turbines (HAWTs) were not made until the Middle Ages and were used to pump water and grind grain (Eriksson et al 2008). Generating electricity from wind turbines was developed in Europe first and slowly made its way to the US for the small rural communities that were not yet connected to the grid. However, the energy crisis in the 1970s caused a big push for wind and other renewable technology, culminating into the large HAWTs that are widespread today (Hau 2006). HAWTs are well-established and current research is focused on the arrangement of wind farms, rather than the individual turbine.

In the 1970s, VAWTs were being developed simultaneously with HAWTs among various groups in the US and Canada (Eriksson et al 2008). Several theories account for the decline of VAWT development: the poor wind power market, issues with structural and bearing loading,

and random selection between HAWTs and VAWTs (MacPhee & Beyene 2012, Eriksson et al 2008).

Today, the wind energy industry has accelerated once again due to the political campaign to meet 20% of the US power needs by wind power by 2030 (DOE 2008). The need to diversify the energy sector, as well as curb climate change, has caused the resurgence of vertical-axis wind turbine research. Mid-sized VAWTs are attempting to find a niche in urban areas where large HAWTs are impractical, dangerous, and an eyesore. VAWTs have several advantages over HAWTs, including:

- Omni-directionality
- Operation in turbulent winds
- Less noise
- Easier maintenance
- Safer for birds and bats

VAWTs are able to accept wind from any direction without a yawing mechanism, as illustrated in Figure 1.1. They also respond to varying and turbulent winds better than HAWTs (MacPhee & Beyene 2012). Acoustic noise from wind turbines come from two sources: aerodynamic and mechanical. The aerodynamic noise is directly related to the speed of the blades. VAWTs typically rotate at speeds half of that as HAWTs, thus reducing the acoustic effects. Mechanical noise comes from the gearbox and drivetrain components, and is lessened by being near or on the ground level in VAWT designs. Having the mechanical components on the ground also makes maintenance much easier and safer than climbing a hundred meters to the hub of an HAWT. Slower blade speeds also correlates to fewer bird and bat collisions (Eriksson et al 2008).

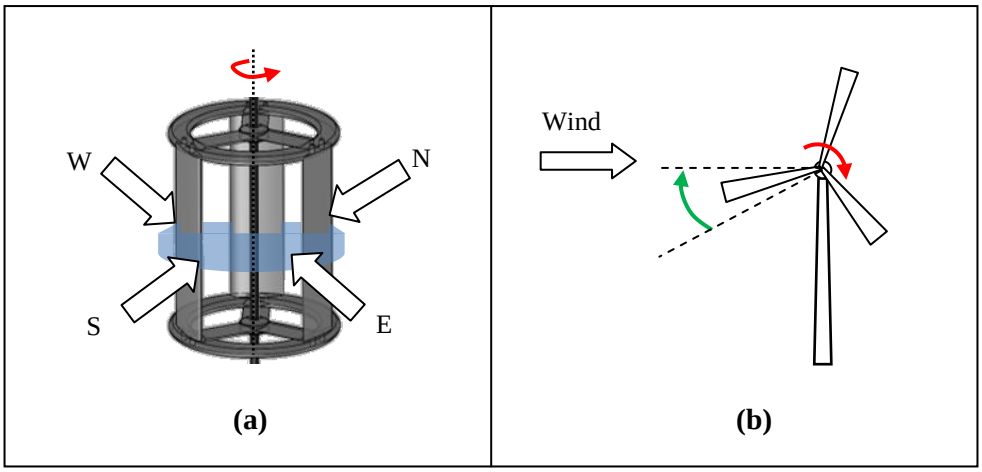

Figure 1.1: (a) VAWTs are omni-directional while
(b) HAWTs must yaw to align themselves in the wind.

Turbines of different designs are compared by their efficiencies. The efficiency of a wind turbine is designated as the coefficient of power, C_P, which is the ratio of actual power to available power in the wind as follows:

$$C_P = \frac{actual\ power}{power\ in\ wind} = \frac{P_{mech}}{\frac{1}{2}\rho U^3 A} \tag{1.1}$$

where P_{mech} is the mechanical power extracted, ρ is the density of the wind, U is the freestream wind velocity, and A is the projected area that the wind intersects. The efficiency of a turbine cannot equal 100%, as that would imply that all the kinetic wind energy comes to a stop and the rotor no longer rotates. Betz (1966) determined the maximum ideal efficiency of a simple rotor disc (such as Figure 1.2) to be 59%. This is the theoretical limit for extracting energy from the wind. Key points of the derivation will be described here, but a full description can be found in Appendix A.

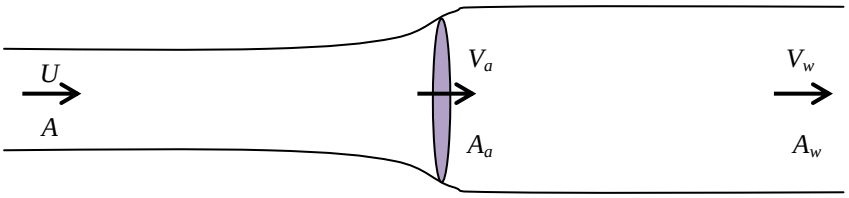

Figure 1.2. Rotor disc for deriving Betz limit

Mass continuity describes the relationship between the upstream velocity U, the downstream velocity in the wake V_w, and the velocity through the actuator disc V_a as follows:

$$UA = V_a A_a = V_w A_w \tag{1.2}$$

The cross-sectional area increases from upstream to downstream of the turbine because in order for the turbine to extract energy, the wind energy and wind velocity must decrease. Analysis of the force and power of the system indicates that the velocity through the rotor disc V_a is the average of the freestream and wake velocity as shown in Equation 1.3 below.

$$V_a = \frac{1}{2}(U + V_w) \tag{1.3}$$

An equation of power in terms of the wake velocity V_w can be formed from a control volume analysis and/or finding the difference between the rate of change of kinetic energies upstream and downstream of the disc. Differentiating the power equation with respect to V_w and setting the derivative to zero (as in Equation 1.4) will give the V_w for maximum power.

$$\frac{dP}{dV_w} = \frac{1}{4}\,\rho A\,(U^2 - \,2UV_w - \,3V_w^2) = 0 \tag{1.4}$$

The maximum occurs when $V_w = 1/3\ U$. Substituting this value into the power equation gives the Betz coefficient of power limit of 59%. Figure 1.3 compares the C_P's of a typical HAWT and a typical VAWT to the Betz efficiency limit.

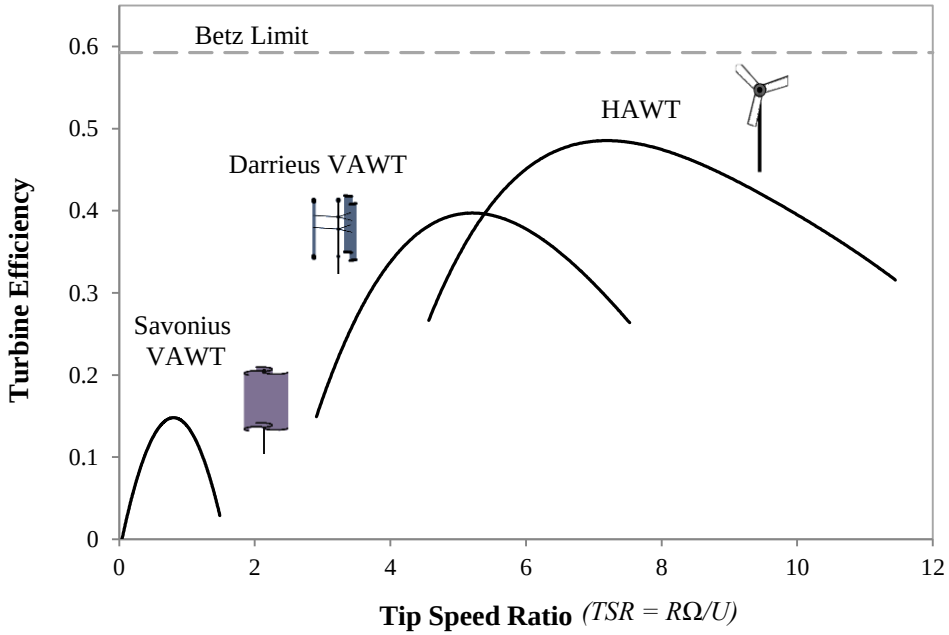

Figure 1.3: Power efficiencies of common wind turbine designs as a function of tip speed ratio, the non-dimensional rotational speed of the turbine (adapted from Hau 2006).

While Darrieus turbines are apparently less efficient that HAWTs, developing a Darrieus turbine to its full potential may close the efficiency gap. Furthermore, Dabiri et al (2008) recently showed that the power density of a VAWT farm has the potential to be an order of magnitude greater than an HAWT farm. This is because the wind through a VAWT recovers faster, allowing for the turbines to be packed closer together in counter-rotating pairs. This strongly supports the case for further VAWT development and application.

1.3 Mini-turbines in the Urban Environment

Urban environments contain high densities of wind energy that are inaccessible to large HAWTs. By exploring small-scale VAWTs, or "mini-turbines," wind energy can possibly be harvested more efficiently from these constrained spaces. While VAWTs have been studied previously, this project explores a comprehensive parameter space that has apparently not yet been rigorously studied. In doing so, this project is developing fundamental knowledge of the fluid dynamics of mini-turbines. The ultimate result of this project is a robust and radically new wind turbine that will blend engineering and art in the urban environment, such as the renderings shown in Figure 1.4.

Recently, there has been a large research initiative within the Mechanical and Aerospace Engineering Department at Cornell University to research vibrational wind harvesting devices. Research groups have utilized fluttering, galloping, and bluff body vibration to produce electricity via piezoelectric materials. Power output is typically in the microwatts or milliwatts range, which is suitable for powering microsensors. Figure 1.5 shows the efficiencies of small wind harvesting devices while Table 1.1 shows estimates of energy density in "surface flow" and "through flow" arrays, as defined in Figure 1.4.

Mini-turbines will be able to fulfill the vibrational energy niche by providing power for microdevices or possibly larger loads such as lighting on and around buildings as well as streetlights. Small rotational devices will be able to provide more energy per area as compared to vibrational devices.

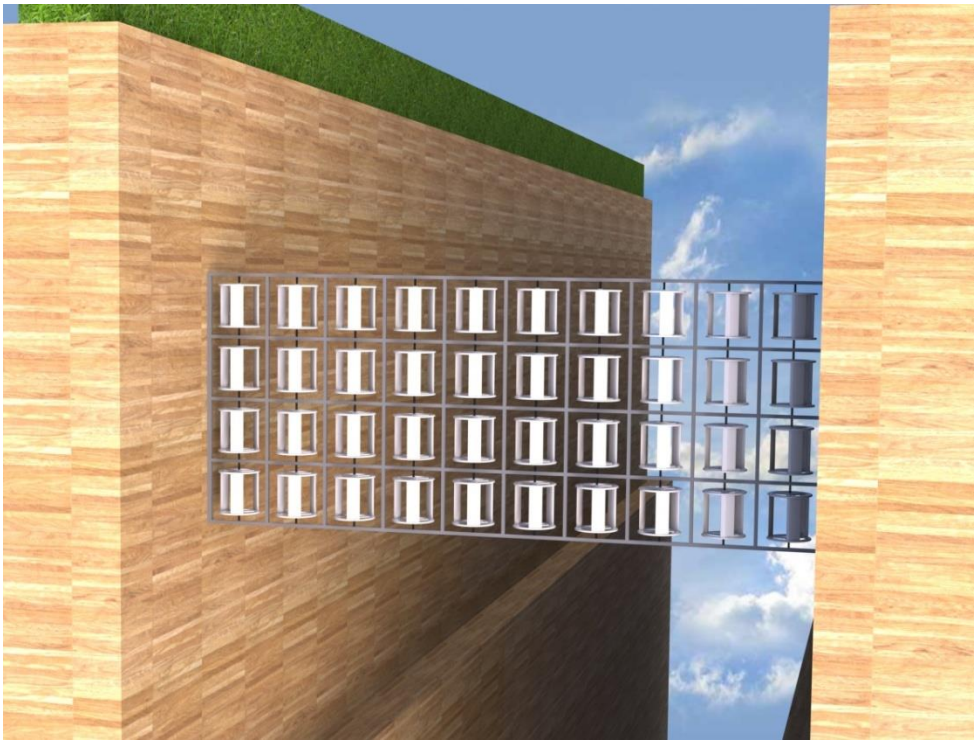

(a) Through- Flow Array

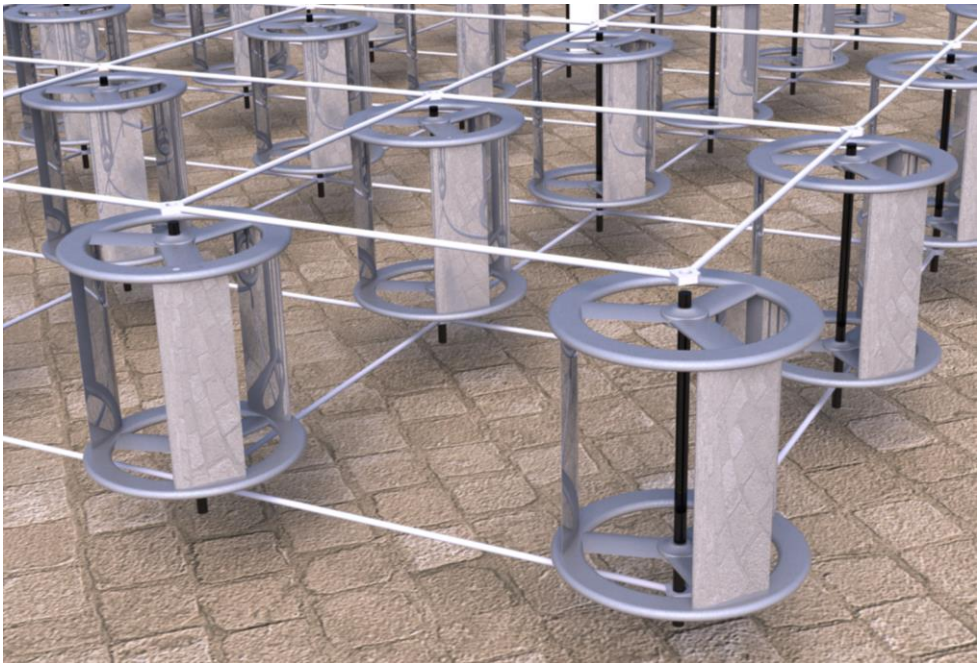

(b) Surface-Flow Array

Figure 1.4. (a) Mini-turbines can be placed in urban environments as a Through-flow array between buildings or as **(b)** Surface-flow arrays on vertical or horizontal surfaces.

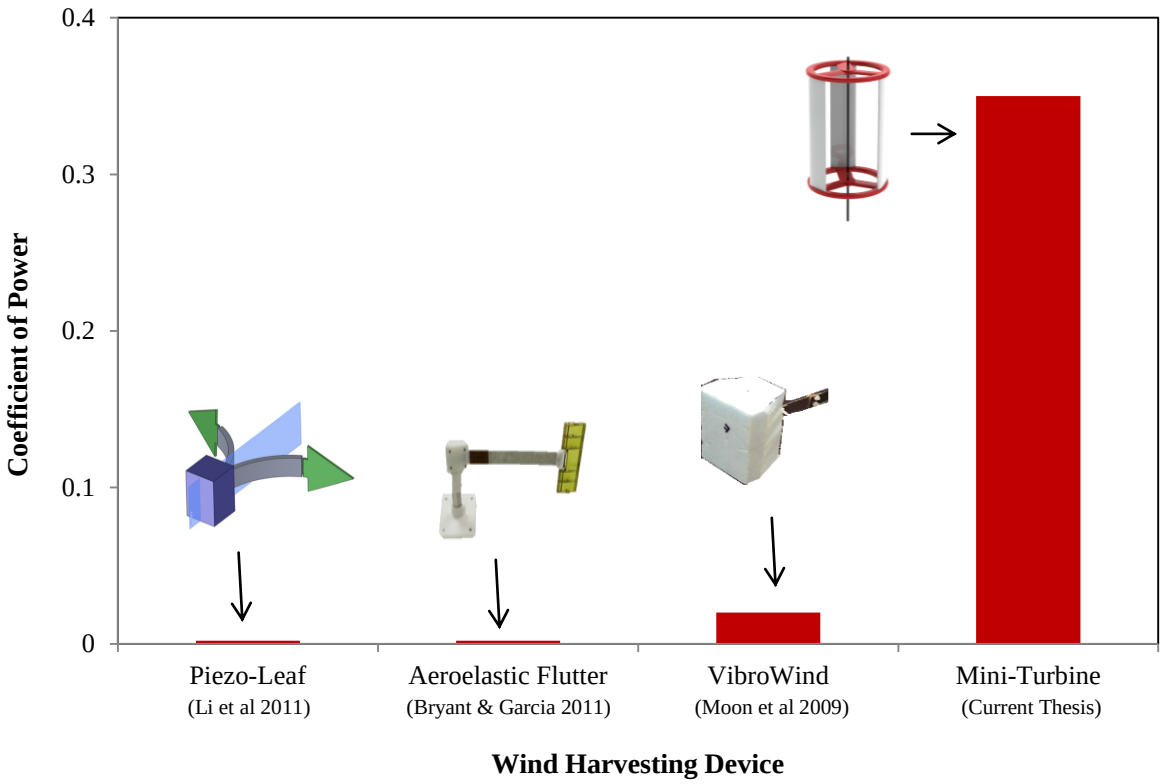

Figure 1.5. Energy efficiencies of small wind harvesting devices. Mini-turbines have large potential for urban applications.

Table 1.1 Energy density of small energy harvesting devices

Device	Reference	Single Device		Surface-Flow Array			Through-Flow Array		
		Cp	*Unit Cost ($)*	*No. of Devices*	*Power per Area (W/m^2)*	*Cp of Array*	*No. of Devices*	*Power per Area (W/m^2)*	*Cp of Array*
Piezo-Leaf	Li et al (2011)	0.002	$5.00	60	0.02	0.0001	100	0.03	0.00008
Aeroelastic Flutter	Bryant & Garcia (2011)	0.002	unknown	6	0.02	0.00005	20	0.1	0.0002
VibroWind	Moon et al (2009)	0.020	unknown	7	0.1	0.001	63	0.5	0.01
Mini-Turbine	Current Thesis	0.35	$4.00	9	18	0.066	16	32	0.12

Vertical-axis wind turbines can be divided into two categories: lift-based and drag-based. Lift-based VAWTs are "Darrieus" turbines while drag-based devices are "Savonius" turines. Figures 1.6a and b are examples of Darrieus turbines, which utilize lift forces from airfoil-shaped blades to produce torque. Windspire is considered a straight-bladed Darrieus wind turbine, also known as an H-Rotor. QuietRevolution is also a Darrieus-type wind turbine, but it has curved helical blades. The HelixWind (Figure 1.5c) is an example of a Savonius wind turbine which utilizes differences in drag forces to produce torque (See Figure 1.7). The classical Savonius turbine has straight cups much like an anemometer, but HelixWind has a twist to its design. The Windscreen designed by MIT architect Dr. Yoon contains artistic renderings of VAWTs and only extract enough energy to illuminate small LEDs, but provide an example of the aesthetic potential of small scale VAWTs.

(a) Windspire[1] (b) QuietRevolution[2] (c) HelixWind[3] (d) MIT Windscreen[4]

Figure 1.6. Commercial VAWTs being studied by (a) Dabiri of Caltech and (b) Babinsky of Cambridge. Other products include (c) Helix Wind and (d) MIT architect Yoon's Windscreen.

Darrieus turbines are more efficient than Savonius turbines and their rotational speeds can exceed the wind speed due to the lift-based operating principle. The mini-turbines of this project are classified as straight-bladed Darrieus wind turbines, but may exhibit different characteristics than is typically seen in large scale commercial wind turbines such as Windspire.

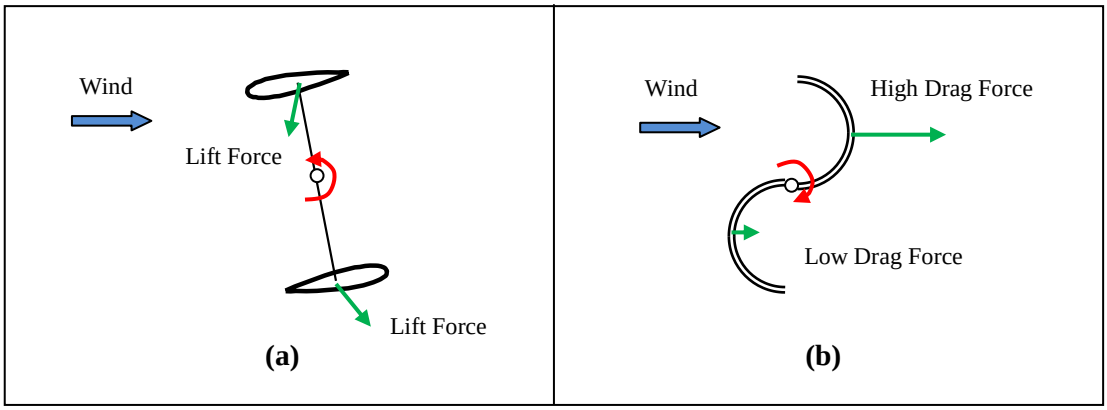

Figure 1.7. (a) Lift-based and (b) Drag-based VAWT working principles

The tip speed ratio (TSR) of a turbine is defined by Equation 1.5 below, where R is the radius of the turbine, $\dot{\theta}$ is the rotational velocity, and U is the freestream velocity. Hence, it is the ratio of the rotational velocity of the turbine and the freestream velocity.

$$TSR = \frac{R\dot{\theta}}{U} \tag{1.5}$$

Turbines that operate at low TSRs (TSR < 2) have blades that experience large ranges of angles of attack, on the order of $\pm$ 90 degrees. On the other hand, a turbine at high TSR (TSR > 2) experiences lower angles of attack on the blade ($\pm$ 20 degrees) which corresponds to a high lift to drag ratio and possibly more power. However, high TSR operation may also lead to higher fatigue of the blades. The effects of TSR and the physics of the turbine are discussed further in Sections 3 and 8.

1.4 Eggbeater Darrieus turbines

Modern development of VAWTs in the US began in the 1970s at Sandia National Laboratories with large scale "eggbeater" type Darrieus turbines, as seen in Figure 1.8a. The basis for the curved eggbeater blades was to emulate the ideal "troposkein" shape, which can be pictured as the curve a skipping-rope makes when secured at both ends. This ideal shape was thought to minimize bending stresses due to the centripetal forces of the rotating blades, but is difficult to manufacture (Paraschivoiu 2002). The field study done by Sheldahl, Klimas, and Feltz (1980) resulted in a maximum coefficient of power $C_P = 0.39$ at a tip speed ratio TSR = 5.2 for a three-bladed, 5m diameter rotor.

The eggbeater Darrieus turbine was commercialized by FloWind in the 1980s, creating wind farms in California which lasted a decade and delivered electricity to 20,000 homes until mechanical fatigue, failure, and unreliability made the farms uneconomical (Gipe 2013). Figure 1.8b below depicts the largest VAWT farm made to date.

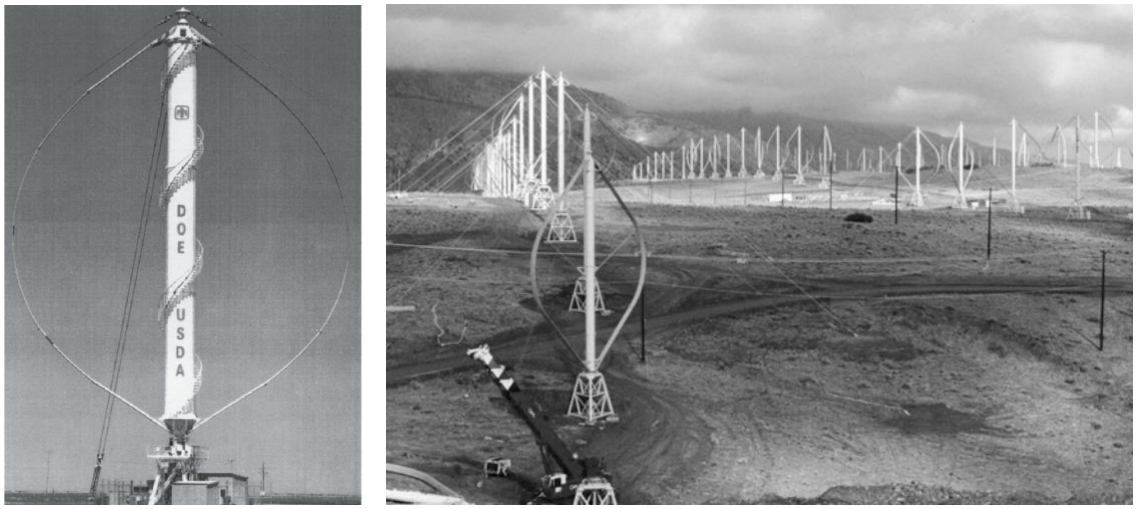

(a) **(b)**

Figure 1.8: (a) Classical "eggbeater" Darrieus turbine at DOE/Sandia National Laboratories (Paraschivoiu 2002) **(b)** Flowind's 1980s farm of Darrieus turbines in Southern California (Hau 2006)

1.5 Straight-bladed Darrieus turbines

The resurgence of Darrieus VAWT research in the last ten years has favored straight-bladed turbines rather than the eggbeater turbine. Some advantages of the straight-bladed turbine over the eggbeater turbine are the ease of manufacturing, assembly, and installation.

Fiedler & Tullis (2009) experimented with the commercial turbine Cleanfield V3.5, rated at 2.5kW with a 1.25m radius at the Fire Research Lab at Waterloo, Canada (See Figure 1.9). They had two mounting positions along the chordline to investigate the effect of mounting position and preset pitch angle for two symmetric airfoil profiles (NACA 0015 and 0021). Their results show a maximum $C_P = 0.34$ for both airfoils, though the NACA 0021 had a broader TSR range with good performance. The TSR of the peak C_P (TSR= 1.6 for NACA 0015, and TSR = 1.45 for NACA 0021) was independent of the effective offset pitch angle. As seen in Figure 1.9c, the power curves (C_P vs TSR) collapse really well above 8 m/s, suggesting an independence on Reynolds number.

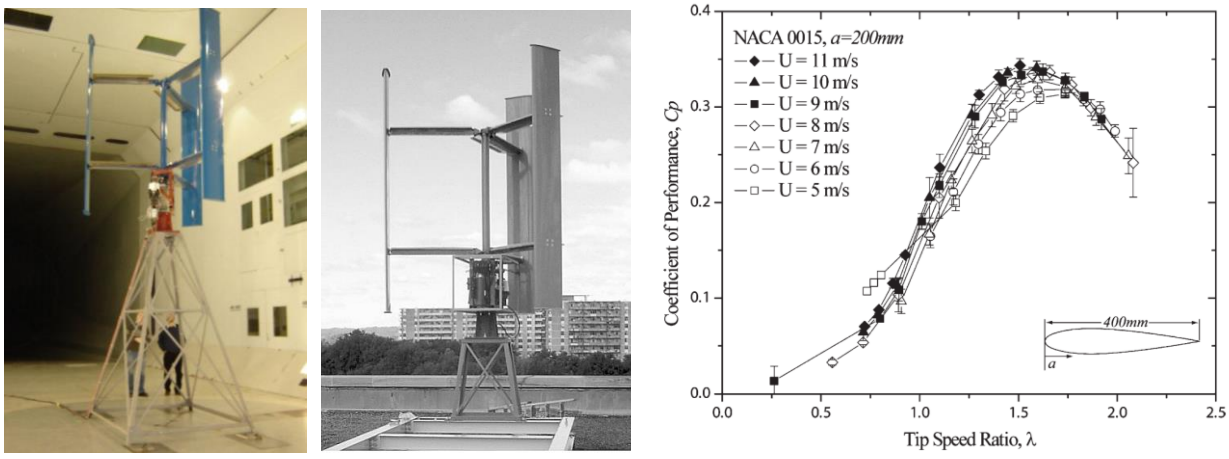

(a) **(b)** **(c)**

Figure 1.9: Cleanfield Energy Corp 3.5 kW VAWT **(a)** in wind tunnel and **(b)** on rooftop. **(c)** Power curves for a NACA 0015 blade with 0 pitch angle (Fiedler & Tullis 2009).

Fiedler & Tullis also found that pitching the blades inwards decreased C_P, while pitching the blades outwards increased C_P. They concluded that a preset pitch angle can be used to cancel out pitch created from an offset mounting position, allowing aerodynamic performance to be maintained if the blades need to be mounted offset for structural reasons.

The Tullis group (2007) also studied the CleanField turbine on the rooftop, using tufts to visualize flow reversal. Increasing TSR decreases the occurrence of flow reversal, as expected. Furthermore, pitching straight blades outwards delays flow separation and decreases flow reversal. However, they believe that the dynamic stall and vortex shedding that result from flow separation are important lift mechanisms (Armstrong, Fiedler, & Tullis 2012). Their rooftop studies also included turbulent wind performance tests. They found that turbine performance is independent of wind *direction* variations, but dependent on wind *velocity* fluctuations. This supports the true omni-directional nature of VAWTs. For low velocity fluctuations the turbine performs equal to wind tunnel tests, but for large velocity fluctuations, turbine performance decreased linearly (Kooiman & Tullis 2010).

The Tidal Energy Research Group at the University of Oxford studied transverse horizontal axis water turbines in Newcastle University's combined wind, water, and current tank flume facility as shown in Figure 1.10. The turbine geometry is: radius = 0.25m, chordlength = 65mm, length = 1.53 m, airfoil profile = NACA 0018 "wrapped" to the arc of a circle. The number of blades was varied from 3 to 6 to study the effect of solidity (the ratio of blade area to turbine area).

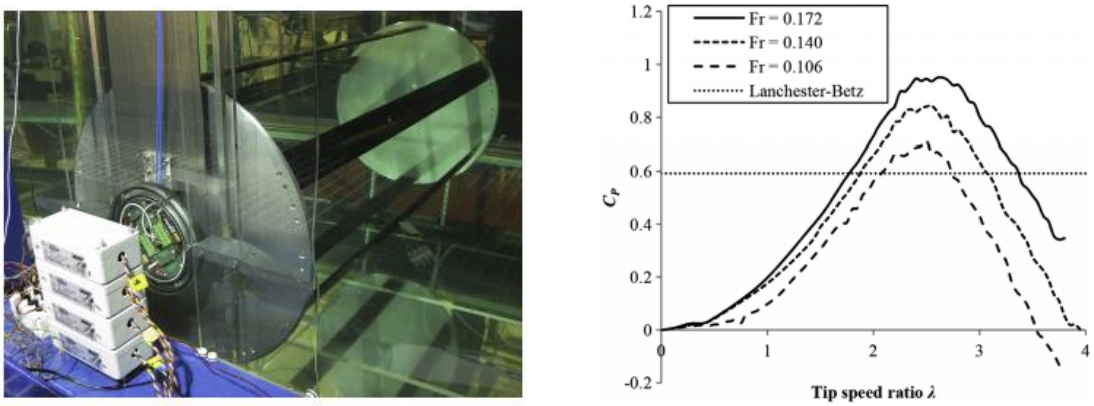

(a) **(b)**

Figure 1.10. Transverse horizontal axis water turbine studied by Oxford researchers (a) in the water flume facility (b) Results surpass the Betz limit by utilizing blockage effects (McAdam et al 2013a)

McAdam, Houlsby, and Oldfield (2013a) found that lower solidity increases C_P and TSR; when there are 3 blades, the flow velocity through the rotor increases to operate at a higher TSR to prevent the blades from stalling. They also "reversed" the flow by turning the turbine 180 degrees, and found no difference, confirming the omni-directionality of VAWTs in their experimental setup.

Most importantly, the Oxford researchers were able to "surpass" the theoretical Betz limit by utilizing blockage effects and increasing the Froude number, the ratio of the characteristic flow velocity to the surface wave velocity. As Equation 1.6 shows, higher Froude numbers occur for higher flow velocities *U* and/or lower water depths *y* (White 2008). For the Oxford group's experimental setup, higher Froude numbers corresponds to higher blockage effects. With the turbine stretched the entire width of the open water channel, the flow is unable to go around the turbine and is forced through the rotor. It may be possible that the flow is exerting an axial force on the walls of the channel, which is counter to the Betz limit theory that the rotor is in a

streamtube. The assumption that the turbine is in an open field flow is no longer valid, and the Betz limit theory should not be applied.

$$\mathrm{Fr} = \frac{flow\ velocity}{surface\ wave\ speed} = \frac{U}{\sqrt{gy}} \tag{1.6}$$

The Oxford group also did a structural analysis and found that the range of loading experienced by the turbine blades increases as TSR increases. Higher loading corresponds to lower lifetime (McAdam, Houlsby and Oldfield 2013b).

Yamada et al (2011) experimented with a two-bladed VAWT of 0.3m radius. The maximum C_P = 0.25 at TSR = 1.6. They tested different airfoil profiles (NACA 0020, 3520, 6520, 0018, 0025, 0030, 6518, 6525, and 6530) to investigate the effect of thickness and camber. Very large camber was detrimental to performance, while small camber made little difference. The effects of thickness on symmetric and asymmetric blades were inconclusive. Yamada et al also studied torque variation, showing that the highest torque occurs when the blade is in the upstream half of the turbine, as one would expect.

A technical report from the National Renewable Energy Laboratory contains field studies of the commercial Windspire turbine. The turbine produces 1kW with a maximum C_P = 0.19 (Huskey et al 2009). Another field study of a prototype VAWT in Sweden produced a maximum C_P = 0.29 at TSR = 3.3 over a span of three months (Kjellin et al 2011). These two studies show the C_P of large scale Darrieus turbines in the field are of the same magnitude as of full-scale wind tunnel studies.

1.6 Helical and Truss Darrieus turbines

Helical VAWTs have been popular in the marine energy (hydrokinetic) industry and have recently gained popularity in the wind turbine field as well. The first helical turbine was patented by Alexander Gorlov (See Figure 1.11). Gorlov (1998) found that helical turbines can operate at low pressure gradients, self-start, and eliminate torque fluctuations. Furthermore, his studies showed that helical turbines have a higher C_P than straight-bladed turbines of the same size.

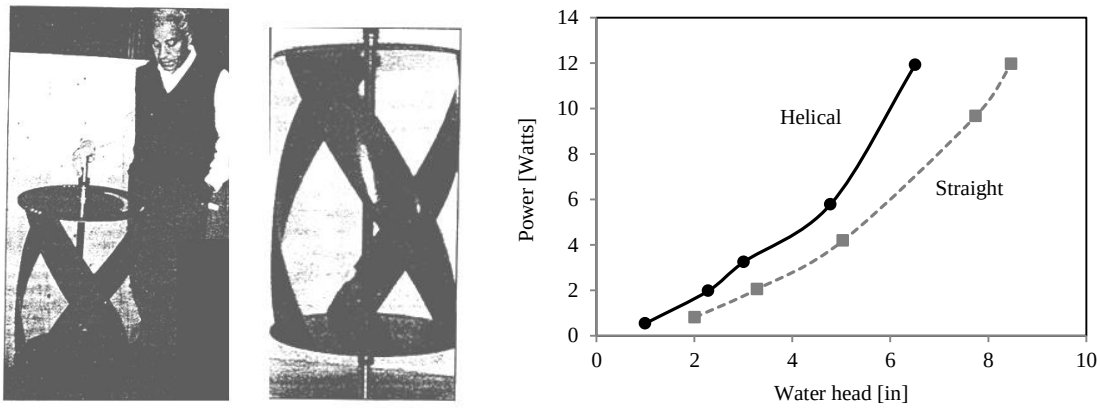

Figure 1.11: (a) Gorlov (1998) with his invention, the helical hydraulic turbine (b) Helical turbines produce more power than straight-bladed turbines (adapted from Gorlov 1998)

Whether straight-bladed turbines can self-start or not is a point of debate among various research groups which have contradictory results (for example Islam et al 2007 and Hill et al 2009). However, Kirke & Lazauskas (2011) explain that helical blades are able to self-start because the blades experience a smaller range of stall. Additionally, the minimum helical twist angle of the blades is 40^o; lower angles have negative energy per cycle and will not be able to self-start while higher angles have positive energy per cycle and will self-start more readily.

They note that higher solidity increases starting torque and hence improves self-starting capabilities, but at the cost of power output. Furthermore, the vibration of straight-bladed turbines is reduced in helical turbines because (1) blades do not stall along their full span simultaneously, (2) blades stall more gradually, and (3) blades experience a lower range of angle of attack (Kirke & Lazauskas 2011). Less vibration and fatigue would result is a higher lifetime product.

Yang and Shu (2012) optimized a hydrofoil for helical water turbines (See Figure 1.12). Their two-bladed turbine (radius = 150 mm, chordlength = 90 mm, height 450 = mm, sweep angle = 44 deg) with the custom hydrofoil shape performed better than the turbine with NACA 0012 or Gottingen 623 profiles, reaching $C_P = 0.41$. They conclude that the camber of the custom profile allows the blade to recover quicker from flow separation, stabilizing the flow for enhanced performance.

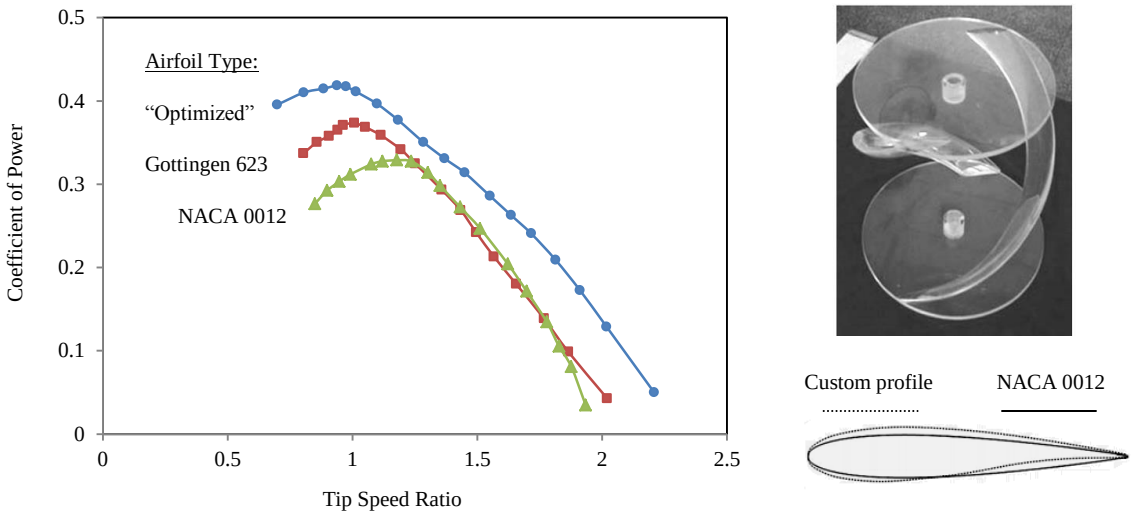

Figure 1.12. Two-bladed helical turbine with a custom hydrofoil shape has a greater coefficient of power than standard airfoil shapes (Yang & Shu 2012).

The previously discussed Oxford researchers have also developed a twisted water turbine, shown in Figure 1.13. The "truss" turbine has a twist angle of 46 degrees and the same average radius, blade airfoil, and solidity as their own straight-bladed turbine previously described. The blade length is 0.5 m, there are six blades per "bay," and three "bays" supported by triangular struts with a NACA 0012 profile. Their patent pending truss design uses the blades as structural members, allowing a portion of the hydrodynamic load to be transferred via axial forces. Thus, structural longevity is expected (McAdam et al 2013c).

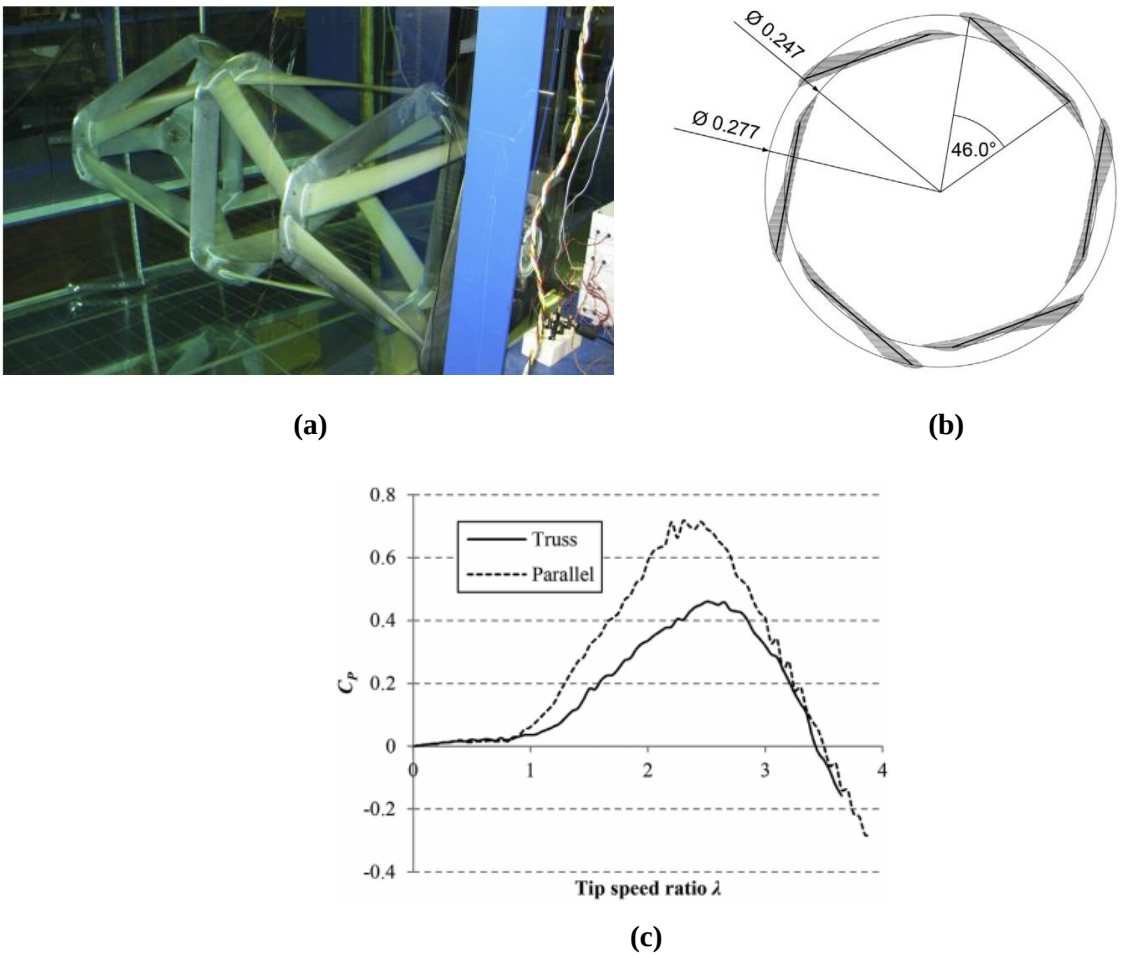

(a) **(b)**

(c)

Figure 1.13. (a) "Truss" turbine in the water facility **(b)** Top view of truss turbine geometry **(c)** Truss turbines have reduced C_P compared to a parallel straight-bladed turbine (McAdam et al 2013c).

Unlike Gorlov (1998), the Oxford truss turbine has a lower C_P than their own straight-bladed turbine discussed previously. This is not surprising since the truss turbine has additional triangular supports that add drag and disturb the flow. In an earlier study, the Oxford researchers tested a truss blade with no triangular frame and a lower sweep angle of 12 degrees which resulted in only a slight C_P reduction compared to their straight-bladed turbine. (McAdam et al 2013c).

The previously discussed Tullis group has been working on canted blades as shown in Figure 2.14 with and without "fences," or endcaps (Armstrong, Fiedler, & Tullis 2012). The canted blades have a similar peak C_P when compared to their own straight-bladed turbine, though at a higher TSR. The fences act to impede spanwise flow, reducing flow separation (as seen in tuft visualization), but slightly shifting the C_P curve towards a lower TSR (Armstrong, Fiedler, & Tullis 2012).

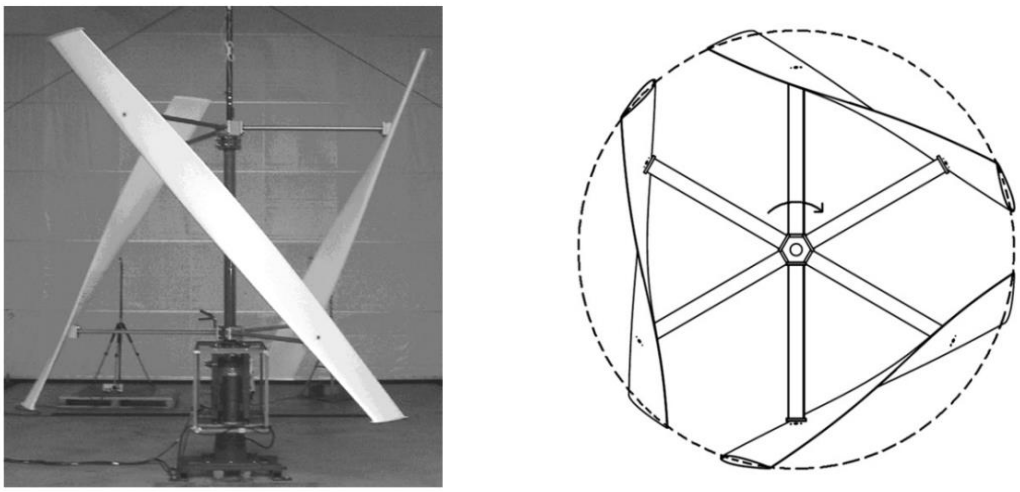

Figure 1.14. Canted blades perform comparably to straight blades (Armstrong, Fiedler, & Tullis 2012).

Computational work concerning helical turbines include McIntosh and Babinsky (2013) and Scheurich, Fletcher, and Brown (2010). McIntosh and Babinsky modified a free vortex model and validated it with ink-dye experiments and wind tunnel data from the QuietRevolution turbine company (See Figure 1.15). Scheurich, Fletcher, and Brown used a vorticity transport model to simulate the wake dynamics of straight, eggbeater, and helical VAWTs. They concluded that straight and eggbeater turbines had a shortened design life due to the load variations, while helical blades had less load fluctuations and an asymmetric wake vorticity.

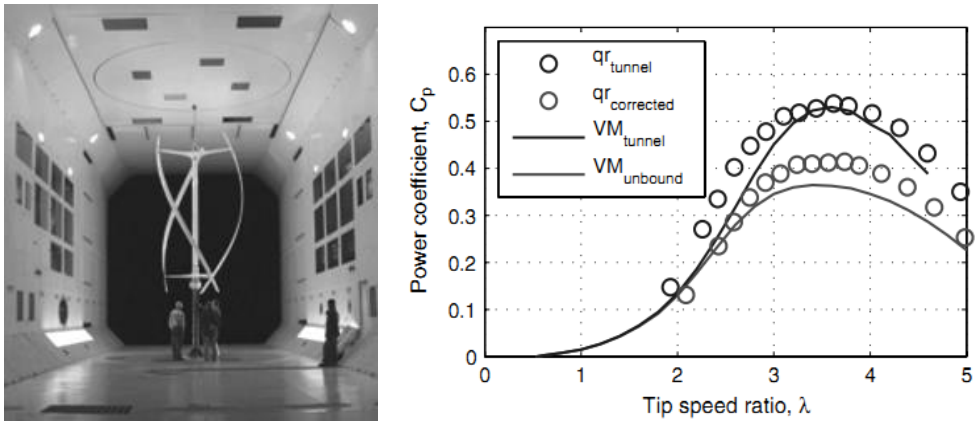

Figure 1.15. QuietRevolution turbine in a wind tunnel results in a C_P of ~0.4 when corrected for blockage (McIntosh & Babinsky 2013)

Other research concerning VAWTs includes numerical models and computational studies that explore solidity, variable pitch, dynamic stall, flow curvature, and wake formation. The simplest numerical model is the single streamtube model developed by Templin in 1974 (Paraschivoiu 2002). This model assumes the turbine is a single actuator disc and utilizes blade element momentum theory to calculate the power performance. Paraschivoiu has done extensive research to build and improve the single streamtube model into the double multiple streamtube model to better represent VAWT aerodynamics.

2. Experimental Methods

2.1 Wind Tunnel Setup

All experimentation is conducted in the burgundy blower-style wind tunnel at Mechanical and Aerospace Engineering at Cornell University shown in Figure 2.1 below. The wind tunnel is composed of a number of critical aerodynamic features: the blower fan, diffuser, settling chamber, contraction, and test section.

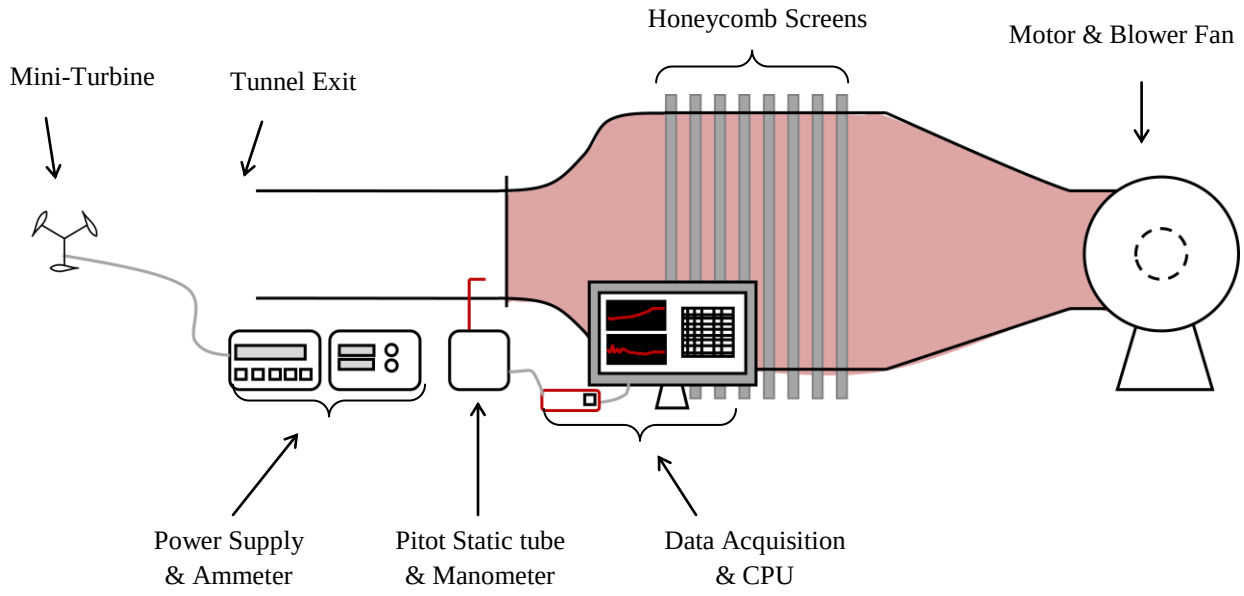

Figure 2.1. Blower-type wind tunnel with labeled sections and instrumentation.

The blower fan on the wind tunnel draws in and accelerates ambient air into the wind tunnel. This accelerated flow, which is turbulent after passing through the fan, enters the diffuser section of the wind tunnel. The diffuser section, utilizing the principles of conservation of mass, decreases the flow velocity. Immediately following the diffuser, the flow enters the settling

chamber, where a series of honeycomb screens with decreasing cell diameters (as wind travels downstream) smooth the flow to a near uniform velocity profile. Next, the flow enters a contraction which increases the flow velocity. The flow enters the test section with a nearly uniform velocity profile. The experimental turbine assembly is positioned in the jet of the wind tunnel. This location allows for quick and easy adjustments to the turbine assembly while maintaining integrity of the wind velocity.

The wind tunnel flow velocity is monitored through a LabVIEW user interface. A pitot-static tube located in the test section of the wind tunnel, upstream of the turbine, connects to a manometer which outputs a voltage proportional to the pressure difference in the flow. The pressure difference is converted to windspeed by Bernoulli's equation and displayed on the computer. The data acquisition software also displays the ambient temperature and density.

2.2 Mini-Turbine Assembly

The turbine assembly and exploded diagram, shown in Figure 2.2, consist of a horizontally mounted solid shaft on low friction bearings on side supports. 3-D printed turbine blades are mounted on each end onto aluminum endplates. The endplates have C-N-C machined mounting holes at angles from 0-10 degrees in one degree increments. Turbine blades have 1/8" diameter steel rods running the spanwise length of the blades. The blades are positioned in the mounting holes at a chosen angle, and hex nuts are tightened on the ends of the rods to secure the blades. The endplates are secured to the solid shaft with a collar.

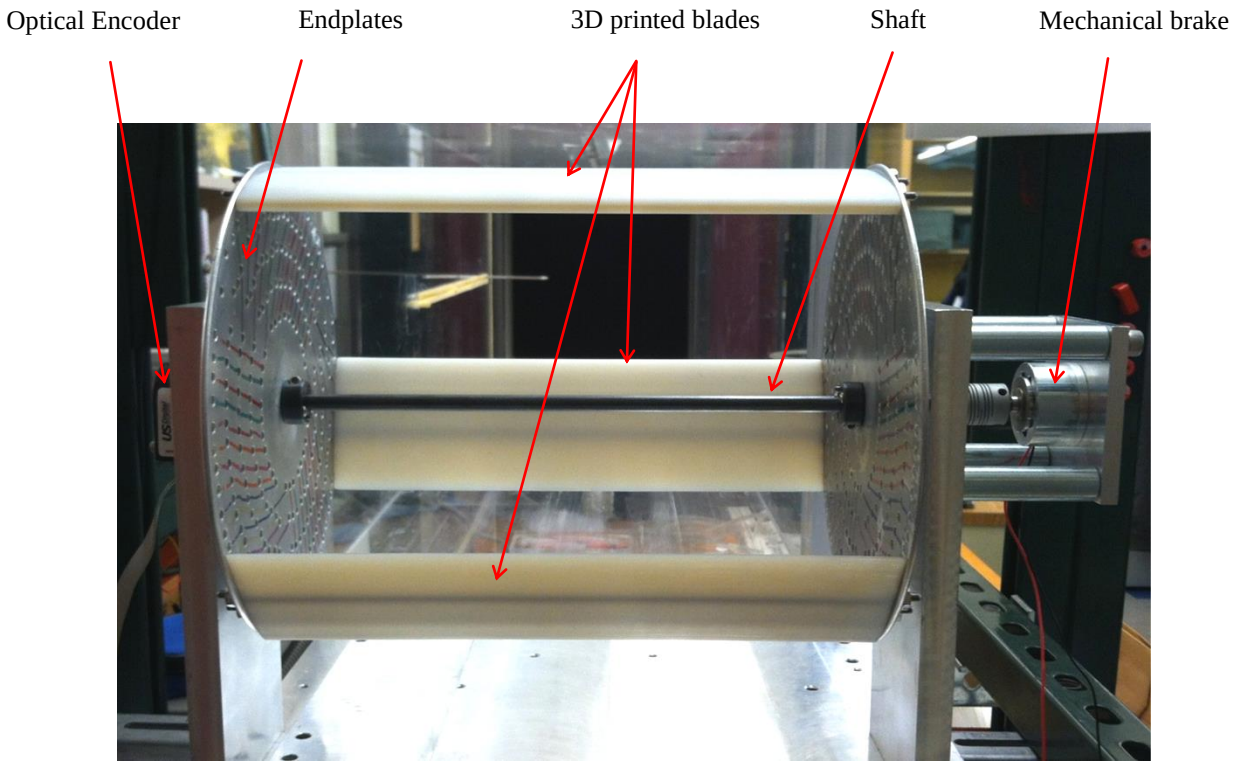

(a)

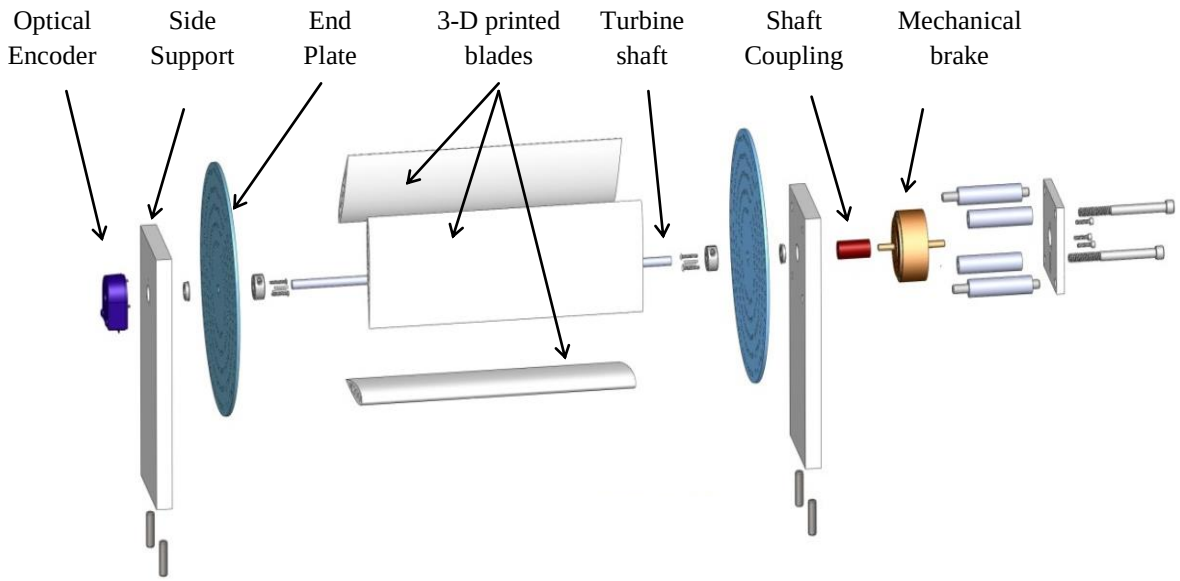

(b)

Figure 2.2 (a). Mini-turbine assembly in the jet of the wind tunnel **(b)** Exploded diagram of assembly

The angular velocity of the turbine is recorded and displayed in LabVIEW through a 1024-slit optical encoder attached to one end of the turbine shaft. At the other end of the shaft, a mechanical brake is mounted to the side support and connected to the shaft with a standard coupler. Two mechanical brakes are used for experimental testing. The HB 2-5-2 can apply a maximum torque of 23 mNm, while the HB 16-2 can apply 177 mNm. The HB 2-5-2 allows for more accurate application of smaller torques, while the larger brake is only used when the turbine torque exceeds the smaller brake's maximum applicable torque.

Torque is applied through a constant current supply. Current is only applied when the turbine is rotating, to limit effects of cogging torque. Likewise, the turbine must be rotating when offloading current to limit this effect. The current supply is connected to a multi-meter in series, which displays a more accurate current measurement than the current supply's display.

2.3 Mini-Turbine blades

Blades for the mini-turbine were designed using the computer-aided design program SolidWorks. Figure 2.3 below defines the convention used for the offset pitch angle of the blade, the angle between the chordline and the turbine circumference relative to the midchord point. The blades have multiple sets of mounting holes to maximize the range of pitch angles in conjunction with the C-N-C machined mounting holes on the end plate. Thus, the total pitch angle β of a blade is a function of different design parameters as follows:

$$\beta = \theta_0 + \theta_P + \theta_x \tag{2.1}$$

where θ_0 is the preset angle of the blade relative to the chordline, θ_P is the angle of the mounting holes on the endplate, and θ_x is the offset angle created when the mounting holes are an x distance from the midchord point. Given the radius R, equation 2.1 becomes:

$$\beta = \theta_0 + \theta_P + \text{atan}\left(\frac{x}{R}\right) \tag{2.2}$$

The diagrams in Figure 2.4 on the next page how each angle contributes to the total offset pitch angle.

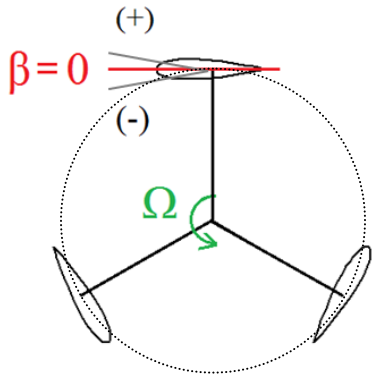

Figure 2.3. The total offset pitch angle β of a blade is defined as the angle between the chordline and the turbine circumference relative to the midchord point

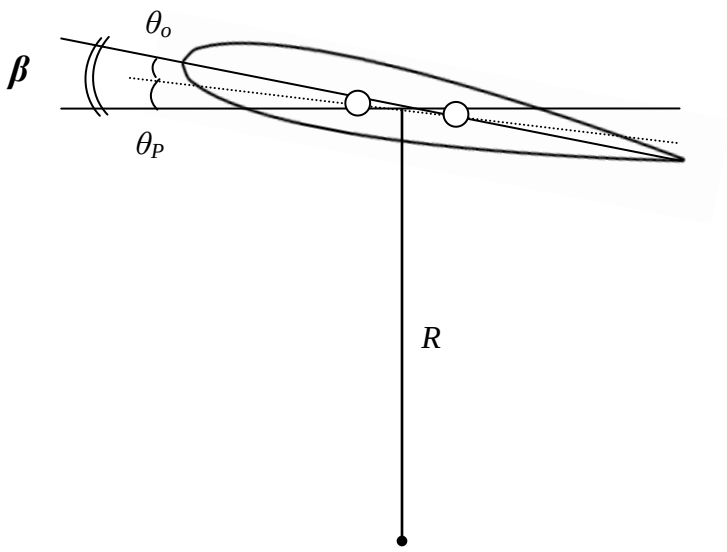

(a) Contribution of preset and mounting angles to total pitch

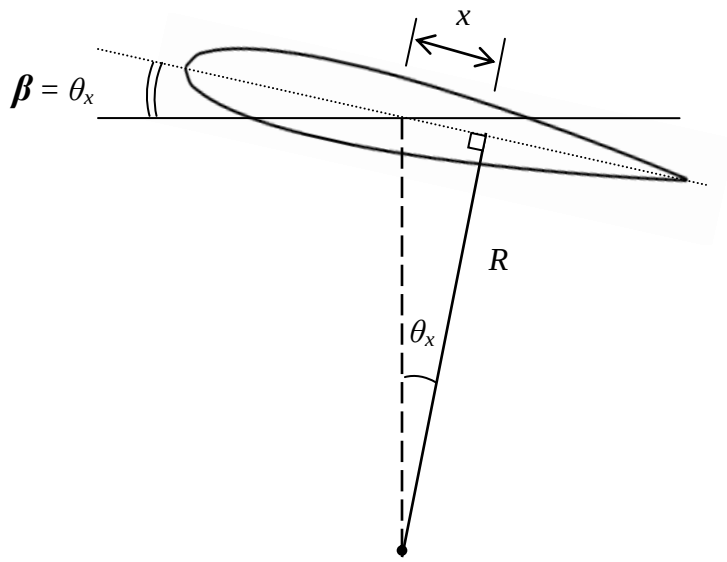

(b) Contribution of offset angle to total pitch

Figure 2.4: Total offset pitch angle β is a function of θ_0, θ_P, and θ_x. **(a)** Illustration of preset and mounting angles when the blade is mounted at the midchord point. **(b)** Illustration of offset angle created when the blade is mounted x distance from midchord point.

Equations 2.1-2.2 were used to choose the optimal location of the mounting holes along the chordline, as well as their preset angle, while taking into account limited thickness of the blade. Such design considerations allowed us to achieve angle of attack ranges of -26 to +15 degrees for the 6 cm chordlength blade and -32 to +15 degrees for the 8 cm chordlength blade.

Figure 2.5 shows an example of a turbine blade with two pairs of mounting holes and three extra holes drilled out to reduce material cost and blade mass. Table 2.1 shows detailed measurements for the holes and distances. The blades are mounted at the desired pitch angles by utilizing a mounting guide and verifying the angle with a custom-designed 3-D printed pitch tool, shown in Figure 2.6. Blades longer than 3cm in chordlength utilize two rods, whereas smaller turbine blade sizes, such as the "Micro blades," can only support one rod. In such cases, the blade is positioned at its desired angle through the use of the turbine blade pitch tool, and the hex nuts are tightened until the turbine blade remains in a fixed position from frictional forces.

The resultant turbine blade geometries are shown in Tables 2.2 – 2.4. Almost all of the blades have an airfoil cross-section from the NACA 4-digit series. The "c/D ratio" is the ratio of the chordlength of the blade to the diameter of the turbine. The "Large Camber" airfoil was custom designed to have the same thickness profile as a NACA 0015, but cambered to a line which arched with the circumference of the blade path, as shown in Figure 2.7. Hence, it was nicknamed "NACA arc-15".

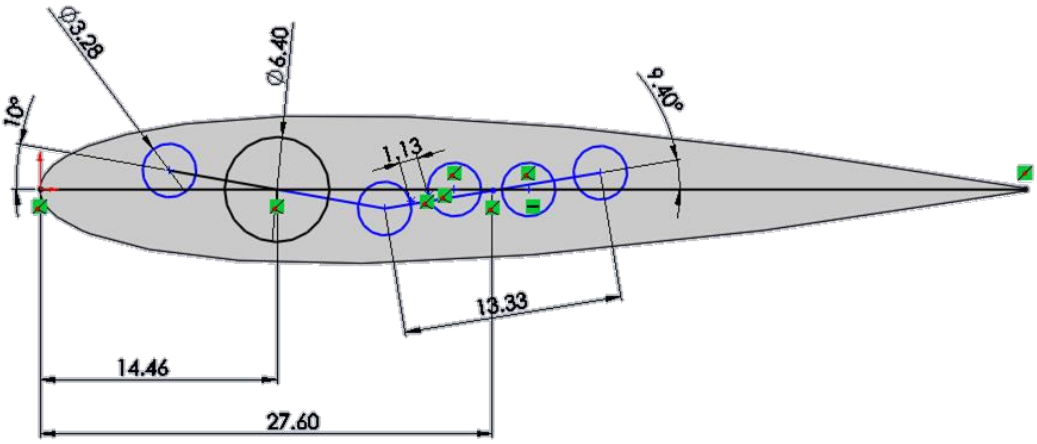

Figure 2.5. Diagram of a turbine blade sketch in SolidWorks

Table 2.1 Dimensions for mounting holes and distances

Feature	**Metric Units**
⅛” rod holes	3.28 mm
¼” holes	6.40 mm
Distance between mounting holes	13.33 mm
Smallest distance from holes to other holes or edges	1-1.5 mm
Distance from leading edge to center of mounting holes	Varies
Angle of mounting holes	Varies

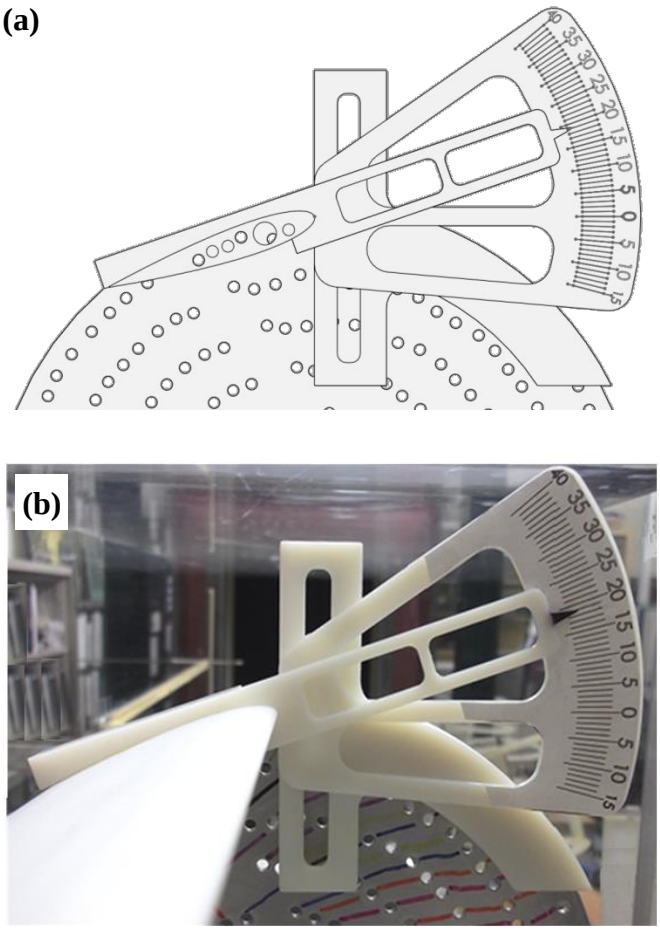

Figure 2.6: (a) Blade pitch measuring tool graphic from SolidWorks and (b) 3-D printed result

Table 2.2 Specifications of different blades tested for c/D experiments

Nickname used in this report	*Image*	*Airfoil Type*	*Chordlength*	*c/D*
Big blades		NACA 0015	8 cm	0.48
Medium blades		NACA 0015	6 cm	0.36
Small blades		NACA 0018	4 cm	0.24
Micro blades		NACA 0021	2 cm	0.12

Table 2.3 Specifications of different blades tested for camber experiments

Nickname used in this report	*Image*	*Airfoil Type*	*Chordlength*
Medium blades (Symmetric)		NACA 0015	6 cm
Small camber		NACA 4415	6 cm
Medium camber		NACA 6415	6 cm
Large camber		NACA arc-15	6 cm

Table 2.4 Specifications of different blades tested for thickness experiments

Nickname used in this report	*Image*	*Airfoil Type*	*Chordlength*
Thin blades		NACA 0009	6 cm
Medium blades (Baseline)		NACA 0015	6 cm
Fat blades		NACA 0021	6 cm

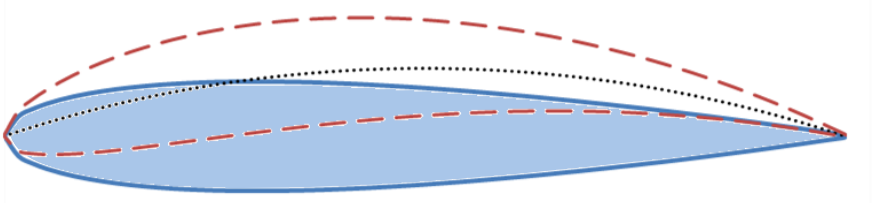

Figure 2.7. Custom designed airfoil denoted "NACA arc-15" has a camber line arched with the circumference of the blade path and the same thickness profile as a NACA 0015.

Sweepback angles were also incorporated into turbine blade designs in the form of helical and "zigzag" blades. Helical blades are of a similar design to the previously mentioned QuietRevolution. The blade profile twists along a helical path that follows the circumference of the blade path such that the profile is also parallel to the freestream wind velocity for all cross-sections. The zigzag blades, pictured in Figure 2.9, also follow a helical path along the circumference of the blade path until the midspan, but then reverse direction. The zigzag blade comes to a point at the midspan, though future designs could include more wavelengths.

Equation 2.3 and Figure 2.8 show how sweepback angle χ and twist angle φ are related, while Table 2.5 shows the geometries of different blades tested. The sweepback angle is denoted as χ, the twist angle is φ, the radius of the turbine is R, and the length of the turbine is L. The photos in Figure 2.8 show a mini-turbine with helical blades with 30 degree sweepback and zigzag blades with a 45 degree sweepback angle.

$$\tan \chi = \frac{\phi R}{L} \tag{2.3}$$

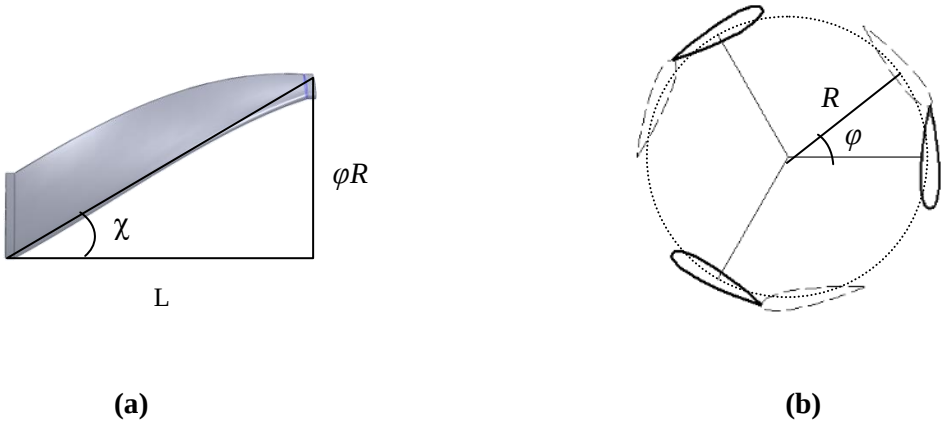

Figure 2.8. (a) Front view and (b) Side view of the geometry of helical and sweptback blades.

Table 2.5. Geometry used for helical and zigzag blades

Nickname used in this report	*Image*	*Airfoil Type*	*Chordlength*	*Sweepback Angle (degrees)*
Medium blades (Straight Symmetric) (Baseline)		NACA 0015	6 cm	0
Helical blades		NACA 0015	6 cm	30
30 degree Zigzag Symmetric		NACA 0015	6 cm	30
30 degree Zigzag Camber		NACA arc-15	6 cm	30
45 degree Zigzag Camber		NACA arc-15	6 cm	45

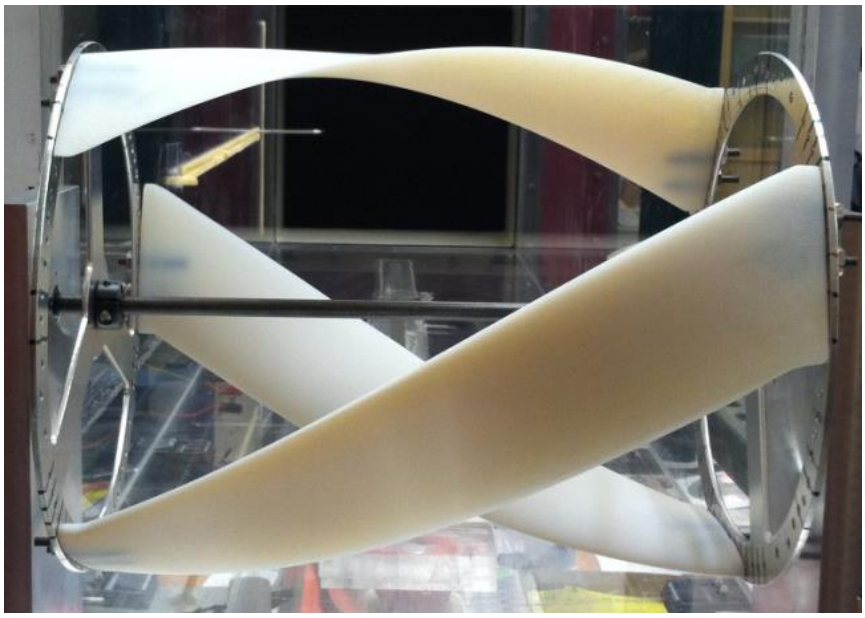

(a)

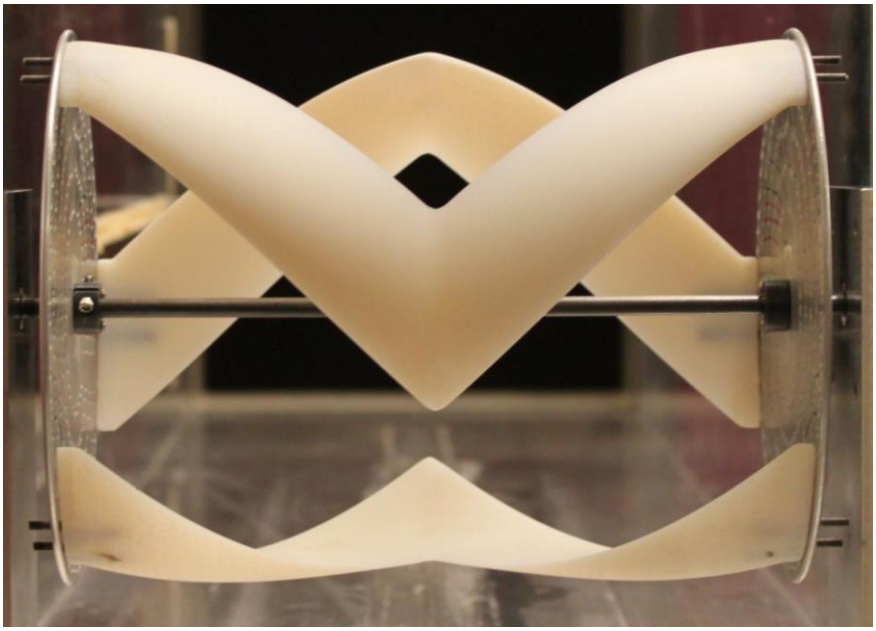

(b)

Figure 2.9. **(a)** Mini-turbine with helical blades with a sweepback angle of 30 degrees and **(b)** Mini-turbine with zigzag camber blades with a sweepback angle of 45 degrees.

Other turbine blade designs incorporated ideas from high lift devices, such as delta wings, slots, and tubercles from whale flippers. Figure 2.10 on the next page shows the geometry of each of these blades.

Delta wings achieve high lift at large angles of attack due to the formation of strong leading-edge vortices on the upper surface of the wing. These vortices are formed due to the pressure differential between the upper and lower surfaces and increase in circulation as they travel downstream from the apex point. As the angle of attack of the delta wing is increased, the pressure differential also increases with a resultant increase in vortex strength and lift. The vortex pair remains stable up to a certain angle of attack, typically greater than 30 degrees.

Another high lift device is slotted airfoils. The effect of the slot is to delay stall and to increase the maximum lift coefficient of the airfoil. Placing the slot nearest to the leading-edge has the greatest effect, and the effect diminishes as the slot is moved towards the trailing-edge. Thus, the blades for this test were designed with the slot near the leading-edge. The NACA 0015 airfoil used in the medium blades was chosen as the cross-section of the slotted blades to provide a suitable means of comparison with the baseline case.

The tubercles on whale flippers give humpback whales the ability to change direction quickly and effectively in their hunting maneuvers. The whale-inspired turbine blade has sinusoidal leading-edge protuberances to emulate the tubercles on whale flippers. The protuberances make stall more gradual, but the peak lift coefficient is decreased. However, the lift after stall is greater than that of a straight symmetric blade.

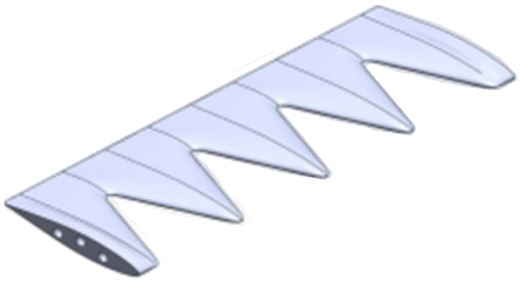

(a) Delta Wing blade

- Chordlength: 2 – 8 cm
- Airfoil: NACA 64A010
- Nose angle: 50 deg

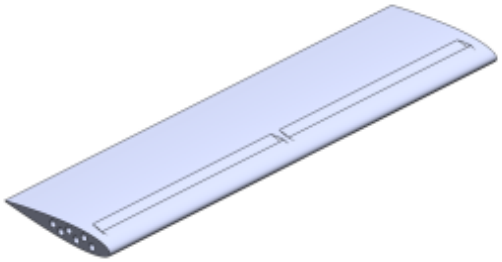

(b) Slotted blade

- Chordlength: 6 cm
- Airfoil: NACA 0015
- Slot: one near leading edge
- Slats: one in center

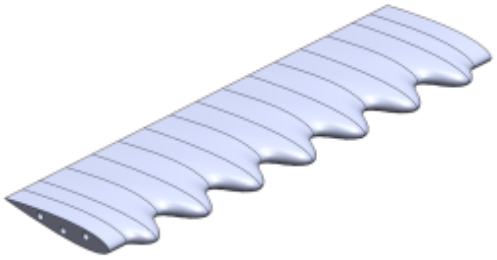

(c) Whale Flipper blade

- Chordlength: 6cm
- Airfoil: NACA 0015
- Wavelength: 50% chord
- Amplitude: 12% chord.

Figure 2.10: Unconventional custom-designed turbine blades inspired by high lift devices and whales

2.5 Conducting an experiment

This section outlines how typical pitch, coefficient of power, and self-start studies are conducted for a given turbine blade design. A pitch study evaluates the maximum angular velocity the mini-turbine can reach unloaded (without a mechanical brake) given a blade pitch and windspeed. From this data, the optimal pitch angle for a given set of blades can be determined.

Pitch studies are conducted by first fixing the blade pitch and then running consecutive tests at varying windspeeds, typically 3 - 8 m/s. The flowchart in Figure 2.11 illustrates the steps for each pitch angle. A pitch study consists of two phases: increasing windspeed and decreasing windspeed. The angular velocity of the turbine is recorded at each steady state for increasing windspeeds up to 8 m/s. If the angular velocity has not reached a faster operating mode, typically greater than 1000 RPM at 8 m/s, then a forced start is attempted. A Dremel drill is used to increase the turbine's angular velocity to greater than 1000 RPM. The turbine either reaches a steady state with a higher angular velocity than previously observed, or it returns to the previous steady state. The angular velocity after the forced start is recorded at the same windspeed. From this point, the windspeed is reduced by 1 m/s and the steady state angular velocity is recorded. This process is repeated until reaching the minimum windspeed. Note that a forced start is not required at each decreasing windspeed because the turbine's previous angular velocity serves as a forced start. The pitch angle is then incremented and the entire process is repeated.

Turbine blades are tested across their entire pitch range, starting at low pitch and working towards the maximum pitch angle. At the lower and higher ranges of blade pitches, slower turbine speeds are expected and blade pitches are tested in increments of three to five degrees. Near a pitch angle of 0 degrees, the pitch increment is reduced to one to two degrees.

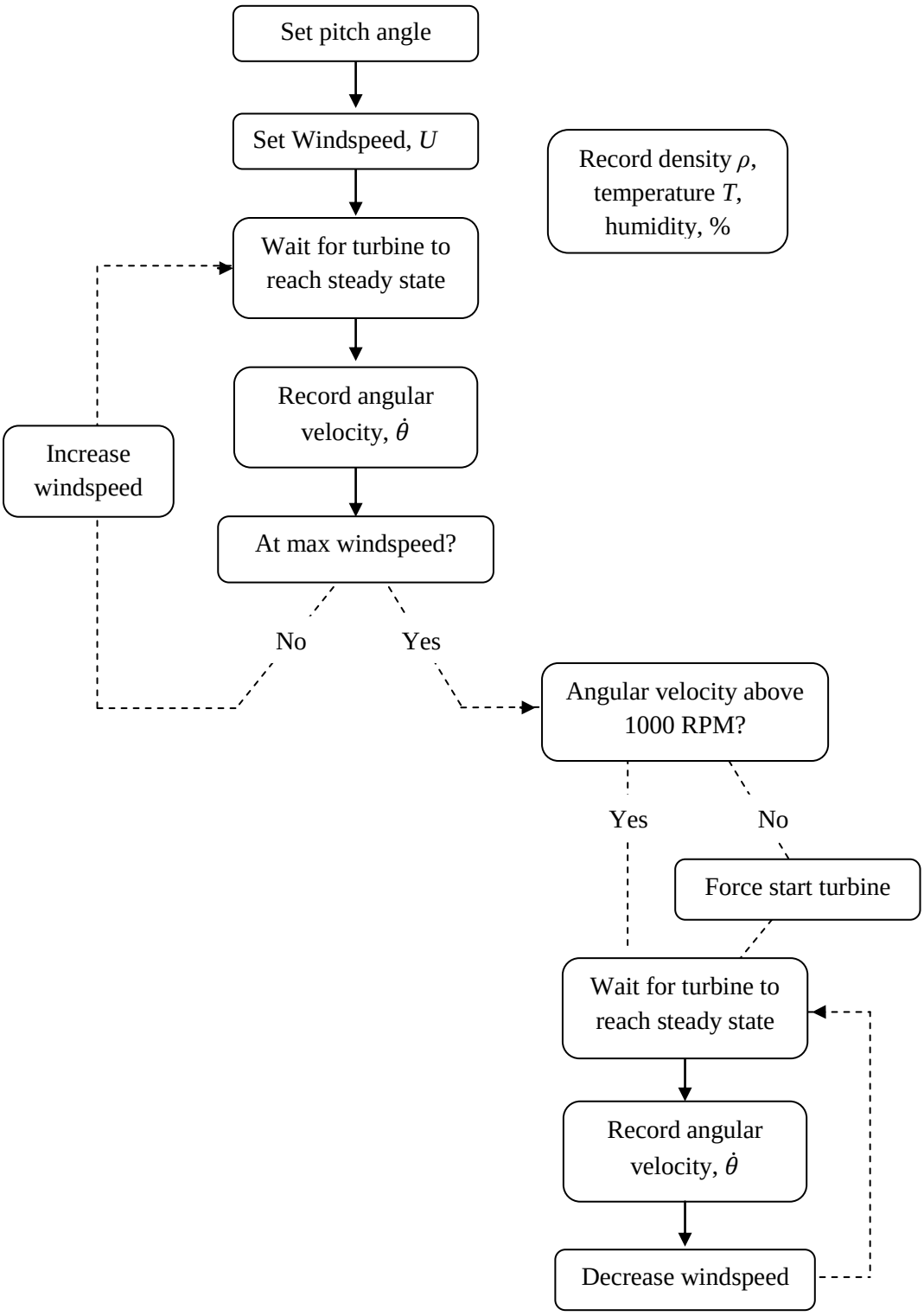

Figure 2.11. Flowchart of experimental procedure for a pitch study.

Coefficient of power C_P studies are carried out in a similar fashion to pitch studies, except at only one pitch angle. A flowchart depicting each step is in Figure 2.12, while Figure 2.13 also includes the instrumentation that is used to perform each step.

Cp studies are started with the smaller HB 2-5-2 brake attached. The current supply and multimeter are powered on and set to zero current. The wind tunnel is set to the lowest testing windspeed, typically 3 m/s, and the turbine is allowed to reach steady state, which is the same steady state observed at this pitch and windspeed during the pitch study. After the angular velocity and applied current are recorded in a testing matrix, the current is increased and the process is repeated until the turbine reaches its stall torque and stops rotating, or the small brake needs to be replaced with the large one. More data points in smaller increments are taken near the stall torque to obtain an accurate stall torque. This process is repeated for each windspeed. Figure 2.14 illustrates an example C_P curve with annotations.

A self-start test was methodically done to capture the self-starting capability of mini-turbines with different blades. A custom-designed 3-D printed protractor, shown in Figure 2.15, was used to measure the starting angle of the turbine relative to the freestream velocity, and then gently released to observe if the turbine self-started. A “Y” or “N” was recorded and then compiled for a range of windspeeds. The starting angles tested were 0 – 120 degrees since the mini-turbines with three blades are symmetric about 120 degrees. The pointer is referenced by one of the rods that extrudes from the blade and through the endplate.

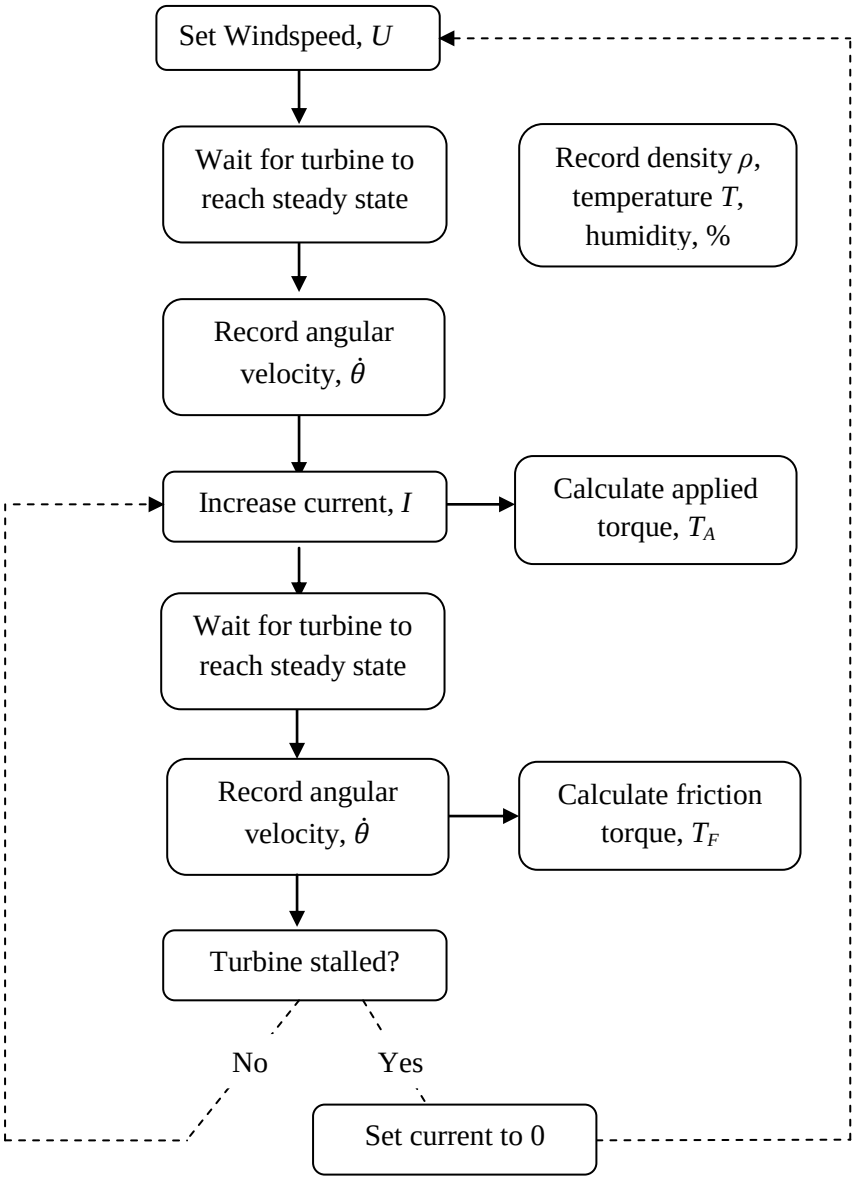

Figure 2.12. Flowchart of experimental procedure for a Cp test. Torque is slowly applied to a free-spinning turbine until the turbine "stalls" and can no longer overcome the total torque of the system.

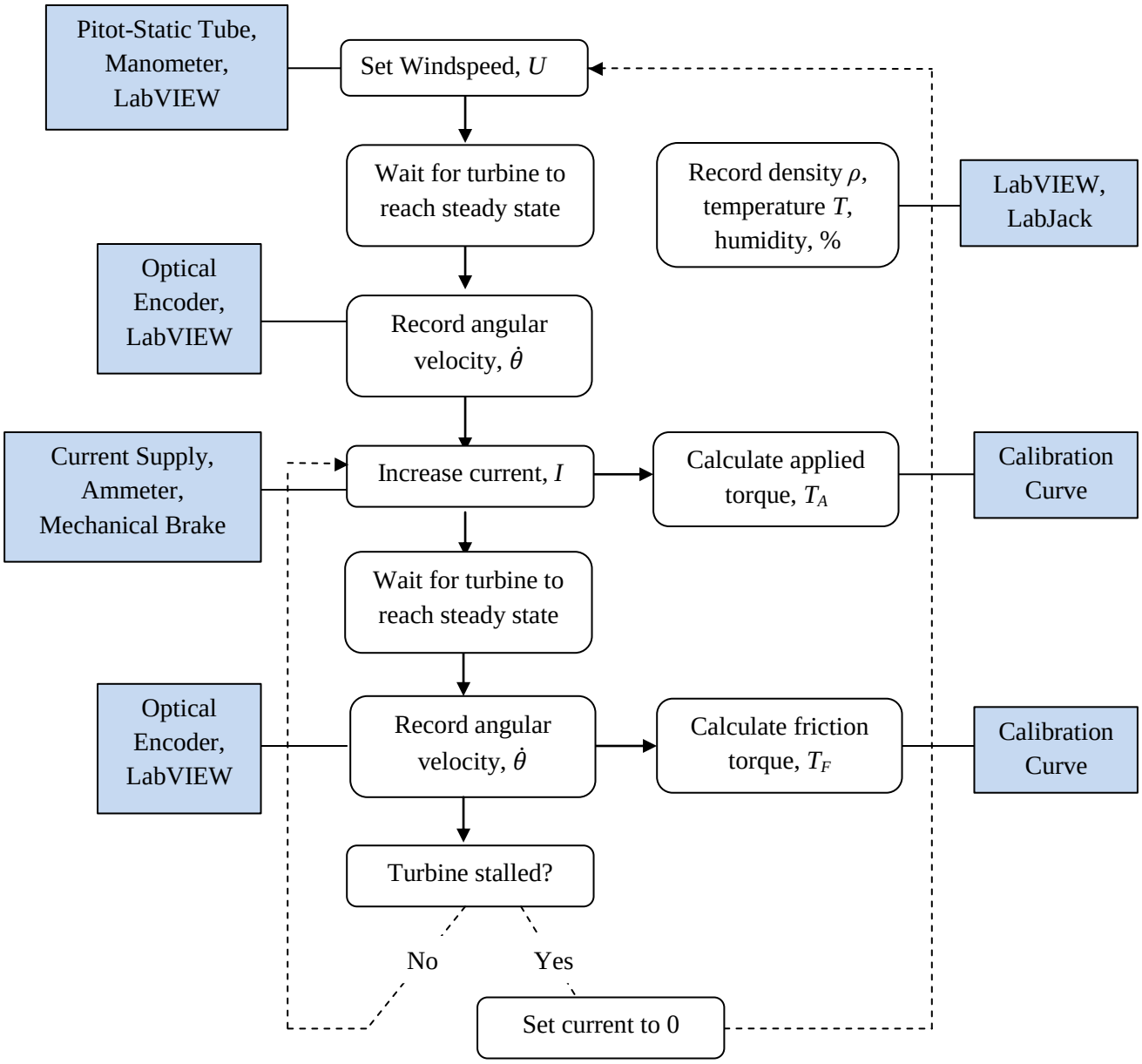

Figure 2.13. Flowchart of experimental procedure for a Cp test. Shaded boxes indicate instruments used to perform step. Torque is slowly applied to a free-spinning turbine until the turbine "stalls" and can no longer overcome the total torque of the system.

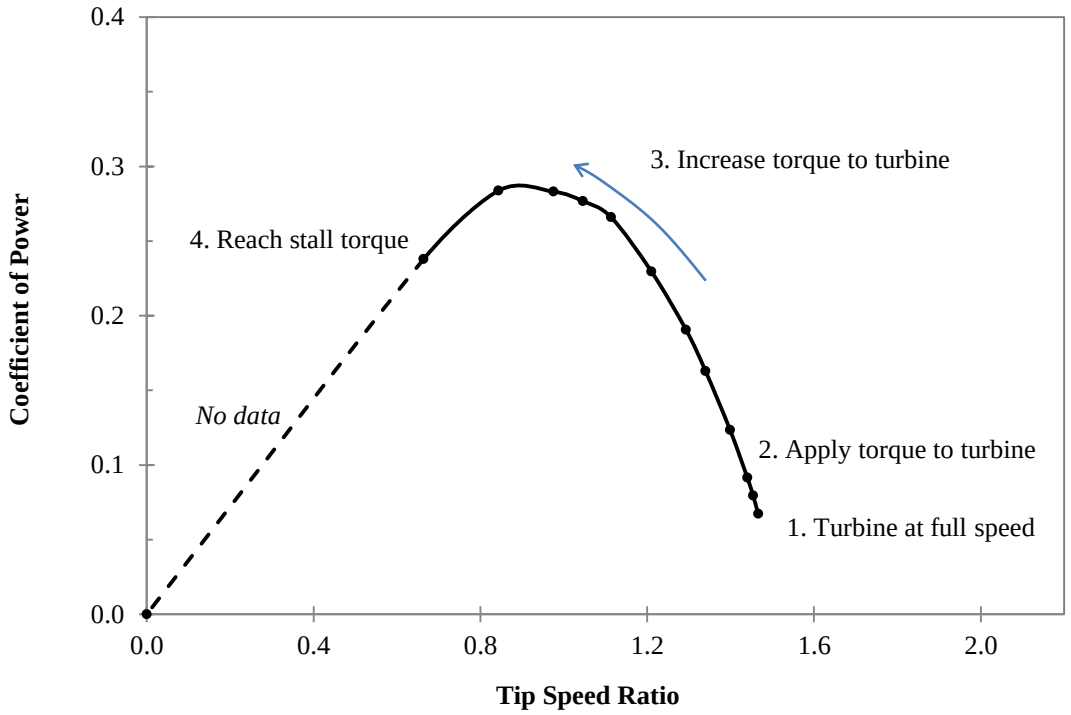

Figure 2.14 – **Coefficient of Power vs Tip Speed Ratio Example of Testing Procedure**. Testing begins with (1) the turbine spinning at full speed (no torque applied) then (2) applying torque to the turbine. The tip speed ratio of the turbine decreases as (3) applied torque increases. At (4) the stall torque, the turbine no longer operates. Decreasing the torque at this point will return the turbine to a previous steady state operating point.

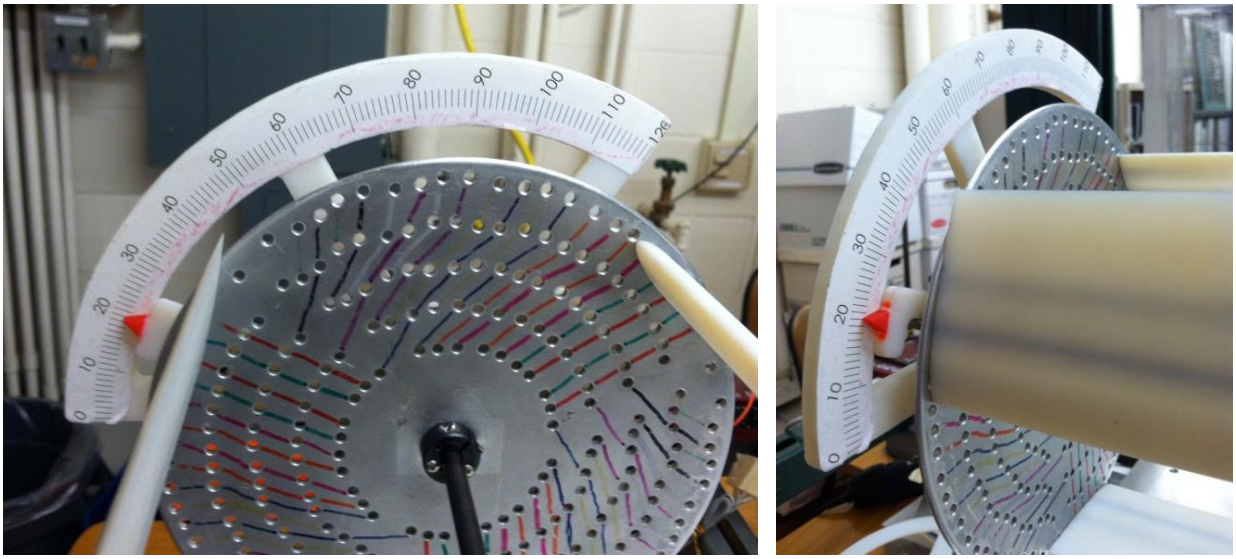

Figure 2.15. Custom designed 3-D printed protractor used to set the starting angle for self-start tests. The rod that secures the blade is used as a reference point.

2.6 Uncertainty Analysis

An uncertainty and repeatability analysis was conducted to ensure that results and instrumentation are statistically sound. Both the biased and random uncertainties were determined on the quantities of interest, the coefficient of power C_P and tip speed ratio TSR, shown in Equations 2.4 and 2.5 below.

$$C_P = \frac{T\dot{\theta}}{\frac{1}{2}\rho U^3 DL} \qquad (2.4) \qquad\qquad TSR = \frac{R\dot{\theta}}{U} \qquad (2.5)$$

where T is the total torque in the steady state system, $\dot{\theta}$ is the angular velocity, ρ is the density of air, U is the freestream velocity, D is the turbine diameter, R is the turbine radius, and L is the length of the turbine. Each of the quantities in Equations 2.4 and 2.5 has an associated measurement error, listed in Table 2.6.

Table 2.6. Bias (Measurement) Error

Parameter	**Error (+/-)**	**Parameter**	**Error (+/-)**
Angular Velocity, Ω	5 RPM	Density, ρ	0.001 kg/m^3
Blade length, L	2 mm	Windspeed, U	0.25 m/s
Turbine Diameter, D	2 mm	Applied Torque, T_A	0.5 mNm
Turbine Radius, R	1 mm	Friction Torque, T_f	0.5 mNm

To calculate the biased uncertainty of the aggregated terms C_P and TSR, the measurement error was propagated by the root-sum-squares method. The governing equation for this method is shown in Equation 2.6, with f being an aggregate function and x_n being measured variables.

$$\Delta f(x_1, x_2, \dots, x_n) = \left[\left(\left|\frac{\partial f}{\partial x_1}\right| \Delta x_1\right)^2 + \left(\left|\frac{\partial f}{\partial x_2}\right| \Delta x_2\right)^2 + \dots + \left(\left|\frac{\partial f}{\partial x_n}\right| \Delta x_n\right)^2\right]^{\frac{1}{2}} \qquad (2.6)$$

The partial derivative determines the sensitivity of the primary function with respect to each variable, and multiplies it with the uncertainty of each variable's measurement. For the functions C_P and TSR, Equation 2.6 becomes Equations 2.7 and 2.8.

$$\Delta TSR = \left[\left(\left|\frac{\partial TSR}{\partial \dot{\theta}}\right| \Delta\dot{\theta}\right)^2 + \left(\left|\frac{\partial TSR}{\partial U}\right| \Delta U\right)^2 + \left(\left|\frac{\partial TSR}{\partial R}\right| \Delta R\right)^2\right]^{1/2} \tag{2.7}$$

$$\Delta C_P = \left[\left(\left|\frac{\partial C_P}{\partial \dot{\theta}}\right| \Delta\dot{\theta}\right)^2 + \left(\left|\frac{\partial C_P}{\partial T}\right| \Delta T\right)^2 + \left(\left|\frac{\partial C_P}{\partial \rho}\right| \Delta\rho\right)^2 + \left(\left|\frac{\partial C_P}{\partial U}\right| \Delta U\right)^2 + \left(\left|\frac{\partial C_P}{\partial D}\right| \Delta D\right)^2 + \left(\left|\frac{\partial C_P}{\partial L}\right| \Delta L\right)^2\right]^{1/2} \tag{2.8}$$

Equations 2.7 and 2.8 are evaluated and the measurement error values from Table 2.6 on the previous page are substituted to give the total bias error. An example C_P vs TSR curve with bias error bars is shown in Figure 2.16 on the next page.

The random uncertainty was determined from the bootstrap method. For this analysis, the measurements for each data point were repeated for a bin size of 30-40 samples. The bootstrap function then created a new data sample by randomly selecting raw data with replacement. This process was repeated for 1000 data samples to uncover the range of possible values from the raw samples. The results of this analysis are shown in Figure 2.17.

The total uncertainty for this experiment is the sum of the biased and random uncertainty. Figure 2.18 shows the result of this summation, along with three other experiments that were done with the same turbine parameters but at different times of the year and different users conducting the experiment. The repeatability of the experiments is clear in the agreement of the experiments with the error bars. There is more agreement in the lower windspeeds, as shown in Figure 2.19. This shows our experiments have low uncertainty and high repeatability.

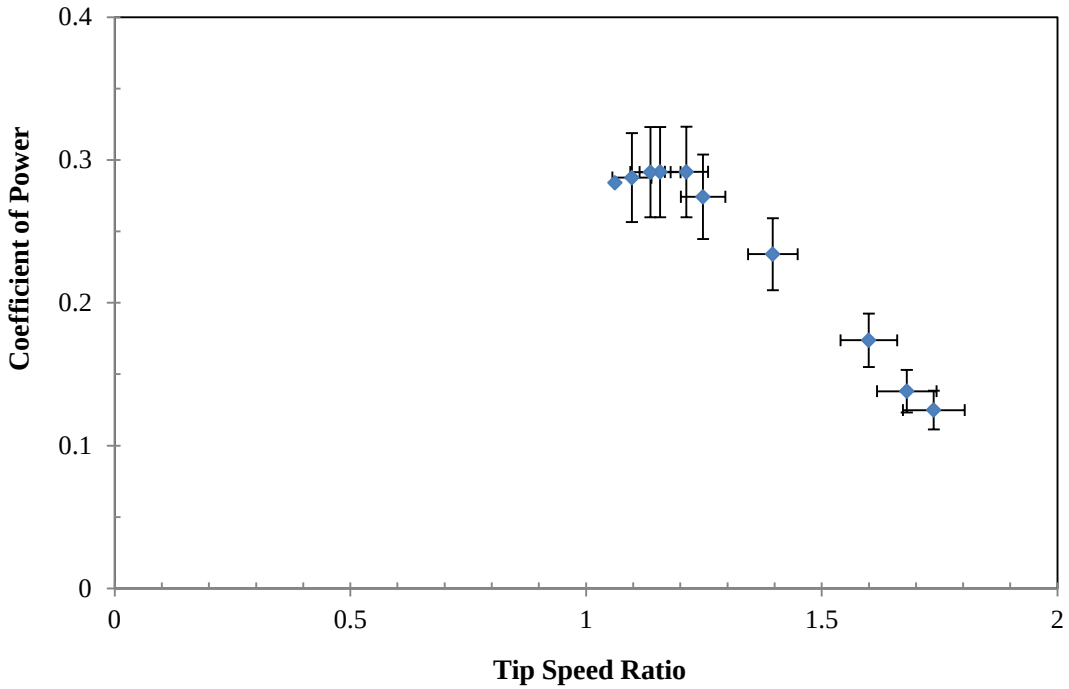

Figure 2.16. Bias uncertainty for a C_P vs TSR curve. Measurement uncertainties were propagated using the root-sum-squares method. Experimental parameters: NACA 0015, chordlength 6cm, windspeed 7 m/s.

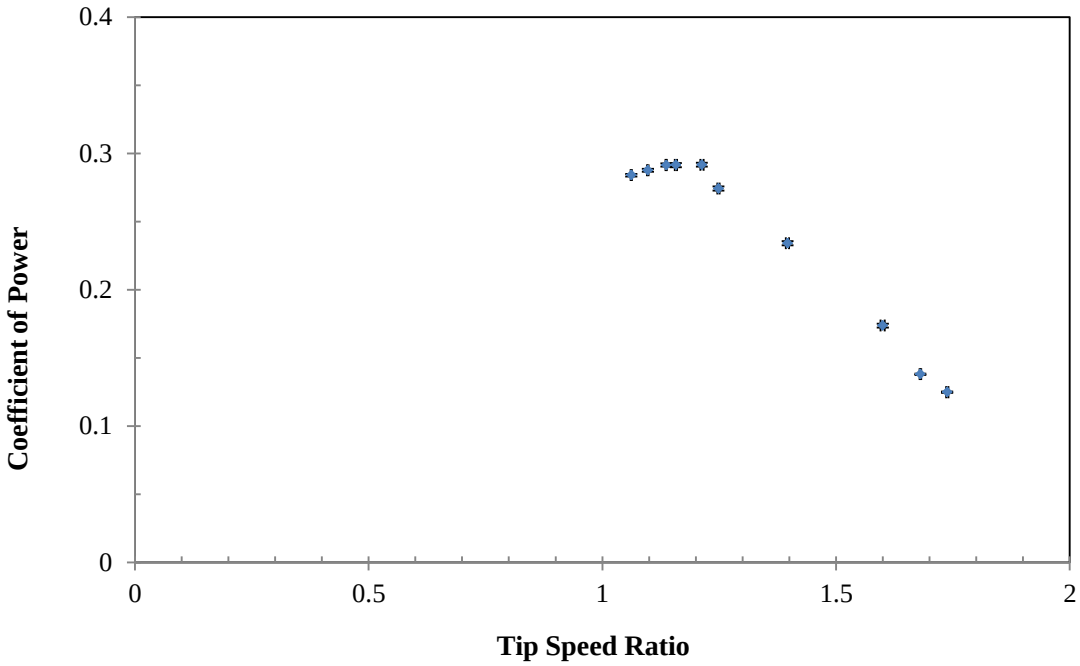

Figure 2.17. Bootstrap uncertainty for a C_P vs TSR experiment is very small. Number of random samples: 1000; original data size: 30-40. Experimental parameters: same as Figure 2.10.

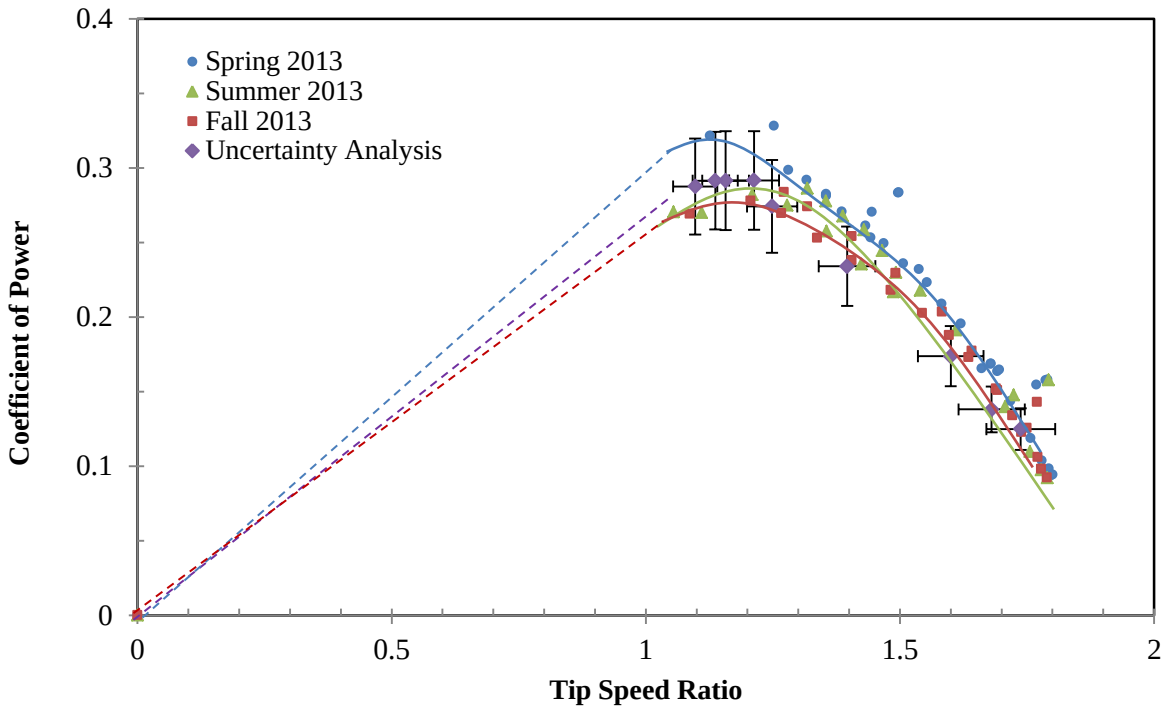

Figure 2.18. Total uncertainty and repeatability of the mini-turbine experiments for same parameters: NACA 0015, chordlength 6 cm, windspeed 7 m/s.

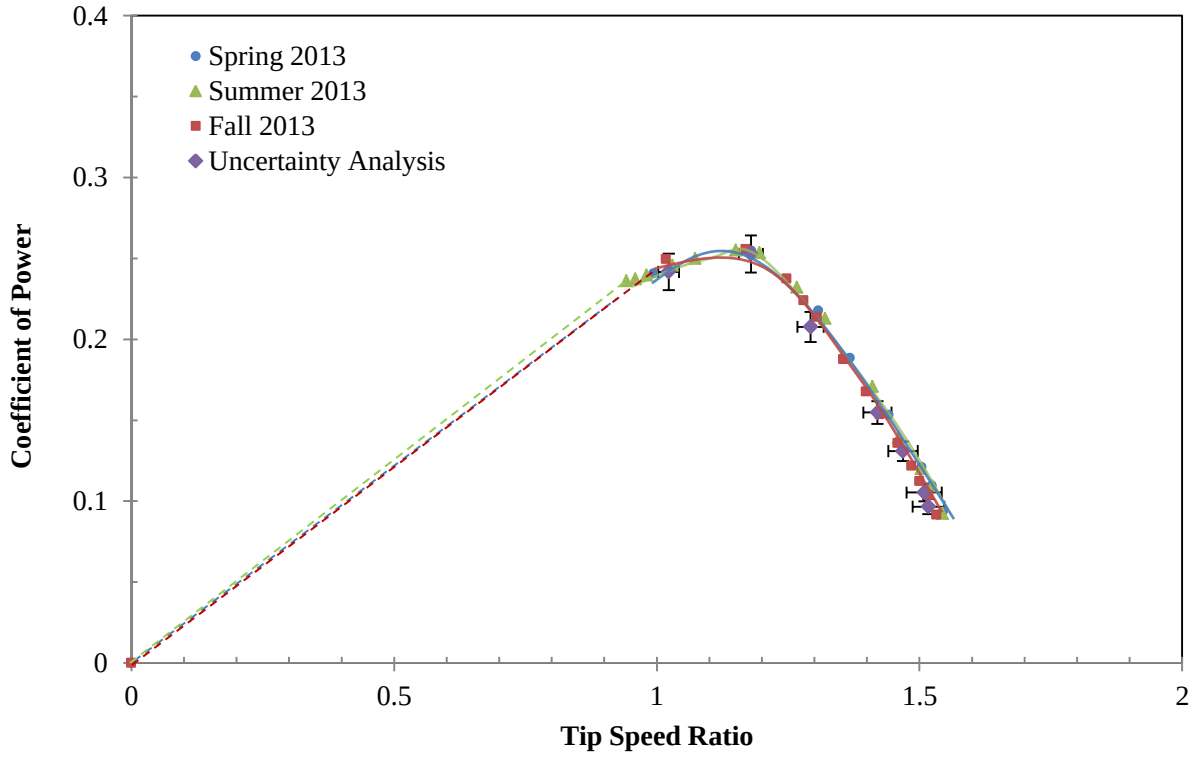

Figure 2.19. Repeatability of mini-turbine experiments is better at a windspeed of 4 m/s. Parameters: NACA 0015, chordlength 6 cm.

3. Straight Blades

This section will discuss the results of the different experiments done on straight blades. The design parameters tested were the offset pitch angle, the ratio of the chordlength of the blade to the diameter of the turbine (c/D), camber, and thickness.

3.1 Pitch Study

The first design parameter investigated was the offset pitch angle of the turbine blades. The offset pitch angle β is defined as the angle between the midchord of the blade and the turbine circumference, as shown in Figure 3.1 below.

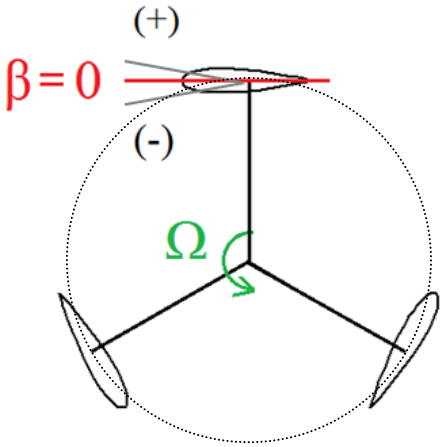

Figure 3.1. Schematic of the offset pitch angle β, the angle at which the chordline of the blade is parallel to the tangent of the turbine circumference at the midchord point

A pitch study was done on the big, medium, and small blades. The results of the pitch study are shown in Figures 3.2 to 3.4. Figure 3.2 shows the free-spinning turbine speed and tip speed as a function of offset pitch angle for the small, medium, and big blades for a windspeed of 6 m/s. All three blade sizes have a peak turbine speed at an offset pitch angle of 0 degrees, which

is unexpected. The different size blades have comparable turbine speeds, though there is a slight trend of decreasing and wider peaks with increasing chordlength.

Figure 3.3 shows the pitch study results for the medium blades for a range of windspeeds. When the turbine speed is non-dimensionalized with the freestream velocity, the resultant data of TSR vs pitch angle collapses into one curve. Loading the mini-turbine does not change the optimal offset pitch angle, as shown in Figure 3.4. The coefficient of power is greatest for a pitch angle of 0 degrees for the medium blades.

As described in the experimental methods section, certain turbine configurations can have two operating regions. Figure 3.5 compares two techniques: Slow start (no assistance) and Forced start (apply Dremel drill to 1000 RPM) for the small, medium, and big blades. At extreme offset pitch angles, the turbine is unable to produce enough thrust to spin at the higher operating region. However, force starting the mini-turbine at a low pitch angle with a Dremel drill elevates the turbine speed to higher speeds than when the mini-turbine is left to slow start. At pitch angles near 0 degrees, the mini-turbine with no assistance can reach the same speeds as the turbine that was forced. The ability of the mini-turbine to reach higher operating speeds with no assistance when the pitch angles is 0 degrees supports the finding that this is the optimal pitch angle. This feature was evident at all windspeeds for big and medium blades, and at a windspeed of 8 m/s for small blades. For windspeeds less than 8 m/s, the small blades are unable to reach the higher operating region without assistance.

The experiments of Templin (1972) with a 14ft diameter eggbeater Darrieus turbine with NACA 0012 blades showed a similar phenomenon of two operating levels. The Templin turbine would self-start when it was disconnected from the motor but only spin up to 13 RPM. However,

when assisted by the motor to 65 RPM and released, the turbine would accelerate rapidly to a free-running speed of 213 RPM. The c/D ratio was 0.04 and tests were done in a controlled wind tunnel. This similarity implies that Darrieus turbines have a band of negative torque at low TSR that must be overcome before reaching a higher operating level. For the mini-turbines, extreme offset pitch angles are unable to provide enough thrust to overcome the negative torque.

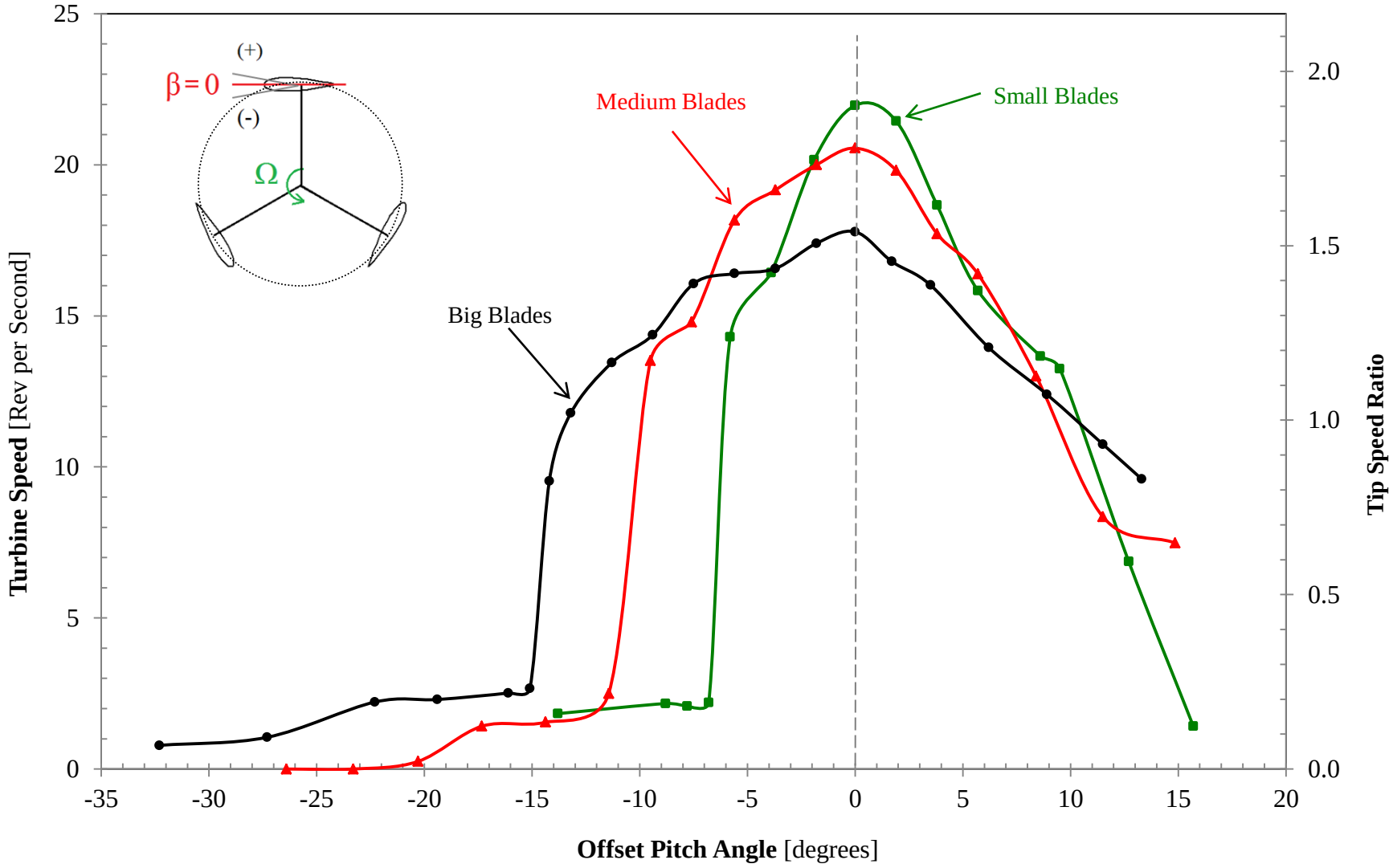

Figure 3.2. **Turbine Speed and Tip Speed Ratio vs Pitch Angle** for small, medium, and big blades with at a windspeed of 6 m/s.
Big blades: NACA 0015, chordlength 8 cm; Medium blades: NACA 0015, chordlength 6 cm; Small blades: NACA 0018, chordlength 4 cm.

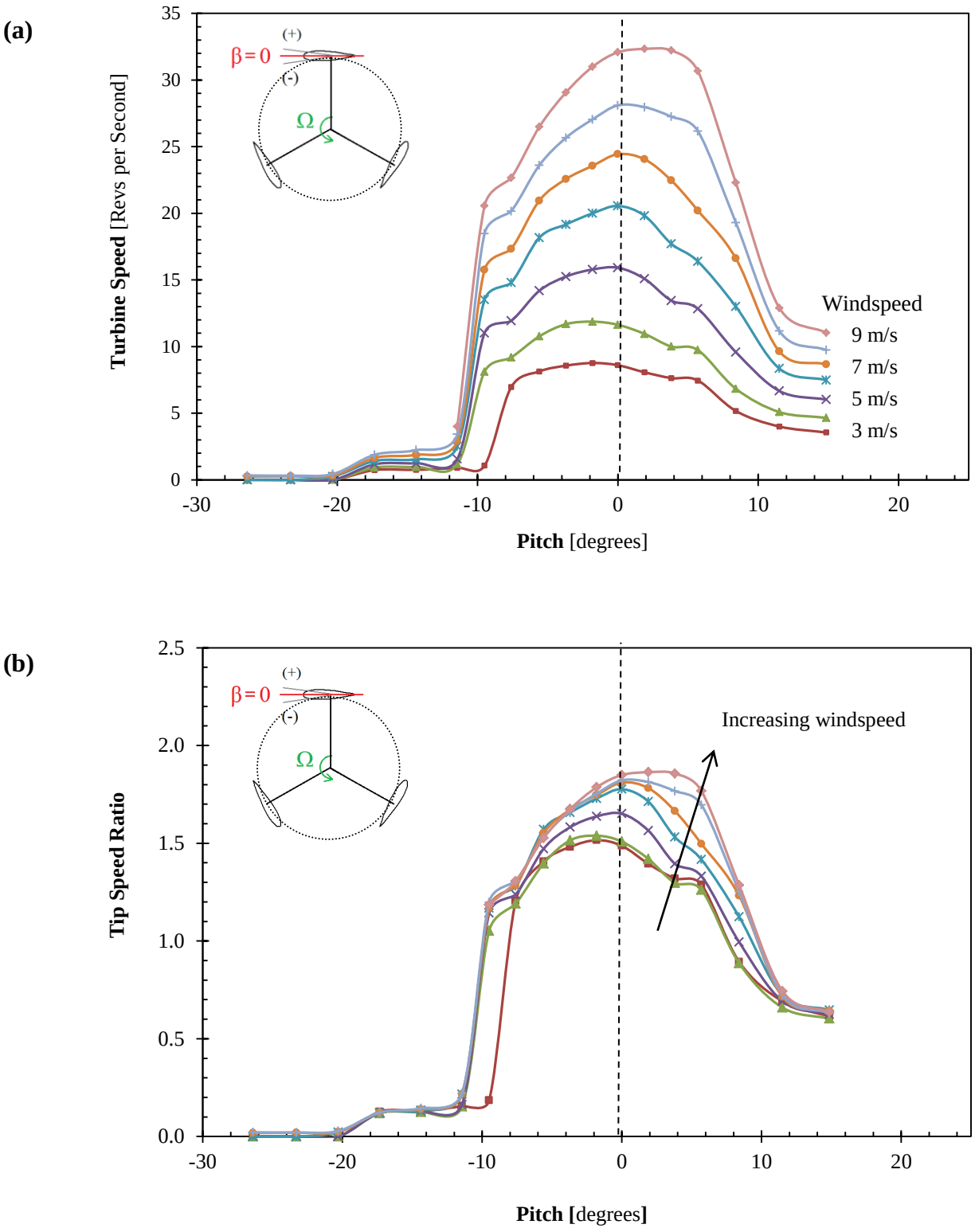

Figure 3.3. **(a) Turbine Speed vs Pitch Angle** and **(b) Tip Speed Ratio vs Pitch Angle** for medium blades at a windspeed of 6 m/s. When turbine speed is non-dimensionalized, data collapses into one curve reasonably well.

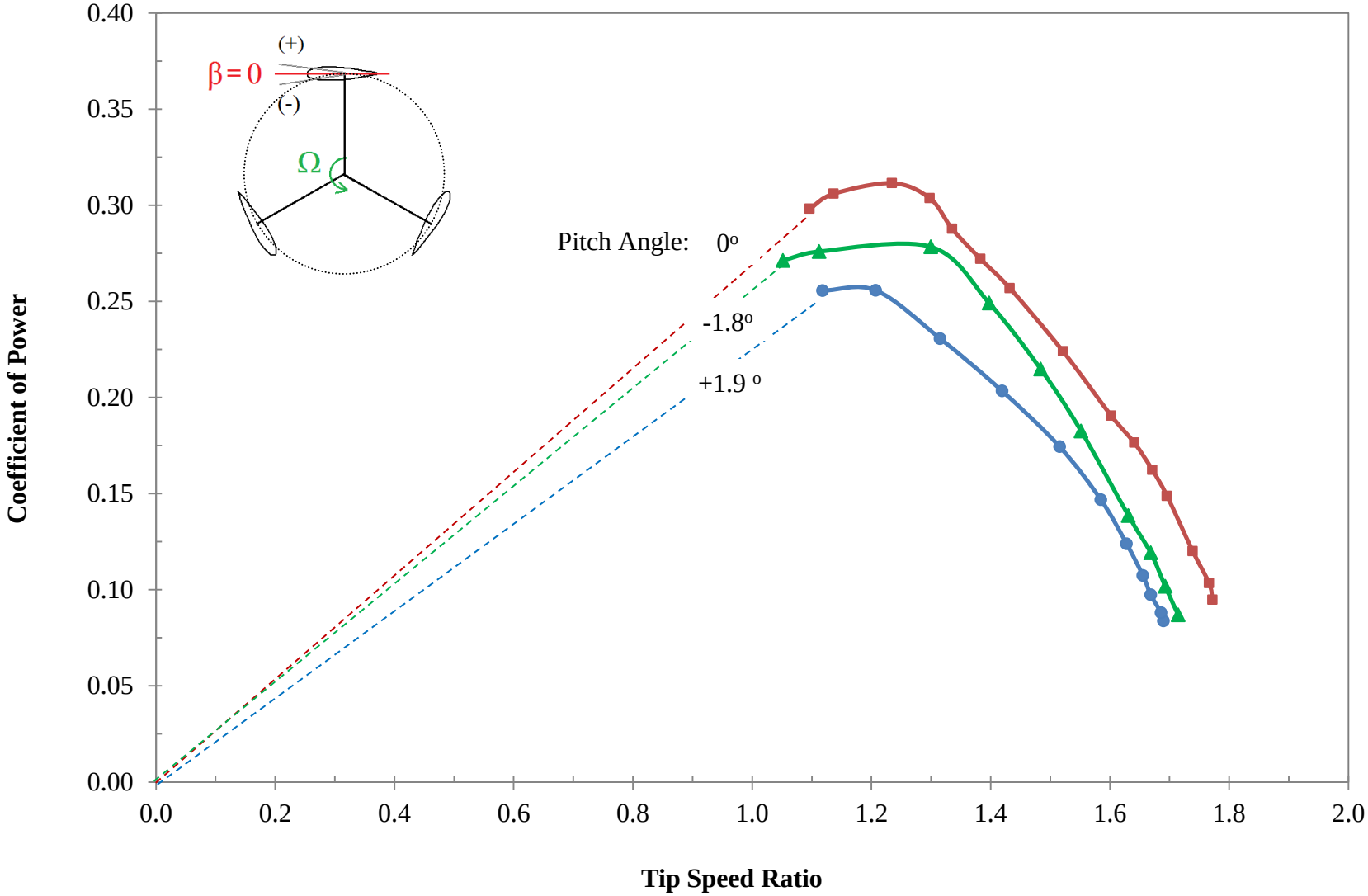

Figure 3.4. Coefficient of Power vs Tip Speed Ratio for medium blades at different pitch angles. Loading the mini-turbine does not change the optimal pitch angle. Parameters: Medium blades (NACA 0015, chordlength 6 cm) at a windspeed of 6 m/s.

(a) Small blades

NACA 0018
chordlength: 4 cm

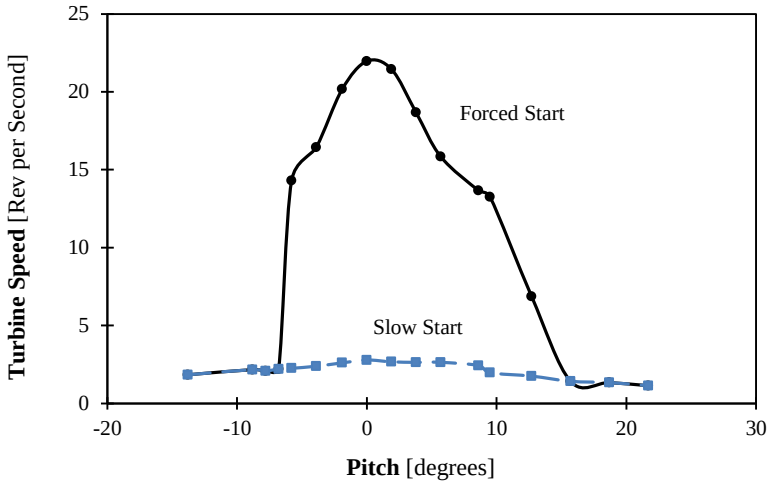

(b) Medium blades

NACA 0015
chordlength: 6 cm

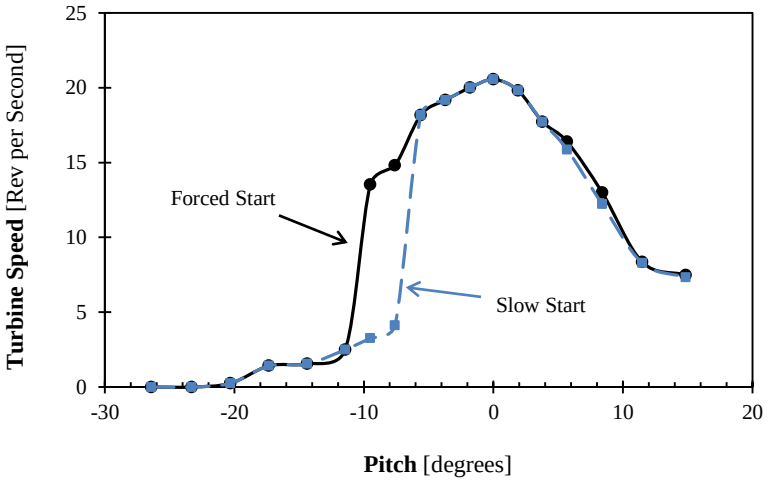

(c) Big blades

NACA 0015
Chordlength: 8 cm

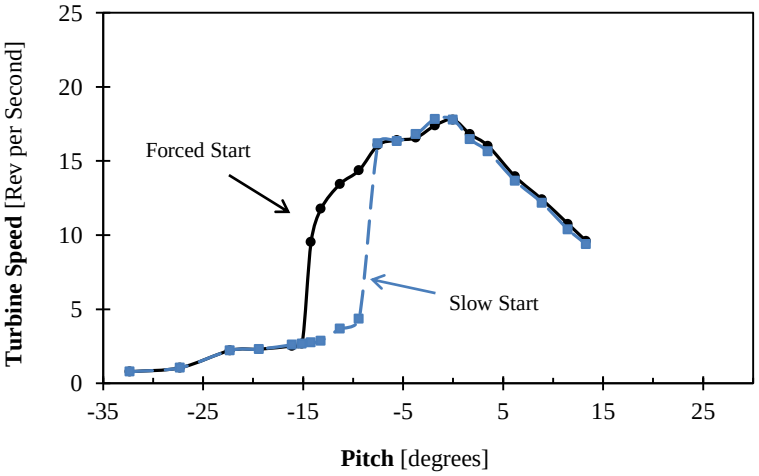

Figure 3.5. Turbine Speed vs Pitch Angle for (a) small blades (b) medium blades and (c) big blades at a windspeed of 6 m/s. Force starting the mini-turbine increases the turbine speed at smaller pitch angles. Small blades are unable to slow start to higher operating speeds at this windspeed.

3.2 c/D study

A coefficient of power C_P study was conducted for the big, medium, small, and micro blades to investigate the effect of the ratio of the chordlength of the blade to the diameter of the turbine (c/D) when the turbine is loaded. Results from the C_P studies are shown in Figures 3.6 to 3.8 as a function of tip speed ratio TSR. TSR is the ratio of the tangential velocity to the freestream velocity.

A comparison of all blade sizes for a windspeed of 8 m/s is shown in Figure 3.6. The big blades produce a maximum C_P of approximately 0.3 at TSR = 1.0, while the medium blades produce a maximum C_P of approximately 0.35 at TSR = 1.2. In contrast, the small blades reach a maximum C_P of approximately 0.19 at TSR = 1.6. The micro blades perform approximately an order of magnitude less efficiently than the small blades, with a maximum C_P of 0.006 at TSR = 0.15. These results exemplify how small c/D ratios, characteristic of the small and micro blades, on this size scale (i.e. at low Reynolds numbers) do not offer peak power efficiency as they do on larger scale turbines. In addition, the TSR operating ranges for the mini-turbines are lower than the large Reynolds number turbines.

Several trends are observed from Figure 3.6. Peak power efficiency is generated by some blade size between the big and small blades tested, as the medium blades performed more efficiently than both. Micro blades perform more poorly than all other blade configurations, and never reach an angular velocity or C_P comparable to the other blades. Except for the micro blades, with increasing blade sizes, the TSR at which maximum power generation occurs decreases. This trend is seen through the location along the x-axis of the peaks of the three C_P curves in Figure 3.6. The reason for this is not yet understood, but it is remarkable that the big

blades operate at their peak efficiency at such low TSRs, much lower than the TSR regime of large scale high Reynolds number turbines. Both big and small blades exhibit the wider peak operating ranges than the medium blades, which offer some advantage to practical power generation in varying flow conditions.

Figure 3.7 shows results of a C_P experiment for a range of windspeeds for both big and medium blades. For both blade sizes, the data collapses reasonably well. However, there remains a gradual increasing trend of C_P as Reynolds number increases.

For practical illustration, the maximum dimensional power output of the different blade sizes for a range of windspeeds is shown in Figure 3.8. Both the medium and big blades perform similarly in terms of maximum power generation in Watts under realistic slow start conditions, generating 4 Watts at the highest windspeed tested. This is about 60% of the Betz limit. However, the small blades produce approximately 30-40% less power than big and medium blades. Furthermore, the small blades require a forced start at windspeeds less than 7 m/s to be comparable to the big and medium blades, which is not practical. Without a forced start, they operate closer to the micro blades, which do not produce any significant power.

In summary, the results from the C_p studies indicate that relatively large blade sizes (c/D = 0.36 and 0.48) produce power more efficiently and impactfully. The maximum power is produced at unexpectedly lower values of TSR than large scale turbines (where maximum power typically occurs at TSR = 2 – 4). Furthermore, peak power appears to be obtained at decreasing TSR values as blade size (c/D) increases.

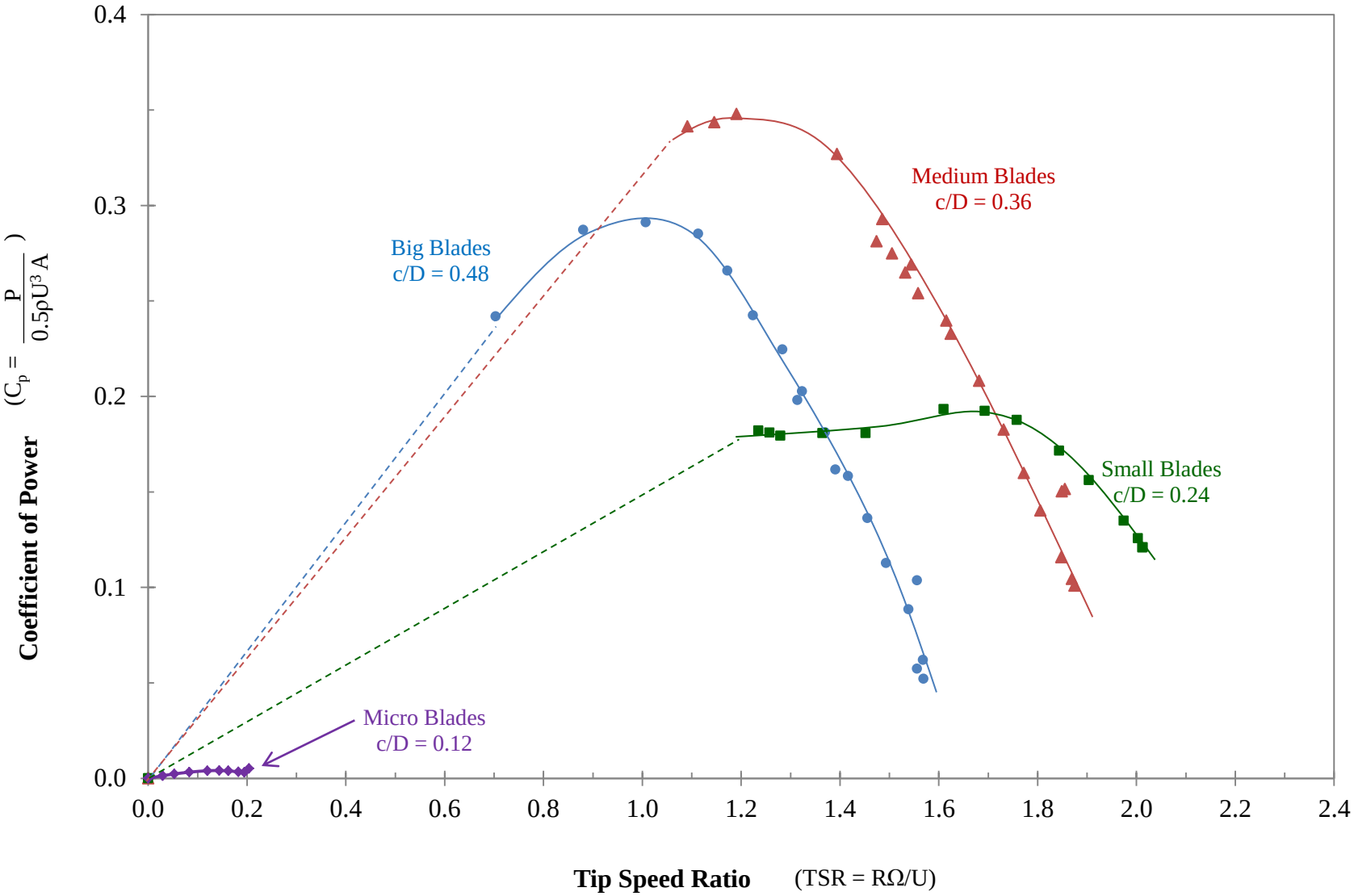

Figure 3.6. **Coefficient of Power vs Tip Speed Ratio** for big, medium, small, and micro blades at a windspeed of 8 m/s. Big blades: NACA 0015, chordlength 8 cm, c/D = 0.48; Medium blades: NACA 0015, chordlength 6 cm, c/D = 0.36; Small blades: NACA 0018, chordlength 4 cm, c/D = 0.24; Micro blades: NACA 0021, chordlength 2 cm, c/D = 0.12. Micro blades do not operate at low Reynolds number mini-turbines.

(a)

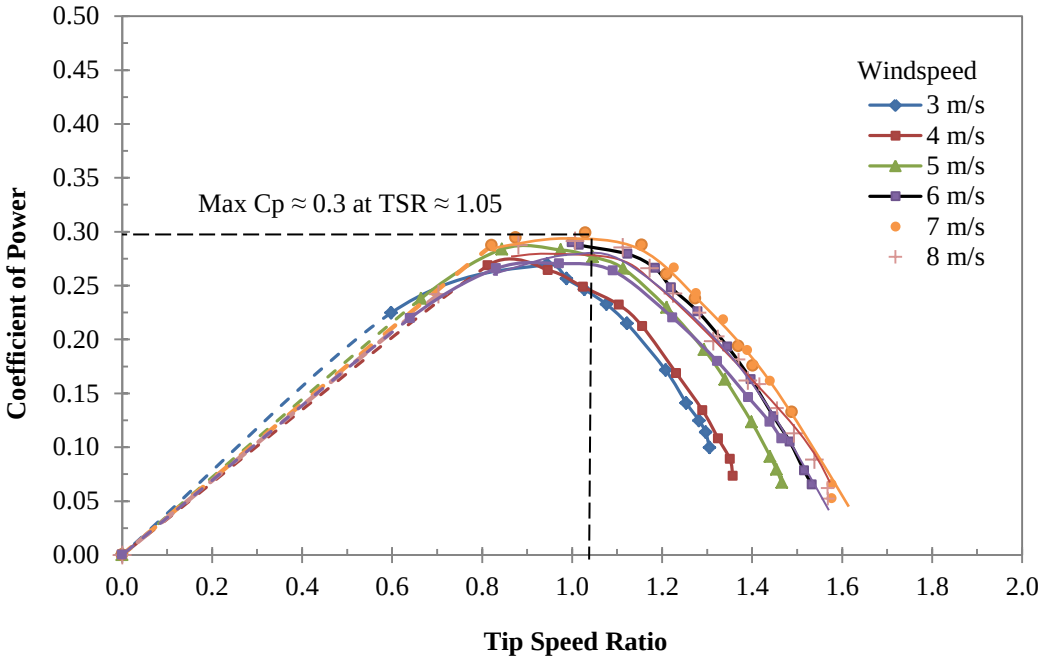

(b)

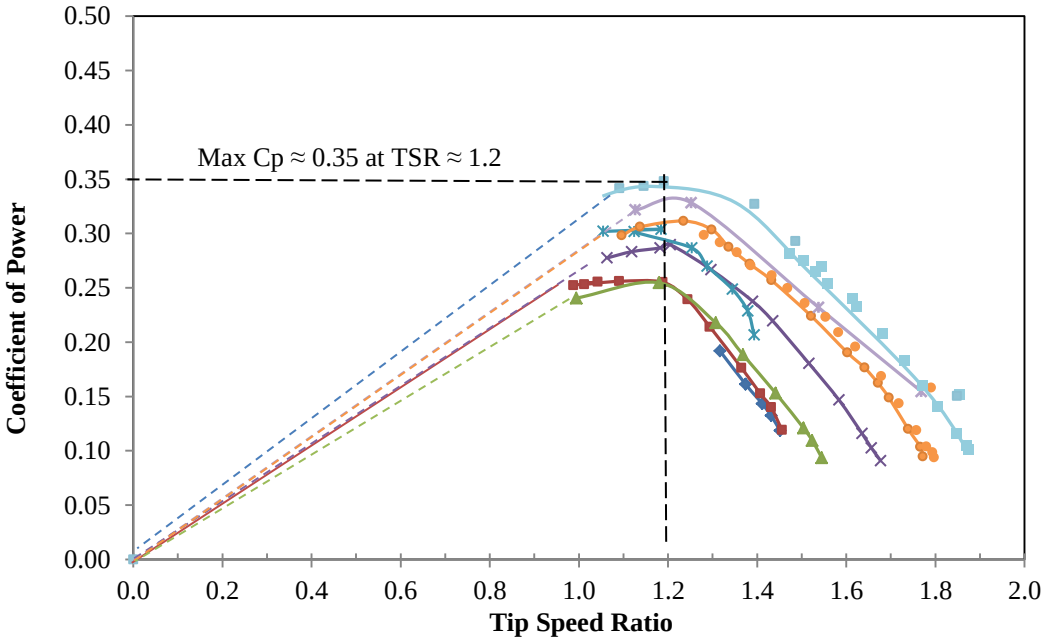

Figure 3.7. **Coefficient of Power vs Tip Speed Ratio (a)** Big blades (NACA 0015, c/D = 0.48) at windspeeds 3-8 m/s. Max Cp ~ 0.30 at TSR = 1.05. **(b)** Medium blades (NACA 0015, c/D = 0.36) at windspeeds 3-8 m/s. Max Cp ~ 0.35 at TSR = 1.2.

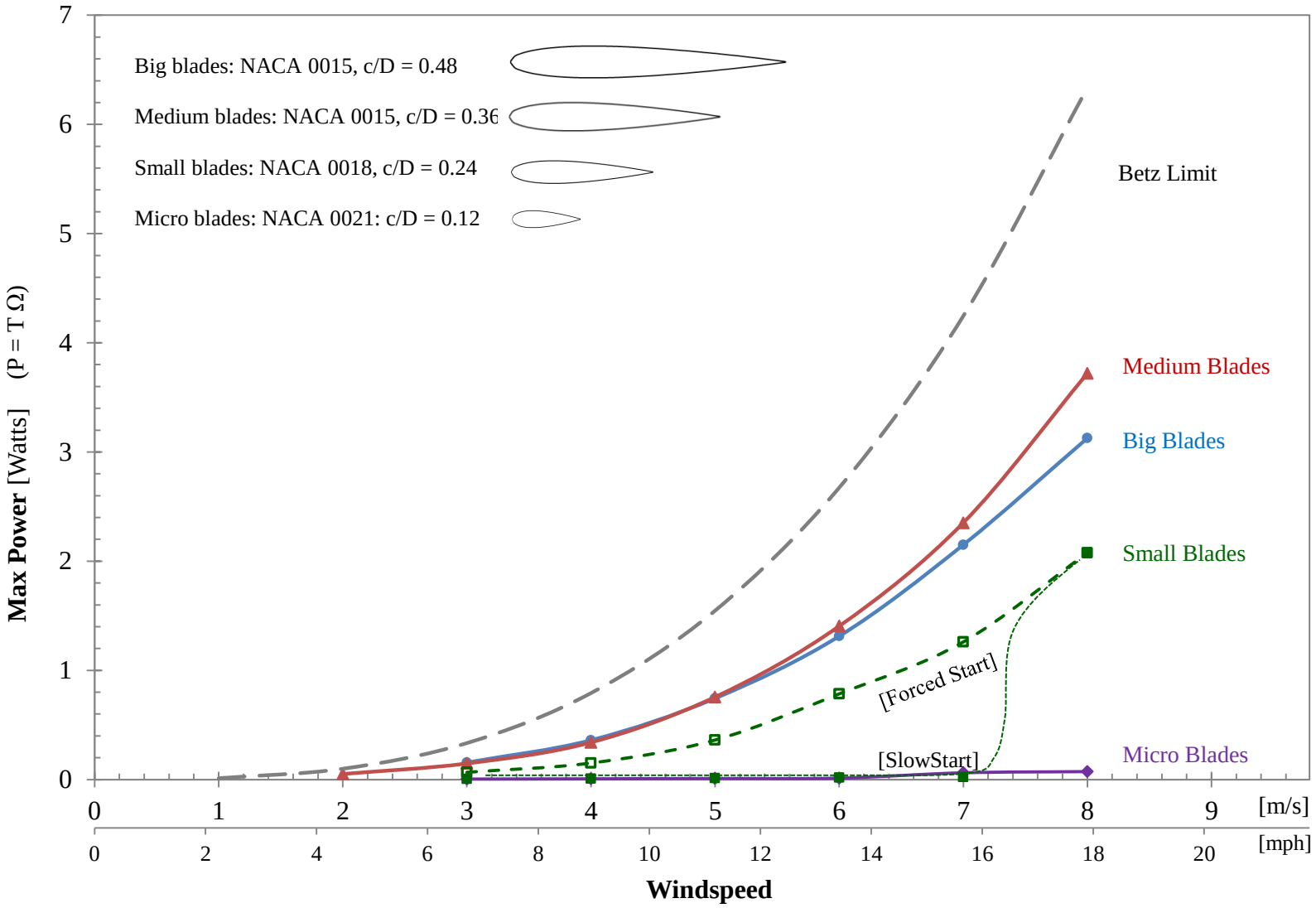

Figure 3.8 – **Maximum Dimensional Power vs Windspeed** for big, medium, small, and micro blades compared to the theoretical Betz efficiency limit. Big and medium blades are comparable for all windspeeds. Small blades only produce usable power when given a forced start or at a windspeed of 8 m/s, otherwise their performance is as poor as the micro blades.

3.3 Camber Study

A range of cambered blades were tested to try to increase the power generation of the mini-turbines. To isolate the effect of camber, all blades tested had a chordlength of 6 cm and a thickness of 15%, the same as the symmetric NACA 0015 medium blades. The medium blades were chosen because they were the highest performing blade of all the sizes tested up to this point. The camber of the airfoil increases the lift coefficient at low angles of attack, and was predicted to perform better than the symmetric blades. Increases in the drag coefficient were neglected because they occur at high angles of attack on the downstream side of the turbine where there is already reduced torque due to blade wake interference.

The effects of camber were tested with the camber direction facing either concave-in or concave-out, as illustrated in Figure 3.9 below. The concave-out configuration has the potential to offset flow curvature effects, allowing the flow to "see" a virtual airfoil that performs better than the symmetric blade. Flow curvature theory takes an airfoil in curvilinear flow (such as in a VAWT) and "straightens" the flow into a rectilinear frame, thereby imposing an effective camber and incident angle onto the airfoil (Migliore, Wolfe, & Fanucci 1980).

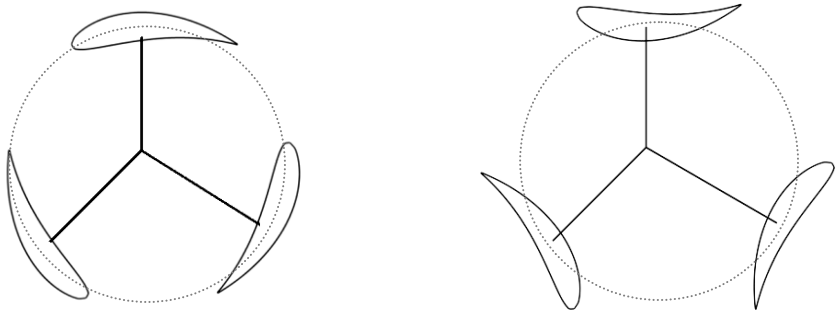

(a) Concave-In **(b) Concave-Out**

Figure 3.9. Cambered blades in two configurations (a) Concave In and (b) Concave Out

Figure 3.10 shows the results of a C_P study with cambered blades compared to the symmetric blades at a windspeed of 8 m/s. Despite the NACA 4415 concave-in blades obtaining similar turbine speeds to their symmetric counterpart when unloaded, their C_P curve is consistently around 30% lower than that of the symmetric blades. At higher windspeeds of 7-8m/s, the concave-out blades performed as well or better than the concave-in blades; however, at windspeeds lower than 7 m/s, they produced C_P values lower than the concave-in blades. The NACA 4415 and 6415 blades have comparable C_P, but the NACA arc-15 performs much poorer. All blades show a peak power generation at approximately the same TSR of 1.2 as the symmetric blades, and all exhibited the same width of the operating region. An interesting note is that the concave-out and symmetric blades have the same slope at TSRs $\geq$ 1.2, while the concave-in blades have a more gradual slope.

In summary, cambering an airfoil in either concave-in or concave-out configuration showed detrimental effects on power generation compared to symmetric airfoils with the same thickness. As camber increases, the detriment also increases. This result is similar to those of Yamada et al (2011).

(a)

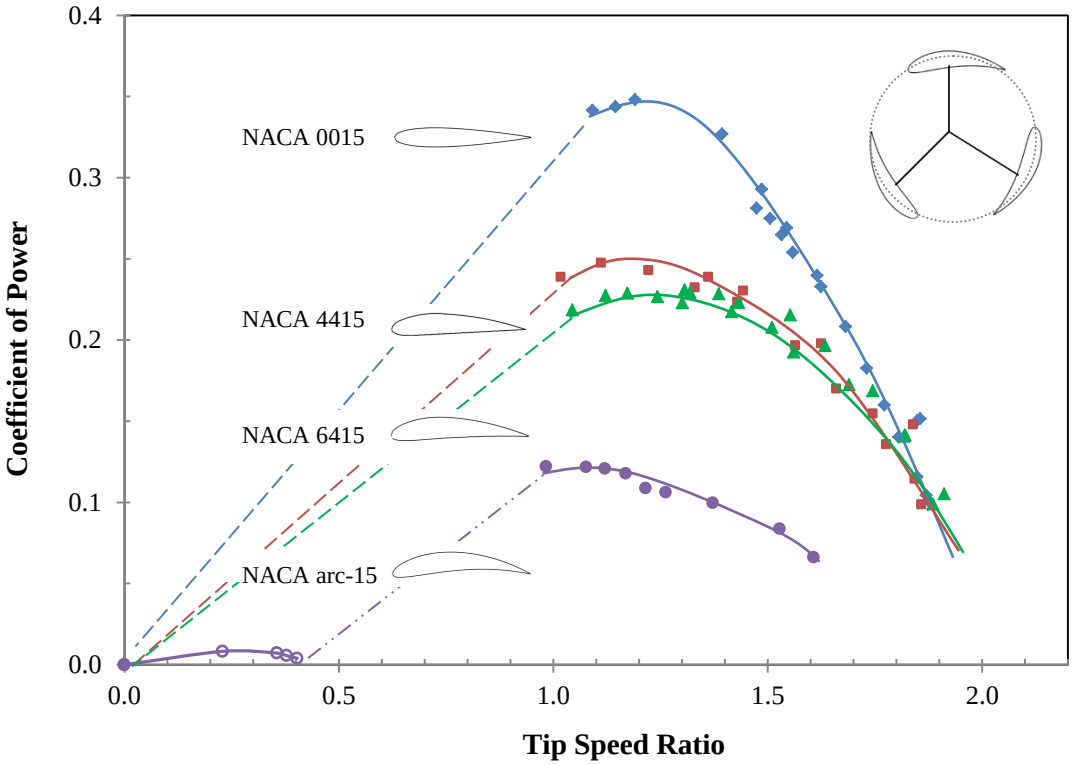

(b)

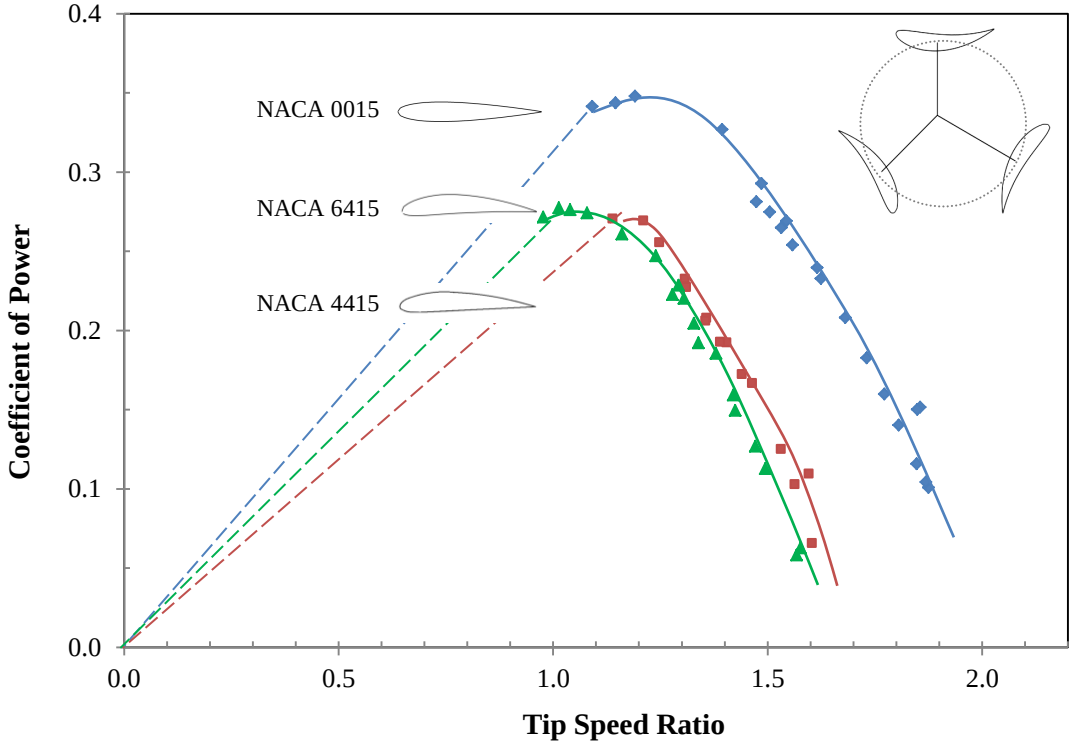

Figure 3.10. **(a)** Cambered airfoils with a concave-in configuration have lower C_P than symmetric airfoils. **(b)** Concave-out blades also have lower C_P. Parameters: medium blades, c = 6 cm, U = 8 m/s.

3.4 Thickness Study

The effect of blade thickness on power generation was also investigated. The tested blades all had the same chordlength of 6 cm (medium blade size) but had varying thicknesses of 9%, 15% (baseline), and 21% of the chordlength. Figure 3.11 compares the C_p for these blades. The plot clearly indicates that the thin NACA 0009 blades perform worse than the other two blades, generating about half the power, despite being able to spin the fastest when unloaded. The thick NACA 0021 blades generate comparable power to the medium blades. However, for windspeeds below 7 m/s, the thick blades did not reach their maximum operating speed without a forced start, while the other blades did not need a forced start for any windspeeds.

The results indicate that decreasing the blade thickness from the baseline value of 15% has detrimental effects on power generation. Also, increasing the thickness makes no significant change in power performance.

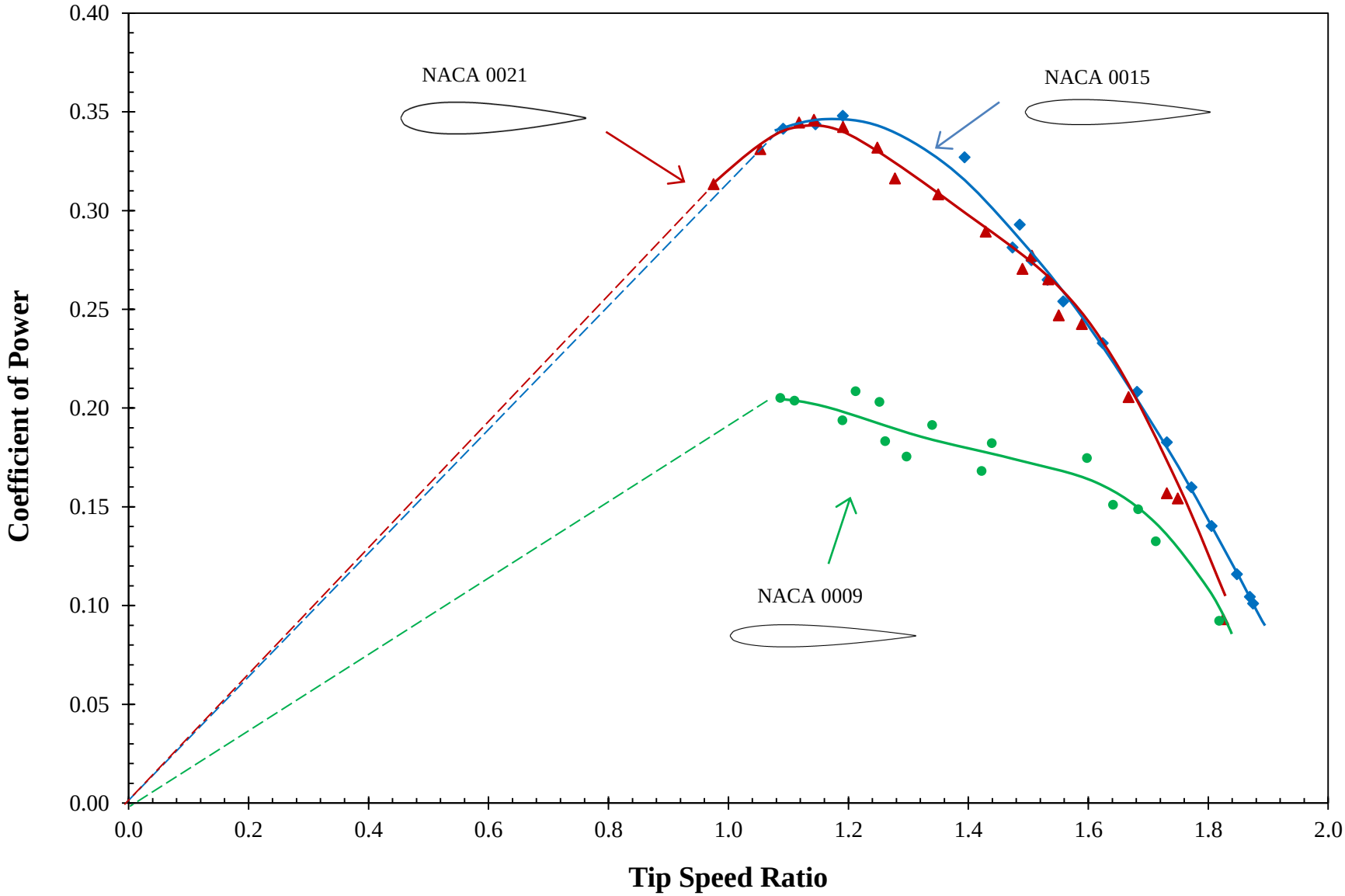

Figure 3.11. Coefficient of Power vs Tip Speed Ratio Comparison for medium blades of various thicknesses at a windspeed of 8 m/s.

4. Zigzag blades

A few variations of zigzag blade designs were tested in the same methods that the straight blades were. The turbine was loaded and the coefficient of power (C_P) and tip speed ratio (TSR) was determined. Figure 4.1 shows that adding a zigzag with a 30 degree sweepback angle to a NACA 0015 airfoil blade decreases C_P. The curves have similar shapes, and the peak C_P occurs at the same TSR, but the zigzag blade has a somewhat lower C_P curve.

The airfoil profile of the zigzag blade was changed to try to improve power performance. The symmetric NACA 0015 was replaced with the custom NACA arc-15 profile which has the same thickness distribution as the 0015 but a chordline that is cambered along the turbine circumference. Figure 4.2 shows that the two profile types have comparable C_P when the cambered profile is force started, although the operating regime of the TSR is shifted slightly higher for the cambered blade. This is another example whereby a mini-turbine may spin faster in the unloaded condition, but has no increase in power output.

Figure 4.3 shows more experiments with the cambered profile. When compared to a straight cambered blade, the 30 degree zigzag performs better. The straight cambered blade has a wider operating range of TSR, but can only achieve this performance with a forced start even at a windspeed of 8 m/s. Figure 4.3b shows that a 45 degree zigzag blade also performs poorer than the 30 degree zigzag. The higher sweep angle also shortens the TSR operating range.

Of all the zigzag blades tested, the symmetric NACA 0015 profile with a sweepback angle of 30 degrees performed the best, but did not perform better than the baseline straight, symmetric medium blades.

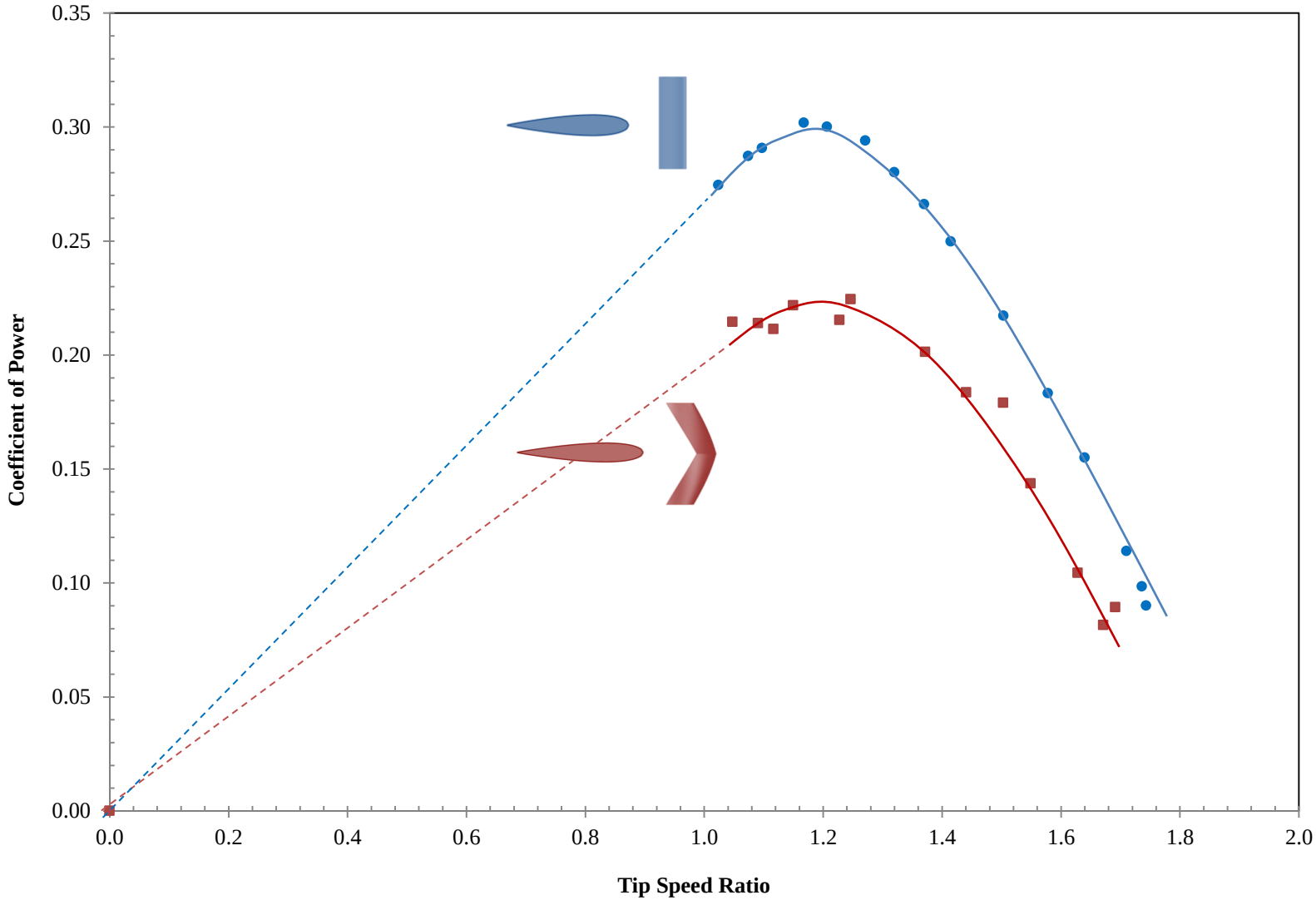

Figure 4.1. Cp vs TSR. Sweeping a straight symmetric blade decreases power output. Parameters: NACA 0015, chordlength 6 cm, pitch (straight) 0 deg and pitch (zigzag) -2.7 deg. Sweepback angle of zigzag blade: 30 deg. Windspeed: 8 m/s

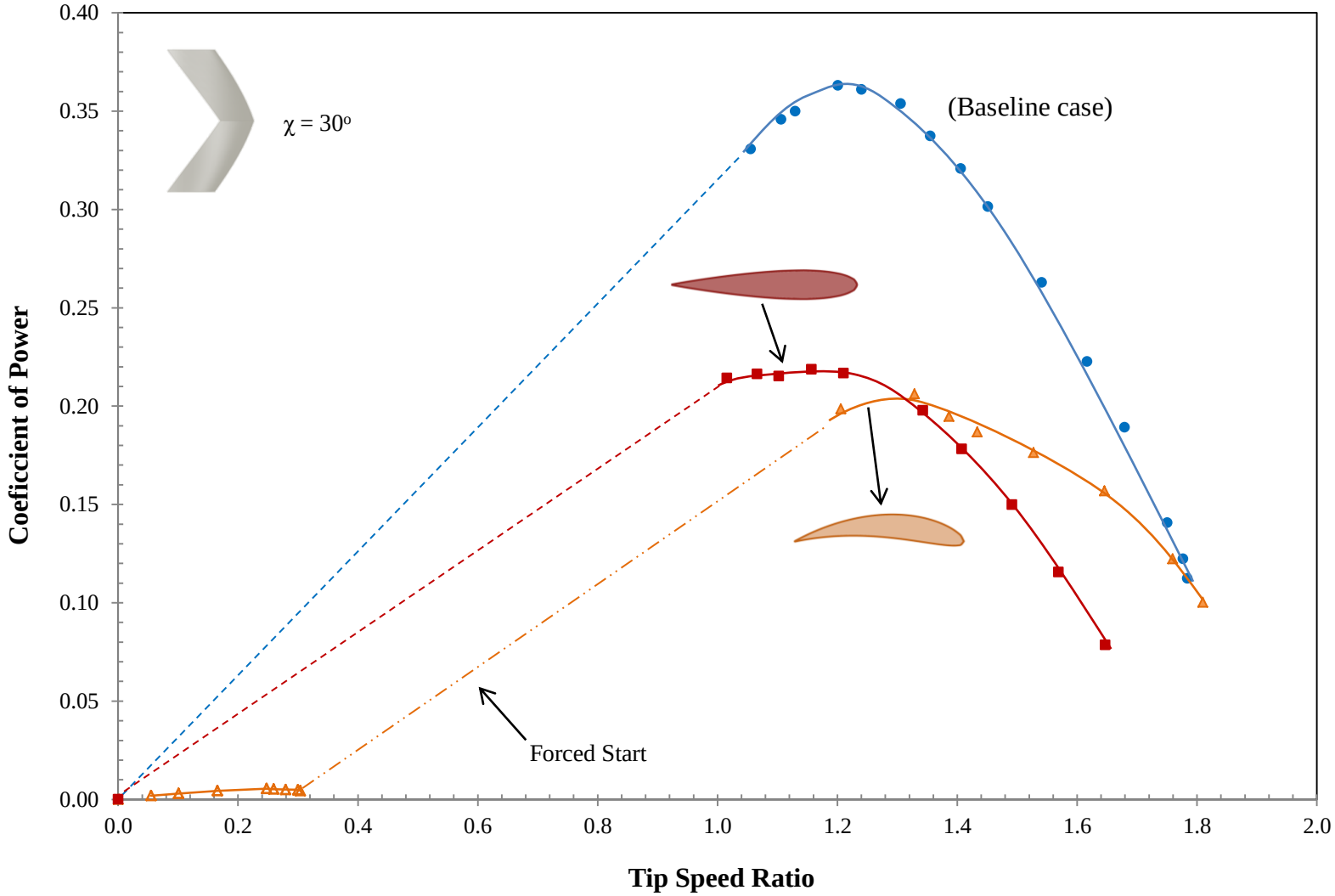

Figure 4.2. Cp vs TSR – At the same sweep angle, a cambered profile must be forced started to reach comparable power as a symmetric blade. Both designs have lower C_P than the baseline case of straight symmetric medium blades. Parameters: NACA 0015 (pitch 1.8°) and NACA arc-15 (pitch 1.6°), chordlength 6 cm, sweep angle 30°, and windspeed 6 m/s.

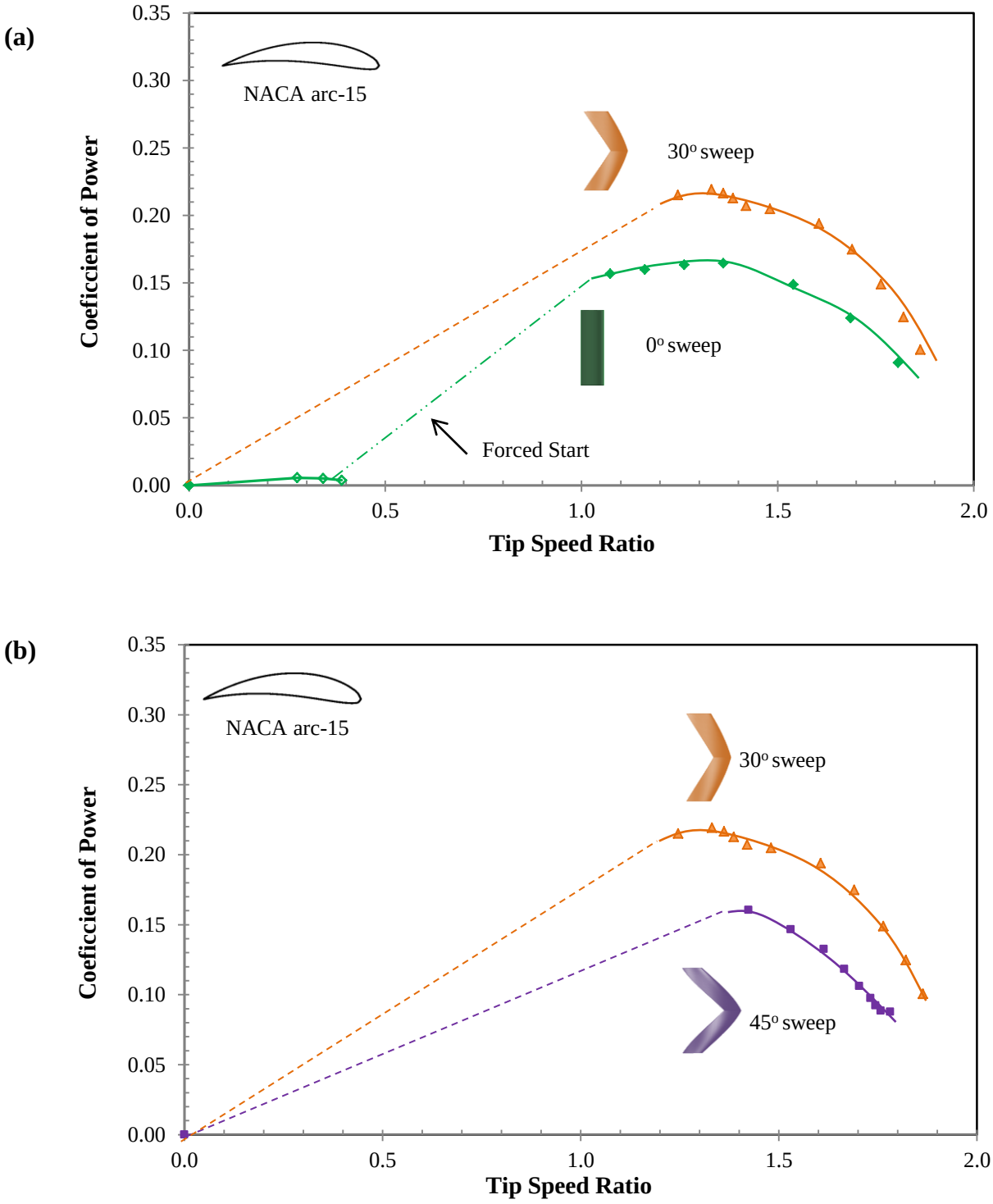

Figure 4.3. Cp vs TSR. **(a)** Sweeping a cambered blade improves power output. Even at 8 m/s, the straight cambered blade needs a forced start to perform well. **(b)** High Sweep angle performs poorly. Parameters: Windspeed 8 m/s, chordlength 6 cm, NACA arc-15. 40 deg zigzag has pitch: 0 deg, 30 deg zigzag has pitch 1.6 deg, and straight blade has pitch 1.9 deg.

5. Helical Blades

Of the three zigzag blades tested, the blade with a symmetric NACA 0015 profile and a sweepback angle of 30 degrees performed the best. Hence, the helical blades for this study were designed with the same sweepback angle and underwent the same C_P test. The chordlength was maintained at 6 cm to continue comparisons with the baseline straight symmetric medium blades.

Figure 5.1 compares the results of a C_P test for the straight medium blades, the 30 degree zigzag blades, and the helical blades at a windspeed of 6 m/s. The helical blades had the lowest C_P and the smallest TSR operating range. This result corresponds with the Oxford group (McAdam et al 2013c) who show that straight bladed turbines perform better than truss turbines. However, these results are counter to those of Gorlov (1998), whose experiments showed that helical turbines performing better than straight-bladed turbines.

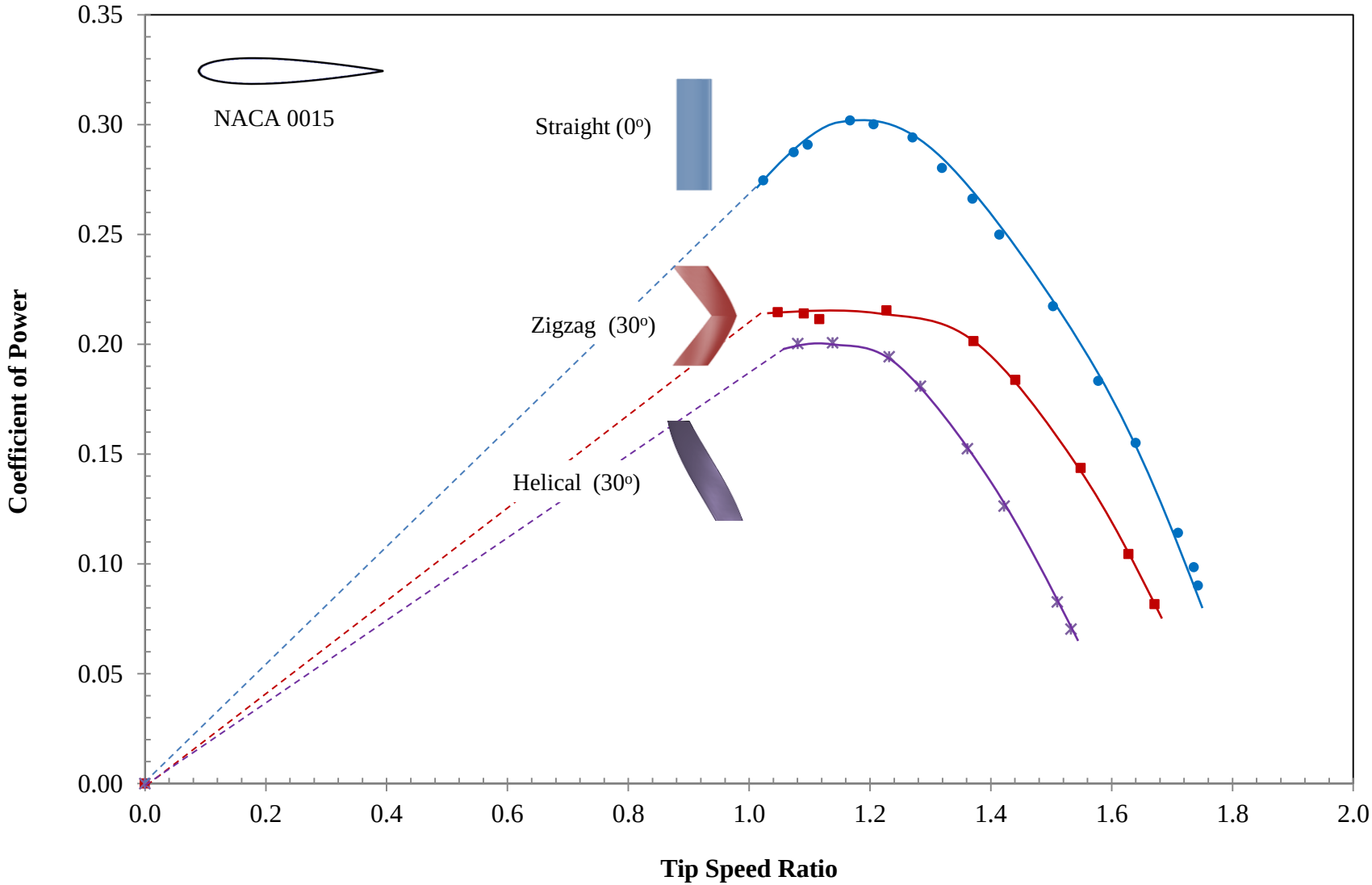

Figure 5.1. Cp vs TSR. Helical blades with the same sweepback angle as a zigzag blade do not perform as well. Parameters: NACA 0015, chordlength 6cm, windspeed 6 m/s, sweepback angle 30 deg.

6. Self-Start Study

An array of urban mini-turbines would not only have to produce high power, but also self-start unaided. The experimental method for conducting a self-start study is described in Section 2. The results for six blade types are shown in Figures 6.1 and 6.2. Note that any self-start study will depend on the intrinsic friction of the system the turbine must overcome. Thus, these results should not be taken as absolute, but rather in the comparative sense.

In Figure 6.1, all the blades have a profile of a symmetric NACA 0015 airfoil. The straight blade has the lowest tendency to self-start for the range of windspeeds tested. The 30 degree zigzag blades have a higher tendency to self-start, and the helical blades have the highest tendency. Note that this trend is reverse of the C_P trend discussed earlier.

In Figure 6.2, all the blades have a cambered profile. Increasing the sweepback angle from 30 degrees to 45 degrees also increases the self-starting capability. This makes sense because there are more sections of the zigzag blade that are available to intercept the wind. The straight cambered blade has a slightly higher self-starting capability than the 30 degree zigzag, which is surprising since they had such poor power performance. However, compared to the symmetric straight blade, the cambered straight blade has much better self-starting capability.

The self-start study shows that the baseline straight, symmetric, NACA 0015 medium blades is the most difficult to self-start. Altering the airfoil profile or sweepback angle increases the self-starting capability, though at the cost of power output. Further custom-designed airfoils or sweepback angles may be able to increase the power output of zigzag blades to match that of the medium blades while maintaining high self-starting capabilities.

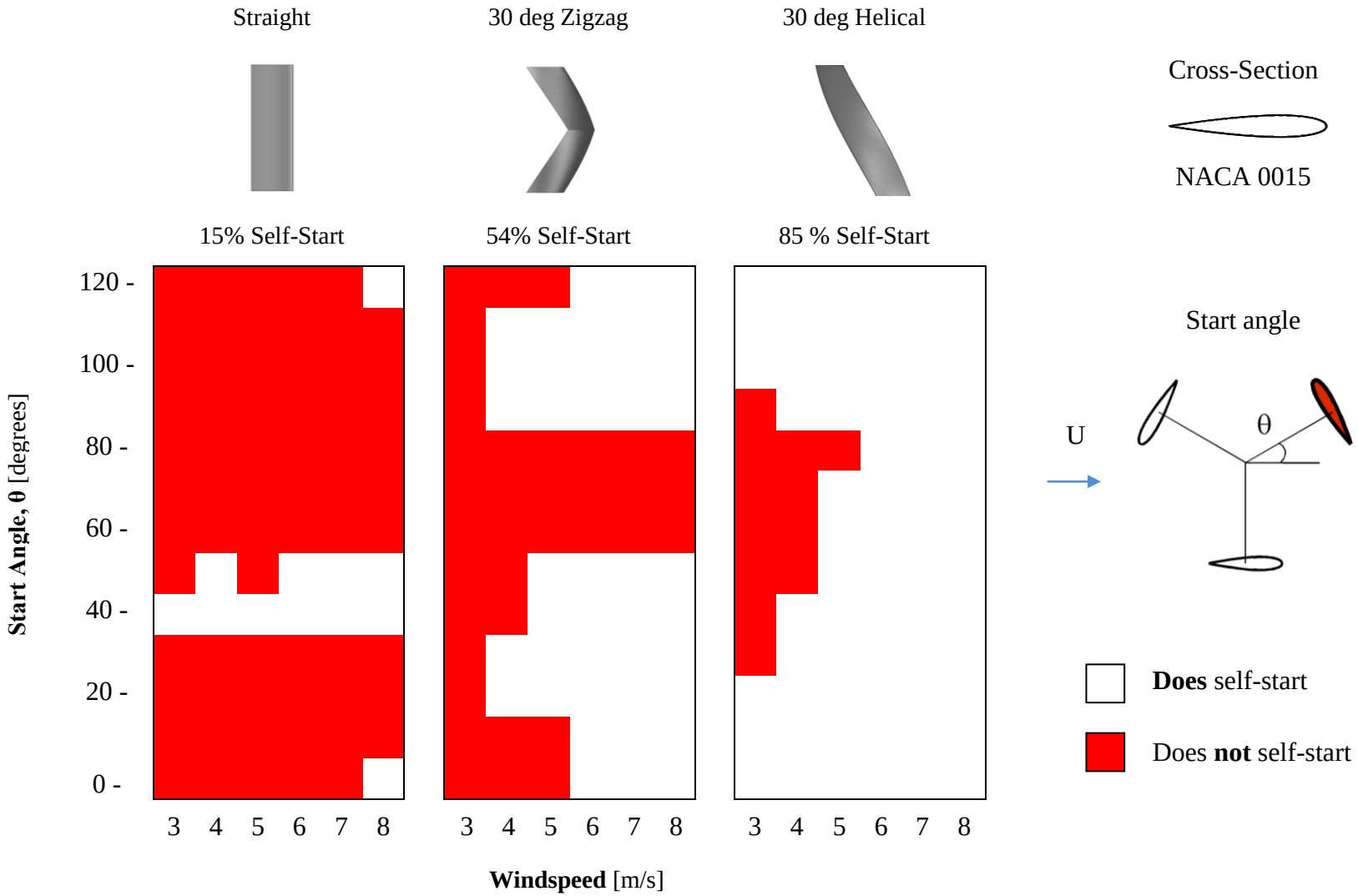

Figure 6.1. Self-Start study on symmetric (NACA 0015) cross-sections. Adding a sweepback angle increases self-starting capability.

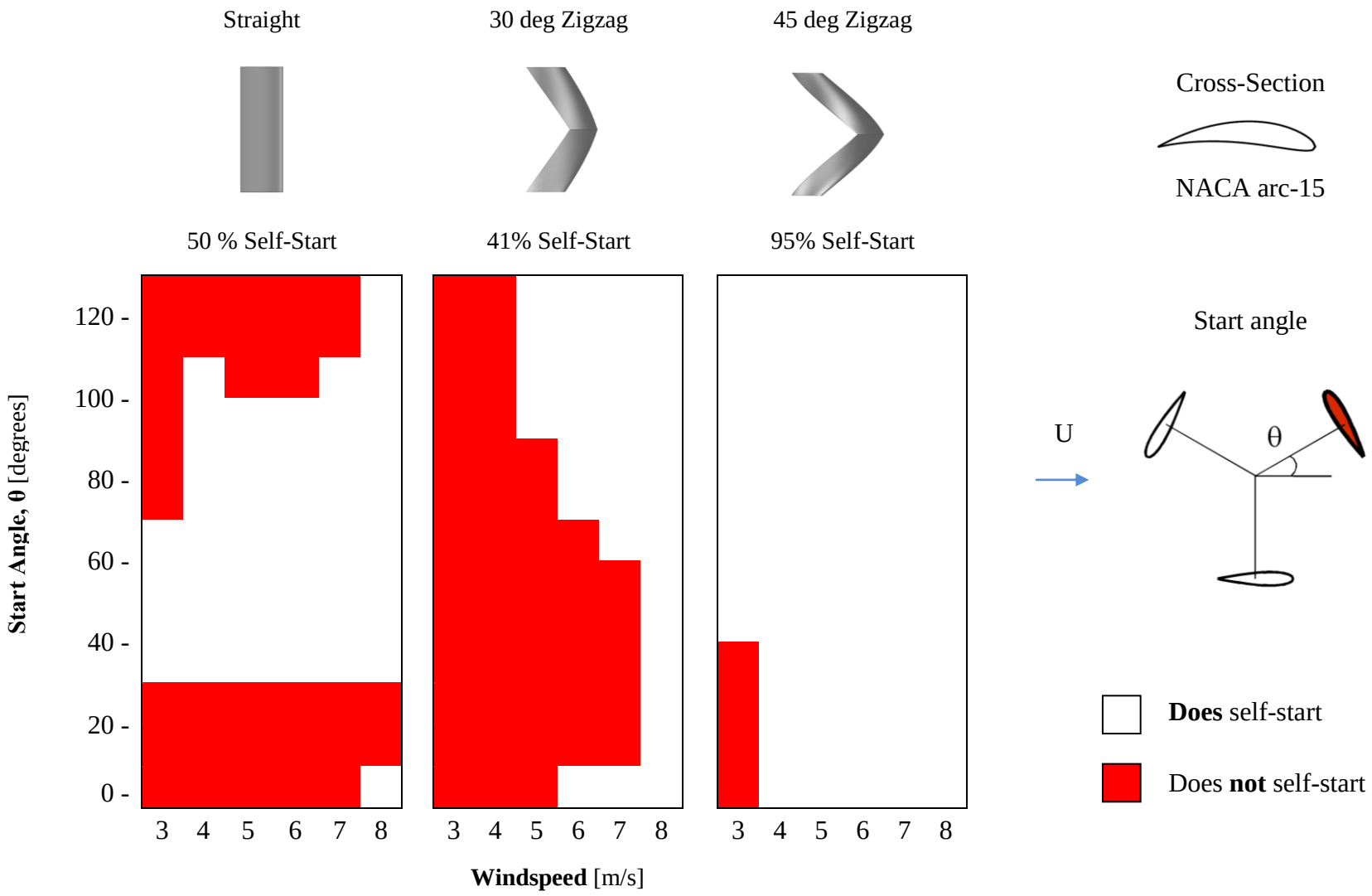

Figure 6.2. Self-Start study on cambered (NACA arc-15) cross-sections. Increasing the sweepback angle from 30 degrees to 45 degrees increases self-starting capability.

7. Unconventional Blade Designs

Other turbine blade designs incorporated ideas from high lift devices, such as delta wings, slots, and tubercles from whale flippers. These unconventional blade designs were chosen because they alter the coefficient of lift and stall characteristics of the airfoil. Figure 7.1 shows the results of a C_P test done for each of the unique blades compared to the baseline NACA 0015 medium blades.

None of the new designs tested performed as well as the medium blades. The slotted blade performed the best out of the new designs, but only when the slot was pointed outwards. When the slot was pointed inwards, the turbine performed significantly worse. The whale inspired blade performed comparably to the blade with the slot pointed inwards. However the blade that performed the poorest, even when given a forced start, was the one with delta wings.

The photos shown in Figure 7.2 are of the delta wing blade in the smoke wire flow visualization wind tunnel. Small spanwise vortices can be seen coming off the apex of each delta. However, we believe they may not be strong enough to provide enough thrust for the mini-turbine. Furthermore, the vortices break up quickly at the troughs in between each delta wing segment. This possibly further reduces the lift and increases the drag of the blades.

In summary, none of the unconventional blade designs improved power output as compared to straight medium blades. This implies that blade designs should not only increase lift

but also decrease drag. In addition, the flow field and dynamics of the mini-turbines are different than those of aircraft or whale flippers, and care should be taken when designing new turbine blades.

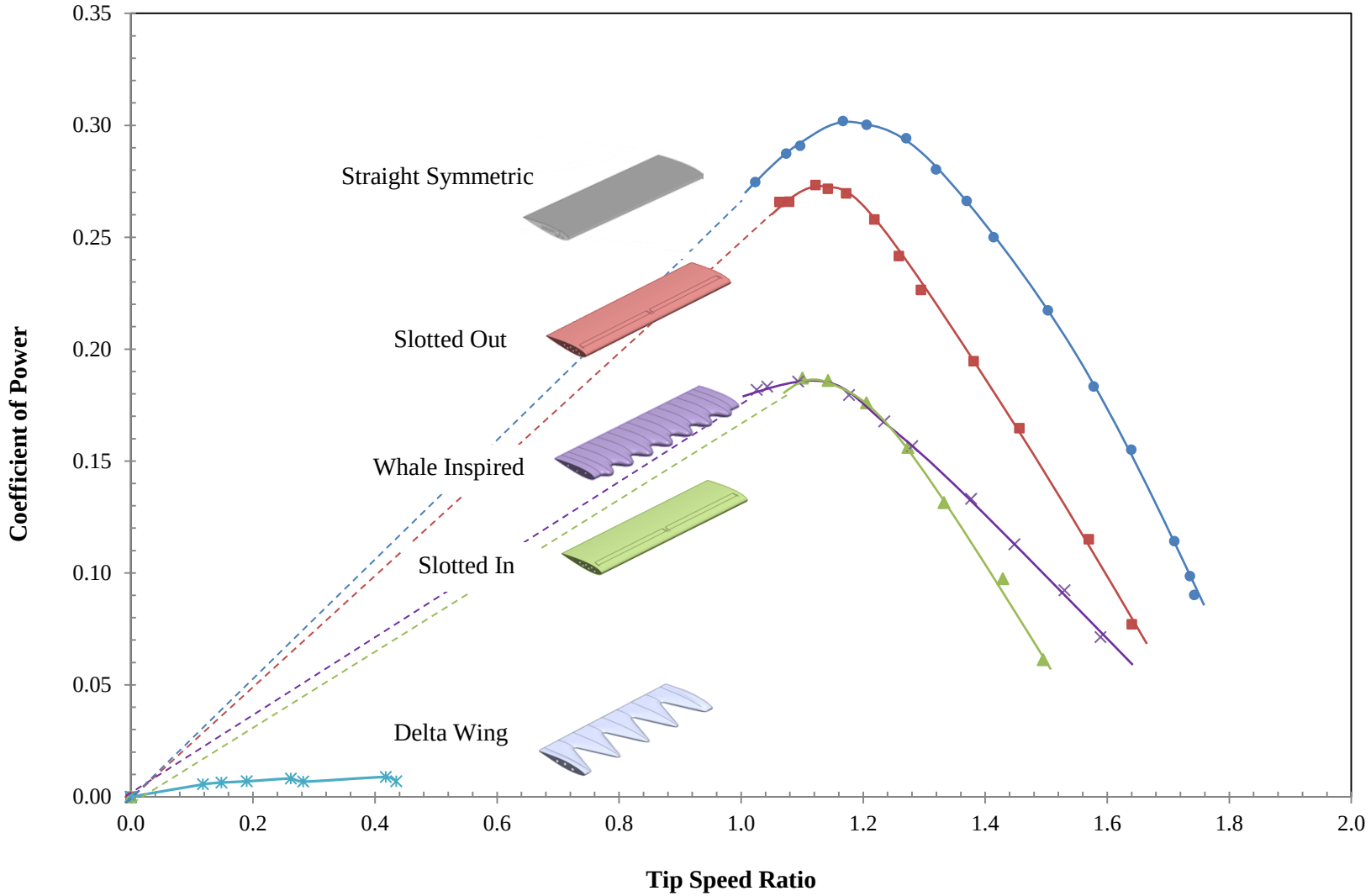

Figure 7.1. Cp vs TSR at a windspeed of 6 m/s. High lift devices do not generate more power than the baseline NACA 0015 blade.

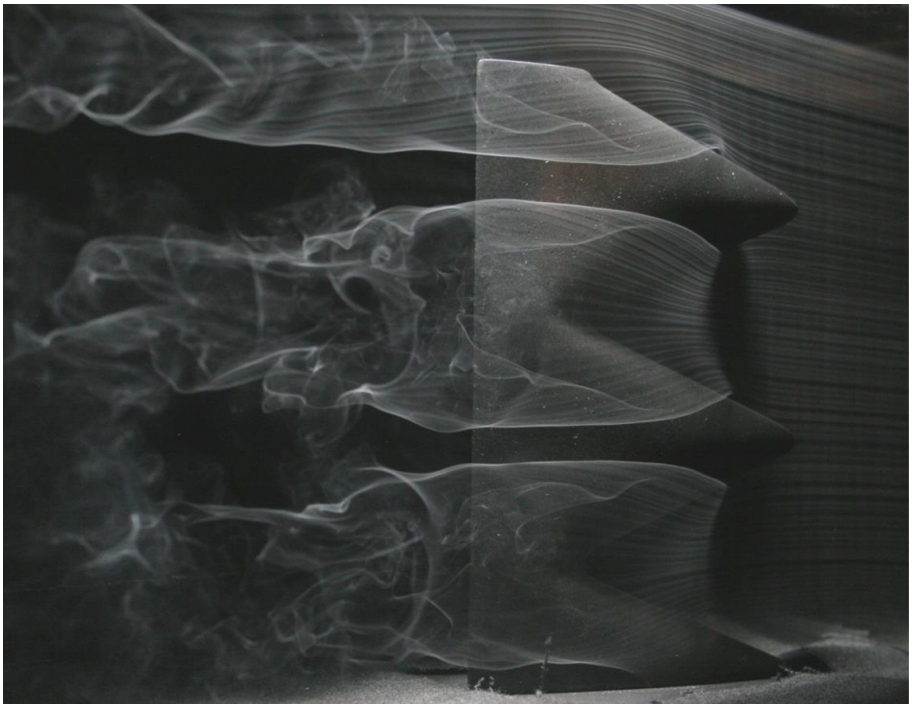

(a)

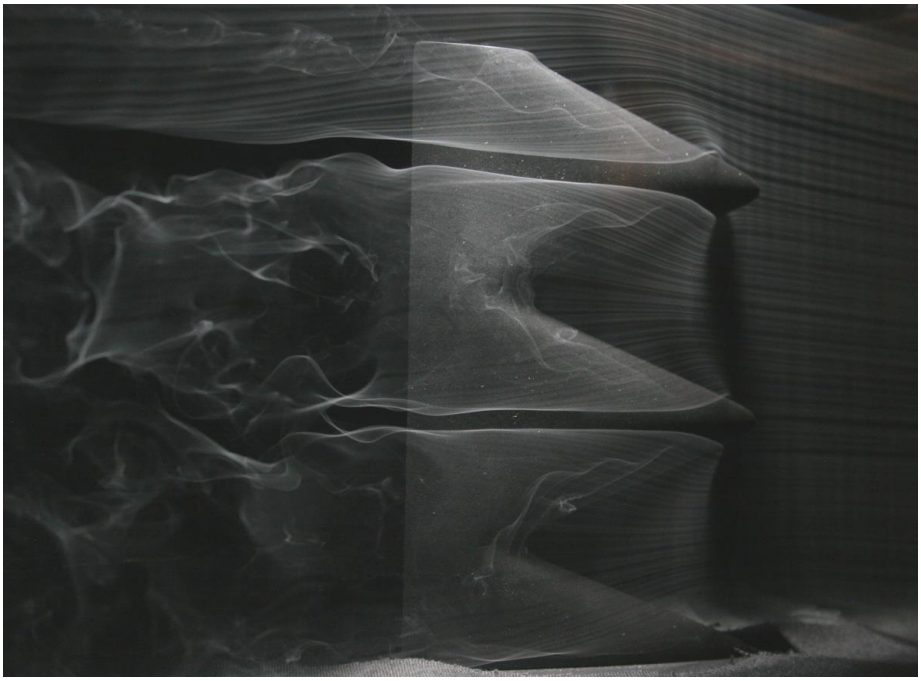

(b)

Figure 7.2. Smoke Flow Visualization of the delta wing blade at **(a) 12 deg angle of attack** and **(b) 20 deg angle of attack**. Streamwise vortices are faint and breakup when they approach a "trough" from an adjacent delta wing segment.

8. Guiding Principles

8.1 Angle of Attack

Numerical modeling is used here to explore the physics of mini-turbines in a simple manner to guide possible turbine designs. The angle of attack α of the blades is the most fundamental parameter, since force, torque, and power are dependent on the angle of attack. Figure 8.1 below illustrates the geometry of an airfoil blade at an arbitrary azimuth position θ. The freestream velocity is *U*, the tangential velocity is $R\dot{\theta}$, the radius of the turbine is *R*, and the vector addition of the velocities is V_{Total}.

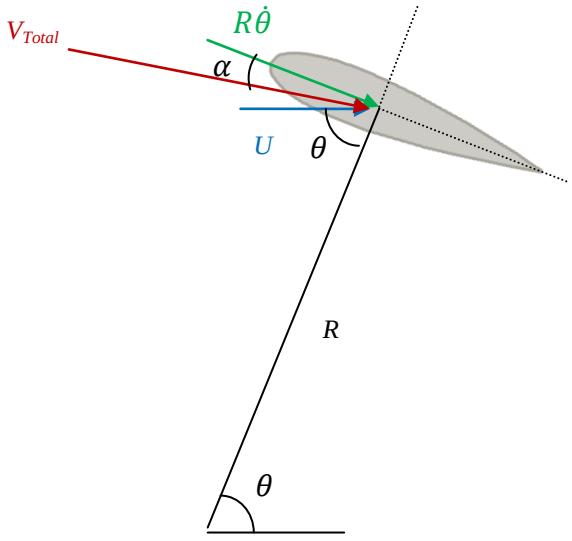

Figure 8.1: Kinematic diagram of an airfoil blade

From simple geometry and the definition of tip speed ratio (TSR = $R\dot{\theta}/U$) an equation of the angle of attack can be derived as Equation 8.1:

$$\tan \alpha = \frac{\sin \theta + TSR}{\cos \theta} \tag{8.1}$$

Hence, the angles of attack of an airfoil blade can be calculated as a function of theta for a range of TSR, as shown in Figure 8.2 on the next page. The rotational aspect of mini-turbines affects the range of angle of attacks a blade sees during one revolution. As TSR approaches infinity, the angles of attack approach zero. This is because the incident angle of the rotational velocity is always in the tangential direction, or at $\alpha = 0°$, and the freestream velocity is negligible by comparison. At TSR = 1, the curve is linear but discontinuous at $\theta = 270$. This discontinuity is a special circumstance due to the rotational velocity being equal to the freestream velocity. At TSR < 1 the angle of attack ranges from -180 to 180 degrees, and as TSR approaches zero, the relationship is linear again.

Figure 8.3 shows the range of angles of attack of a blade as a function of TSR. As previously explained, high TSRs encounter few angles of attack, while TSR $\leq$ 1 encounter all 360 degrees of angle of attack. The typical operating range of a mini-turbine is marked by the dashed lines. The mini-turbine undergoes large angles of attack, ranging from $\pm$ 45 for TSR=2 and $\pm$ 180 for TSR = 1. This large range of angles of attack must be taken into account in blade design considerations.

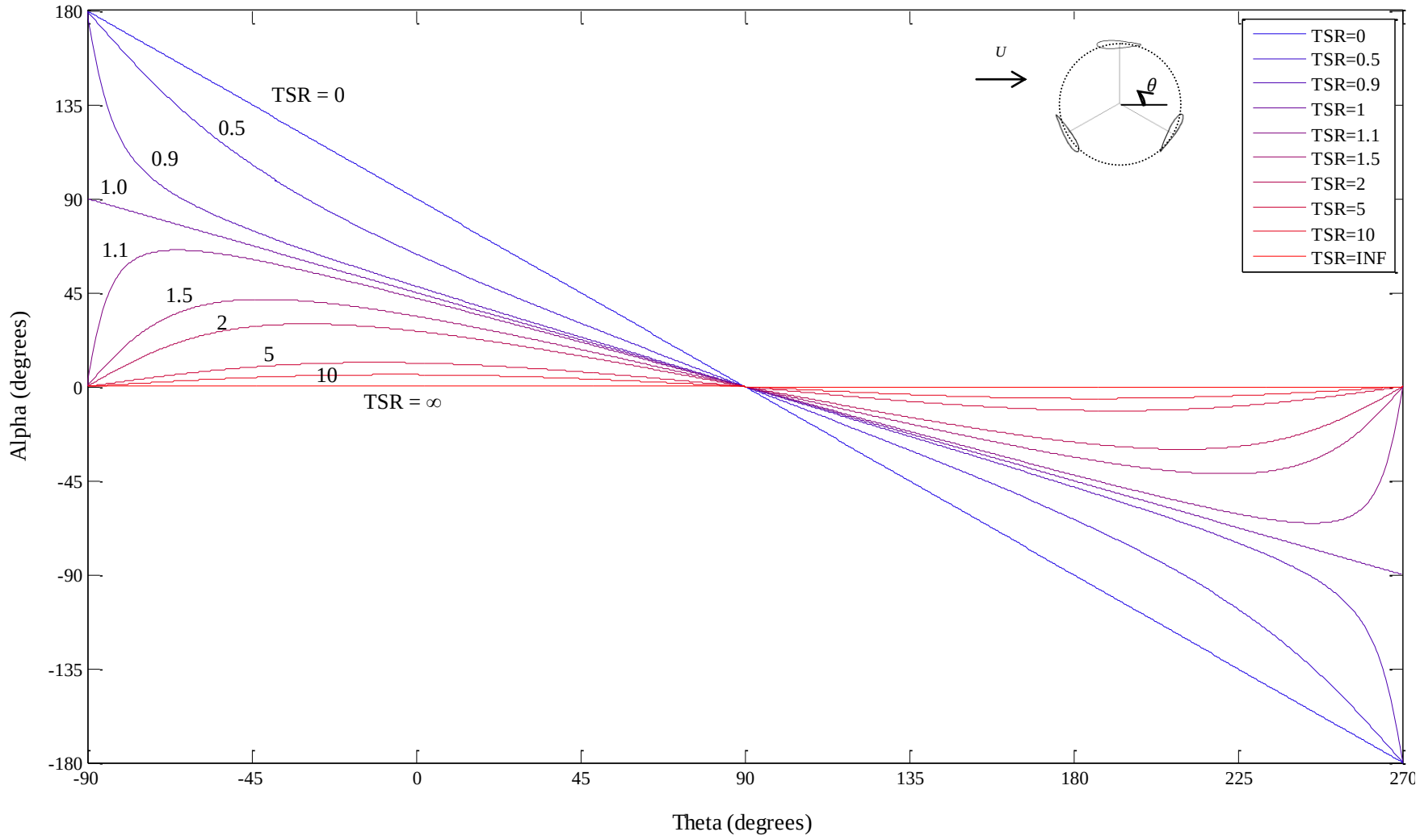

Figure 8.2. Angle of Attack vs Tip Speed Ratio. As TSR approaches infinity, the angle of attack on the turbine blades goes to zero. At TSR=1, the curve is linear but discontinuous at θ=270. At TSR < 1 the angle of attack ranges from -180 to 180 degrees.

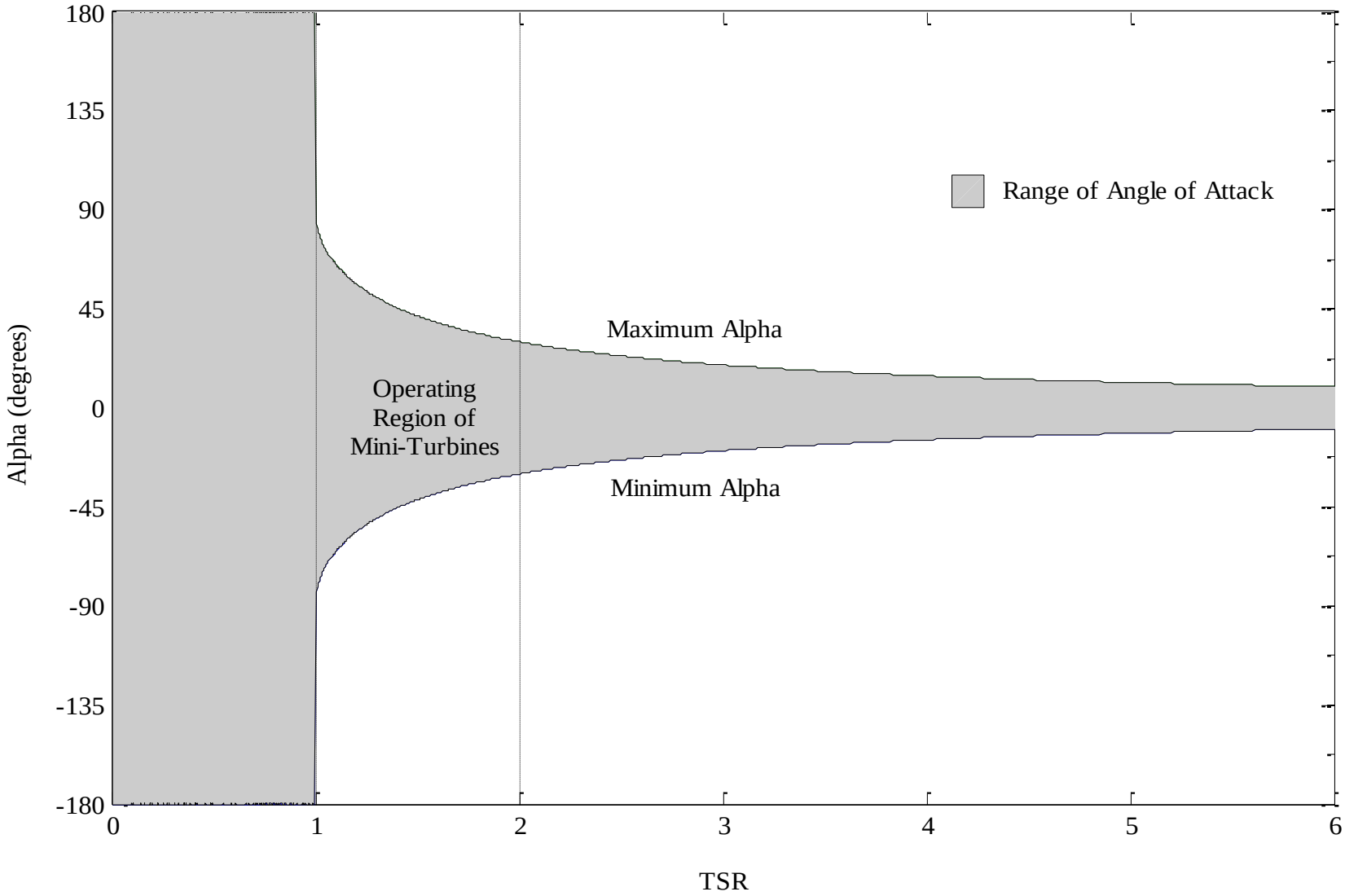

Figure 8.3. Angle of Attack vs Tip Speed Ratio. As TSR approaches infinity, the angle of attack on the turbine blades approaches zero. At TSR < 1 the angle of attack ranges from -180 to 180 degrees.

8.2 Blade Wake Interference

As a turbine blade rotates it sheds a wake that is carried downstream and alters the flow field. Understanding the interaction and interference of these blade wakes will help determine the best parameters for turbine design. This section will briefly describe a simple analysis for estimating when blade wake interaction might occur as a blade rotates. Full details can be found in Appendix B.

The wake interference analysis was done numerically in Matlab. The wake of the blade is represented as a series of points convecting downstream at the same speed as the freestream wind velocity. For turbines with large c/D ratios, wake interference is high and blades are crossing into wakes as much as 2/3 of the time. Figure 8.4 shows six snapshots of a revolution of a 3-bladed mini-turbine. By following the blue blade, it can be seen that on the upstream side of the turbine it does not encounter wake interference. However, on the downstream side the blue blade encounters four distinct regions of wake interference, including one created by its own wake.

Figure 8.5 shows a comparison of two simulations superimposed on each other. The image with ♦, o, and + symbols for wakes was done by the author with the simple wake model described above, while the vorticity image was done by Dr. Dietmar Rempfer of Illinois Institute of Technology (Rempfer 2012). Rempfer's simulation is a 2D direct numerical simulation (DNS) done with the commercial code STAR-CCM+ with Re_c = 50,000 and TSR = 2. The blades produce a clean wake for half of the rotation, but at high angles of attack they create large vortices which interact and merge into larger vortex structures. The turbine geometry was deduced to be a chordlength of 0.0784m and a diameter of 1.3m. Using the similar parameters,

the DNS model and the simple wake model are a visual match on the large scale effects. The simple wake model captures the same overall location of the wakes, especially the blue diamonds. This shows that, although the simple wake model neglects vortex merging and interaction, it is a good estimation of the locations of shed wakes and blade wake interference regions.

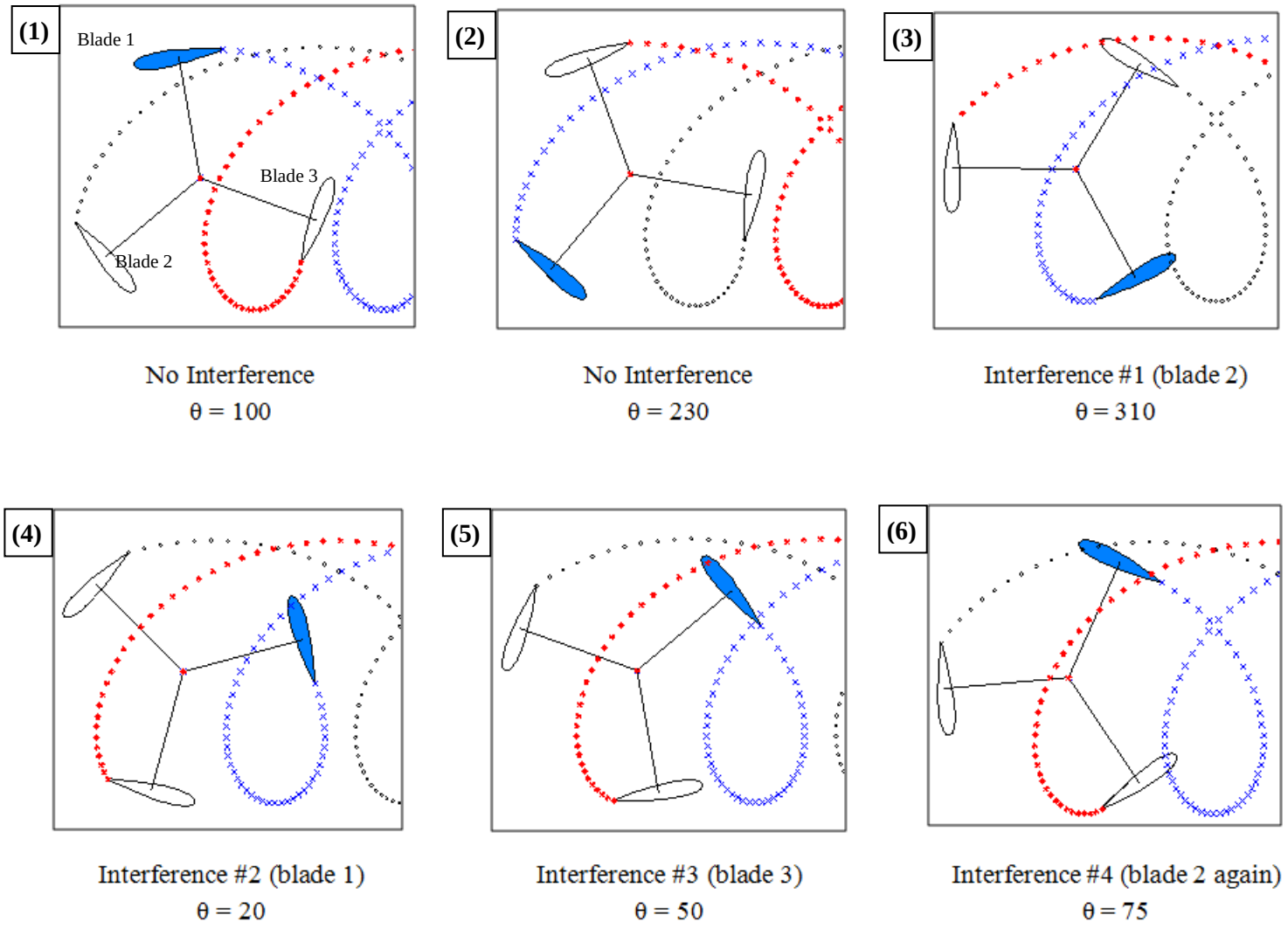

Figure 8.4. **Wake Interference Diagrams** for TSR = 2. The blue airfoil passes through 4 distinct wake interference regions produced from the wakes of other blades as well as its own wake. In (1) and (2) the blue airfoil hits no wakes. In (3) it hits the wake formed from blade 2. In (4) it hits its own wake. (5) The airfoil goes through the wake formed by blade 3 and in (6) it hits the wake formed from blade 2 again.

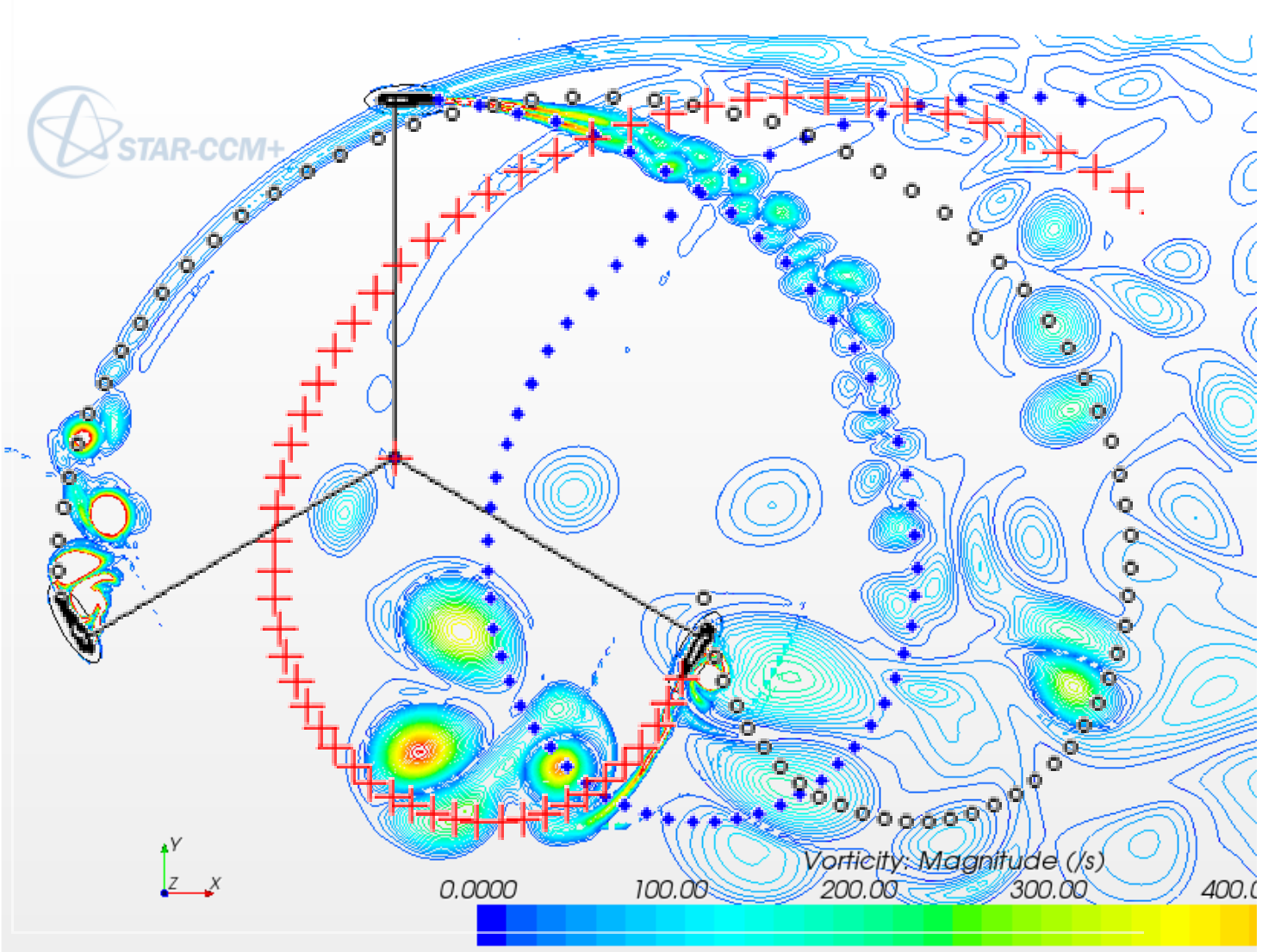

Figure 8.5. Two wake simulations superimposed at a visual match. Parameters: Rempfer: Re_c 50,000 and TSR=2. FDRL: Re_c 80,000 and TSR=3.5.

The next step is to quantitatively mark the wake interference regions. Figure 8.6 shows polar diagrams at four different TSRs with shaded regions estimating where interference occurs. The θ-axis of the polar plots is the same as the azimuth position angle of one blade. Figure 8.6c shows a polar plot of one blade at TSR = 2, with shaded regions of wake interference that are in general the same as the four interferences that were seen in Figure 8.4, which is also at TSR = 2.

The polar plots in Figure 8.6 also contain values of coefficient of power as a function of θ, $C_P(\theta)$. $C_P(\theta)$ is directly proportional to torque $T(\theta)$ as follows:

$$C_P(\theta) = \frac{T(\theta)\cdot\dot{\theta}}{P_{wind}} \tag{8.2}$$

where $\dot{\theta}$ is the angular velocity of the turbine and P_{wind} is the available power in the wind. The polar plots have two primary positive peaks located at the "top" of the blade trajectory, when the blade is moving into the freestream velocity. Peak $C_P(\theta)$ values occur when the angle of attack of the blade is less than the static stall angle of 12 degrees, when there is high lift and low drag. Wake interference regions in grey show that downstream positive $C_P(\theta)$ may be reduced by blade wake interference.

For simplicity, throughout this thesis, C_P is taken as the average C_P defined in Equation 8.3 below.

$$C_P = \overline{C_P} = \frac{1}{2\pi}\int_0^{2\pi} C_P(\theta)\, d\theta \tag{8.3}$$

Furthermore, the area within a $C_P(\theta)$ vs θ curve is proportional to the total average C_P by Equation 8.4:

$$C_P = \frac{1}{2\pi}\int_0^{2\pi} C_P(\theta)\, d\theta = \frac{1}{2\pi}(Area\ Under\ Curve) \tag{8.4}$$

Thus,

$$C_P \propto Area\ Under\ Curve \tag{8.5}$$

The power polar plots in Figure 8.6 of varying TSR can then be evaluated by comparing the areas under the curves. Increasing TSR increases power performance while wake interference remains comparable; it is excpected that power will be reduced due to downstream wake interference for all TSRs.

This simple wake interference study has given additional insights into the possible flow dynamics of mini-turbines that can be used to better design mini-turbines or better predict the performance of mini-turbines.

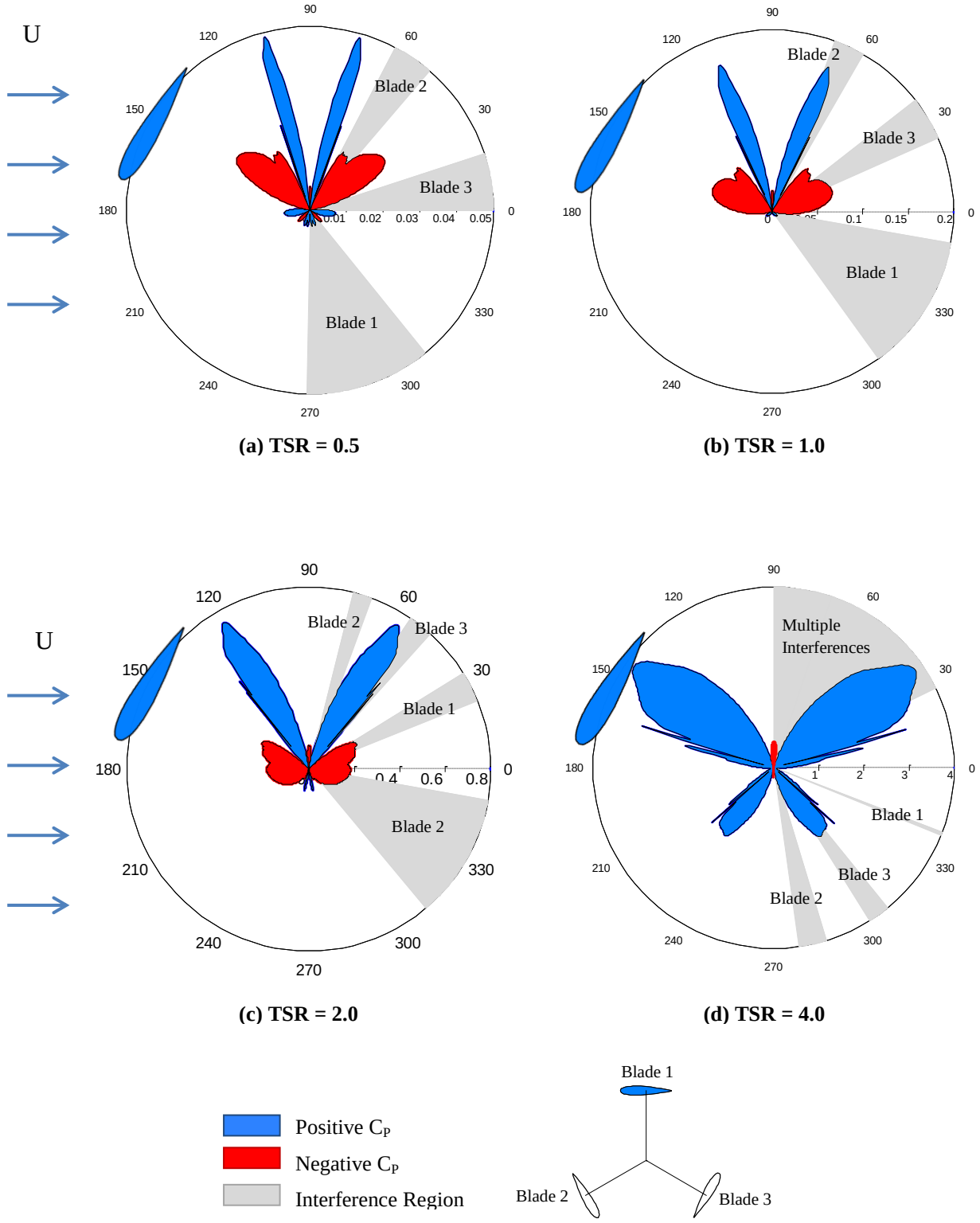

Figure 8.6. **Power Polar Plot:** Cp vs θ values for one blade, at a range of TSR. Area within the curve is proportional to the total average C_p of the turbine. Wake interference regions in grey show that downstream positive C_p may be reduced by blade interference. Increasing TSR increases performance while wake interference remains comparable. NACA 0018, Re 80,000, chord 6 cm, radius 8.2 cm.

9. Conclusions

Several designs of mini-turbine blades have been experimentally tested to find the design with the highest power output. Mini-turbines are capable of producing power, but are sensitive to parameters such as offset pitch angle, c/D (chordlength to turbine diameter ratio), camber, and sweepback angle. The optimal offset pitch angle for straight symmetric blades is 0 degrees. Mini-turbines with large c/D ratios (c/D = 0.36 and c/D 0.48) produce the most power. This is contrary to classical c/D ratios that are seen in large scale commercial turbines such as Windspire. Furthermore, these low Reynolds number mini-turbines have an operating range at lower TSR than high Reynolds number turbines.

Deviating in camber or thickness from the classical NACA 0015 tends to decrease C_P. Adding a sweepback angle assists in self-starting capabilities, but is also detrimental to C_P. The zigzag blade has a higher C_P than a helical blade with the same sweepback angle, but at present produce a somewhat lower C_P than the straight blade.

More unconventional blade designs that have components inspired by high lift devices from aircraft or whale flippers also decrease C_P. The mini-turbines are sensitive to the varying parameters of this study, but an improved, specially designed blade for mini-turbines is yet to be found. The numerical analysis assists in understanding the physics of the flow and how blade wakes interact. The knowledge gained from this thesis lays a foundation for future mini-turbine designs.

References

ARMSTRONG, S., FIEDLER, A., & TULLIS, S. 2012. Flow separation on a high Reynolds number, high solidity vertical axis wind turbine with straight and canted blades and canted blades with fences. *Renewable Energy* **41** 13.

BETZ, A. 1966. *Introduction to the theory of flow machines*. Oxford; New York, Pergamon Press.

BRAVO, R., TULLIIS, S., & ZIADA, S. 2007 Performance testing of a small vertical-axis wind turbine. *21st Canadian Congress of Applied Mechanics*.

BRYANT, M. & GARCIA, E. 2011 Modeling and Testing of a Novel Aeroelastic Flutter Energy Harvester. *J. Vib Acoust.* **133,** 011010

DABIRI, J.O. 2011 Potential order-of-magnitude enhancement of wind farm power density via coutner-rotating vertical-axis wind turbine arrays. *J. Renewable and Sustainable Energy*. **3** 043104.

DEPARTMENT OF ENERGY (DOE). 2008. 20% wind energy by 2030: Increasing wind energy's contribution to U.S. electricity supply. DOE/GO-102008-2587. July 2008.

ERIKSSON, S., BERNHOFF, H., & LEIJON, M. 2008 Evaluation of different turbine concepts for wind power. *Renewable and Sustainable Energy Reviews* **12** 1419.

FIEDLER, A., KOOIMAN, S., MCLAREN, K., ALY, K., TULLIS, S., & ZIADA, S. 2007 Boundary layer flow investigations on small scale vertical axis wind turbines. *23rd Ann. Conf. of the Canadian Wind Energy Association* Quebec (poster).

FIEDLER, A.J. & TULLIS, S. 2009 Blade offset and pitch effects on a high solidity vertical axis wind turbine. *Wind Enginering* **33** (3) 237.

FRAYNE,S. 2010 Humdinger Wind Energy, LLC. http://www.humdingerwind.com/

GIPE, P. 2013 FloWind: the world's most successful VAWT. Excerpt from *Wind Energy Basics Revised: A Guide to Home- and Community-scale Wind Energy Systems.* wind-works.org

GORLOV, A. 1998 Development of the helical reaction hydraulic turbine. *DOE Technical Report*.

HAU, E. 2006 *Wind Turbines: Fundamentals, Technologies, Application, Economics*. Springer, Germany.

HILL, N., DOMINY, R., INGRAM, G., & DOMINY, J. 2009 Darrieus turbines: the physics of self-starting. *J. Power and Energy* **223**

HUSKEY, A., BOWEN, A., & JADER, D. 2009 Wind turbine generator system power performance test report for Mariah Windspire 1kW wind turbine. *NREL*.

ISLAM, M., TING, D.S.K, & FARTAJ, A. 2007. Desirable airfoil features for smaller-capacity straight-bladed VAWT. *Wind Engineering* **31** (3) 165.

KIRKE, B.K. & LAZAUSKAS, L. 2011 Limitations of fixed-pitch Darrieus hydrokinetic turbines. *Renewable Energy* **36** 893.

KJELLIN, J., BULOW, F., ERIKSSON, S., DEGLAIRE, P., LEIJON, M., & BERNHOFF, H. 2011 Power coefficient measurement on a 12 kW straight bladed VAWT. *Renewable Energy* **36** 3050.

KOOIMAN, S. AND TULLIS, S. 2010 Response of a vertical axis wind turbine to time varying wind conditions found within the urban environment, *Wind Engineering* **34 (**4) 389.

LI, S., YUAN, J. & LIPSON, H. 2011 Ambient wind energy harvesting using cross-flow fluttering. *J. Appl. Phys.* **109,** 026104

MACPHEE, D. & BEYENE, A. 2012 Recent advances in rotor design of vertical axis wind turbines. *Wind Engineering* **36** (6) 647.

MCADAM, R.A., HOULSBY, G.T., & OLDFIELD, M.L.G. 2013 Experimental measurements of the hydrodynamic performance and structural loading of the transverse horizontal axis water turbine: part 1. *Renewable Energy*. **59** 105.

MCADAM, R.A., HOULSBY, G.T., & OLDFIELD, M.L.G. 2013 Experimental measurements of the hydrodynamic performance and structural loading of the transverse horizontal axis water turbine: part 2. *Renewable Energy*. **59** 141.

MCADAM, R.A., HOULSBY, G.T., & OLDFIELD, M.L.G. 2013 Experimental measurements of the hydrodynamic performance and structural loading of the transverse horizontal axis water turbine: part 3. *Renewable Energy*. **59** 82.

MCINTOSH, S.C. & BABINSKY, H. 2013 Aerodynamic modeling of swept-bladed vertical axis wind turbines. *J. Propulsion and Power*. **29** (1) 227.

MIGLIORE, P.G, WOLFE, W.P, & FANUCCI, J.B. 1980 Flow curvature effects on Darrieus turbine blade aerodynamics. *J. Energy*. **4** (2).

MOON, F.C, OH, S.T, BANAI, R., & GOULD, Z. 2009 Vibro-Wind Technology: Alternative Wind Energy System. Cornell University.

PARASCHIVOIU, I. 2002 *Wind Turbine Design: With Emphasis on the Darrieus Concept*. Presses Internationalales Polytechnique, Canada.

REMPFER, D. 2012. Personal email correspondence.

SCHEURICH, F., FLETCHER, T.M. & BROWN, R.E. 2010 The influence of blade curvature and helical blade twist on the performance of a vertical-axis wind turbine. In: 29th *ASME Wind Energy Symposium*, 2010-01-04 - 2010-01-07, Orlando, Florida.

SHELDAH, R.E., KLIMAS, P.C., FELTZ, L.V. 1980 Aerodynamic performance of a 5-meter-diameter darrieus turbine with extruded aluminum NACA-0015 blades. *Sandia National Labs Technical Report*.

SIROHI, J. & MAHADIK, R. 2012 Harvesting wind energy using a galloping piezoelectric beam. *J. Vib Acoust.* **134,** 011009

TEMPLIN, R.J. 1972 Wind tunnel investigation of a 14ft diameter VAWT. *National Aeronautical Establishment Technical Report*. LTR-LA-105

WHITE, F. M. 2008. *Fluid Mechanics*. 6th Ed. McGraw-Hill, Boston.

YAMADA, S., TAMURA, T., & MOCHIZUKI, S. 2011 Effects of wing section on mean characteristics and temporal torque variation for a small straight-bladed vertical axis wind turbine. *J. Fluid Science and Technology* **6** (6) 875.

YANG, B., & SHU, X.W. 2012 Hydrofoil optimization and experimental validation in helical vertical axis turbine for power generation from marine current. *Ocean Engineering* **42** 35.

Photo Credits

1. http://www.windspireenergy.com/
2. http://www.quietrevolution.com/qr5/gallery.htm
3. http://www.xconomy.com/san-diego/2012/08/22/in-a-requiem-for-helix-wind-critics-come-to-bury-more-than-praise/
4. http://redchalksketch.wordpress.com/category/architects/meejin-yoon-mystudio/

Appendix A: Derivation of Betz Limit

The Betz Limit is the theoretical efficiency limit for horizontal-axis wind turbines. If a wind turbine were to extract 100% of the wind's energy, the wind would be completely stopped, and the turbine would also be stopped. Thus, there must be some optimal conditions for maximum power extraction.

The following assumptions are made: the rotor is ideal (no hub, has infinite blades which have no resistance drag) and is a pure energy converter. The blades are modeled as an actuator disc, as shown in Figure A.1.

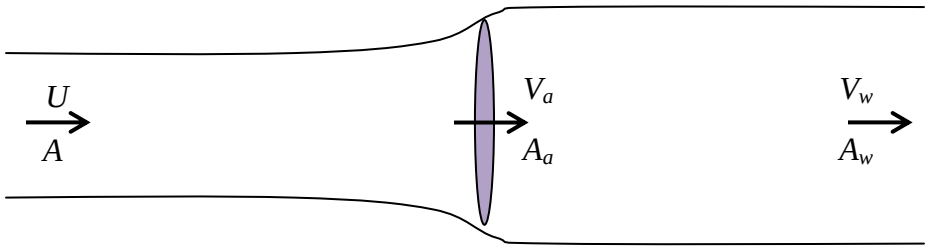

Figure A.1. Actuator Disc diagram

where U is the freestream velocity, V_a is the velocity through the actuator disc, and V_w is the velocity of the wake. V_a is assumed to be uniform throughout the area of the disc. A, A_a, and A_w are the corresponding areas of the three stations (upstream, at the actuator disc, and downstream in the wake).

The cross-sectional area increases from upstream to downstream of the turbine because in order for the turbine to extract energy, the wind energy and wind velocity must decrease. Thus: $V_w < U$. From mass continuity of an incompressible fluid:

$$UA = V_a A_a = V_w A_w \tag{A.1}$$

and thus $A_w > A$.

A relationship between the three velocities can be derived by analyzing the force and power of the system. The force exerted on the turbine by the wind is derived from a control volume analysis as follows:

$$F = \frac{d}{dt}(mV) = \dot{m}\frac{d}{dt}V$$

$$\boldsymbol{F = \rho A_a V_a (U - V_w)} \tag{A.2}$$

The power extracted by the actuator disc is:

$$P = FV = \rho A_a V_a (U - V_w) V_a$$

$$\boldsymbol{P = \rho A_a V_a^2 (U - V_w)} \tag{A.3}$$

This power can also be derived from the difference in kinetic energies between the upstream and downstream velocities as follows:

$$\mathrm{P} = rate\ of\ change\ of\ kinetic\ energy = \frac{d}{dt}\left(KE_{up} - KE_{down}\right)$$

$$= \frac{1}{2}\dot{m}(U^2 - V_w^2)$$

$$= \frac{1}{2}\rho A_a V_a U^2 - \frac{1}{2}\rho A_a V_a V_w^2$$

$$\mathbf{P} = \boldsymbol{\frac{1}{2}\rho A_a V_a (U^2 - V_w^2}} \tag{A.4}$$

Equating Equations A.3 and A.4 and simplifying gives an expression that relates the three velocities together, seen in Equation A.5 on the next page.

$$V_a = \frac{1}{2}(U + V_w) \tag{A.5}$$

This result can be used to get an expression for power as a function of U. Equation A.3 can be substituted for V_a in equation A.2 to give:

$$P = \frac{1}{4}\rho A_a(U^3 - UV_w^2 + U^2V_w - V_w^3) \tag{A.6}$$

Given the freestream velocity *U*, one finds that the power is only a function of V_w. By setting $dP/dV_w = 0$ (no variation in V_w), the maxima can be found as follows:

$$\frac{dP}{dV_w} = \frac{1}{4}\,\rho A\,(U^2 - 2UV_w - 3V_w^2) = 0$$

The solutions to the quadratic equation are:

$$V_w = \begin{cases} -U \\ \frac{1}{3}\,U \end{cases}$$

The solution V_w = -*U* has no physical meaning and can be ignored. The solution V_w = *1/3 U* indicates that the maximum power that can be achieved from the rotor occurs when the wake velocity is 1/3 of the freestream velocity *U*. Using this solution, an expression for power from Equation A.6 becomes:

$$P_{max} = 0.59\,\left(\frac{1}{2}\rho A_a U^3\right) \tag{A.7}$$

The coefficient of power is the ratio of power output to maximum available power in the wind. Thus:

$$C_P = \frac{P_{max}}{P_{wind}} = \frac{0.59\left(\frac{1}{2}\rho A_a U^3\right)}{\frac{1}{2}\rho A_a U^3}$$

$$C_P = 0.59 \tag{A.8}$$

The Betz limit of 0.59 is achieved. In essence, this shows that the maximum power available for energy extraction form the wind is 59% of the available wind power.

Appendix B: Wake Interference Model

The wake shed by one of the turbine blades creates a turbulent flow field and affects downstream blades. Understanding the interaction and interference of these wakes will help determine the best parameters for turbine design. This section does not provide a quantitative measure of wake interference, but does estimate when blade wake interaction might occur as the blades rotate.

Figure B.1 shows a Matlab graphical user interface which displays the wakes of each blade as the turbine rotates. The wake of the blade is represented as a series of points convecting downstream at the same speed as the freestream wind velocity. For large c/D ratios (where c is the chordlength of the blade and D is the diameter of the turbine), wake interference is high and blades are crossing into wakes as much as 2/3 of the time.

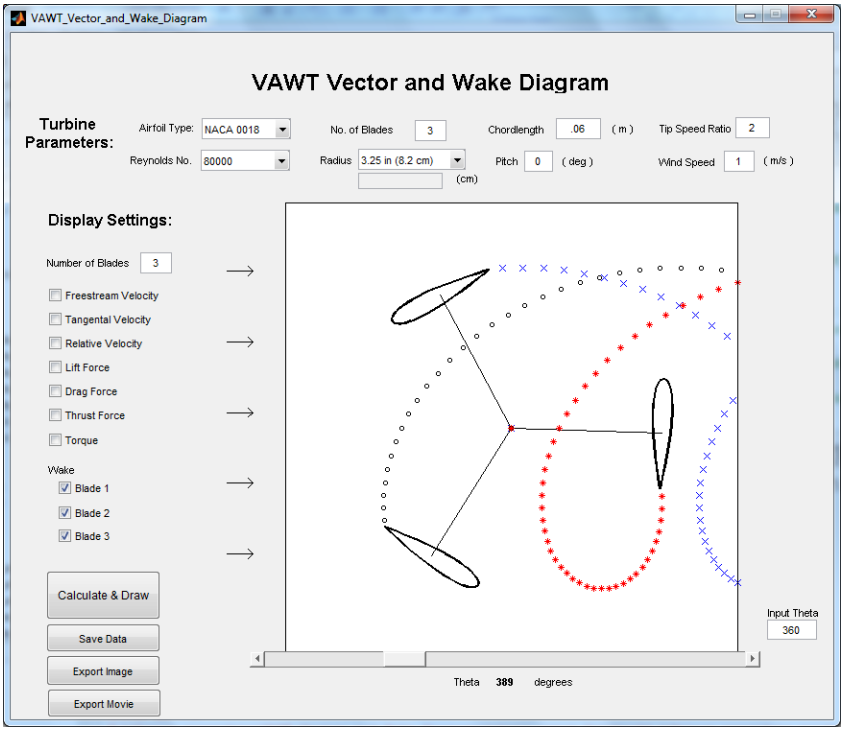

Figure B.1 Graphical User Interface for qualitative wake interference studies.

A two dimensional direct numerical simulation (DNS) of a VAWT was done by Dietmar Rempfer of the Illinois Institute of Technology (Rempfer, 2012). The simulation was done with the commercial code STAR-CCM+ with a chord Reynolds number of 50,000 and TSR = 2. The resultant vorticity plots are shown in Figure B.2 below, with the wind streaming from left to right. The blades produce a clean wake of the upper half of the rotation in the figures, but at high angles of attack and the lower parts of the trajectory they create large vortices which interact and merge into larger vortex structures. The blades pass through previous wakes for about half of the rotation.

The corresponding wake interference plots from our simple model are in Figure B.3. The parameters for the simulation are TSR = 2, chordlength = 0.0784 m, and diameter = 1.3m. The latter two parameters were derived by measuring c/D from the Rempfer's vorticity plots.

In Figure B.4, the $\theta = 0$ plots from the two simulations are superimposed for better comparison. Our simple wake model captures the same overall location of the wakes, especially the blue diamonds at TSR = 2. For reasons unknown, at TSR = 3.5, our simple wake model is a visual match to the DNS model (See Figure B.4b). This shows that, although we are neglecting vortex merging and interaction, we can still utilize our simple wake model as a rough sketch of the locations of shed wakes.

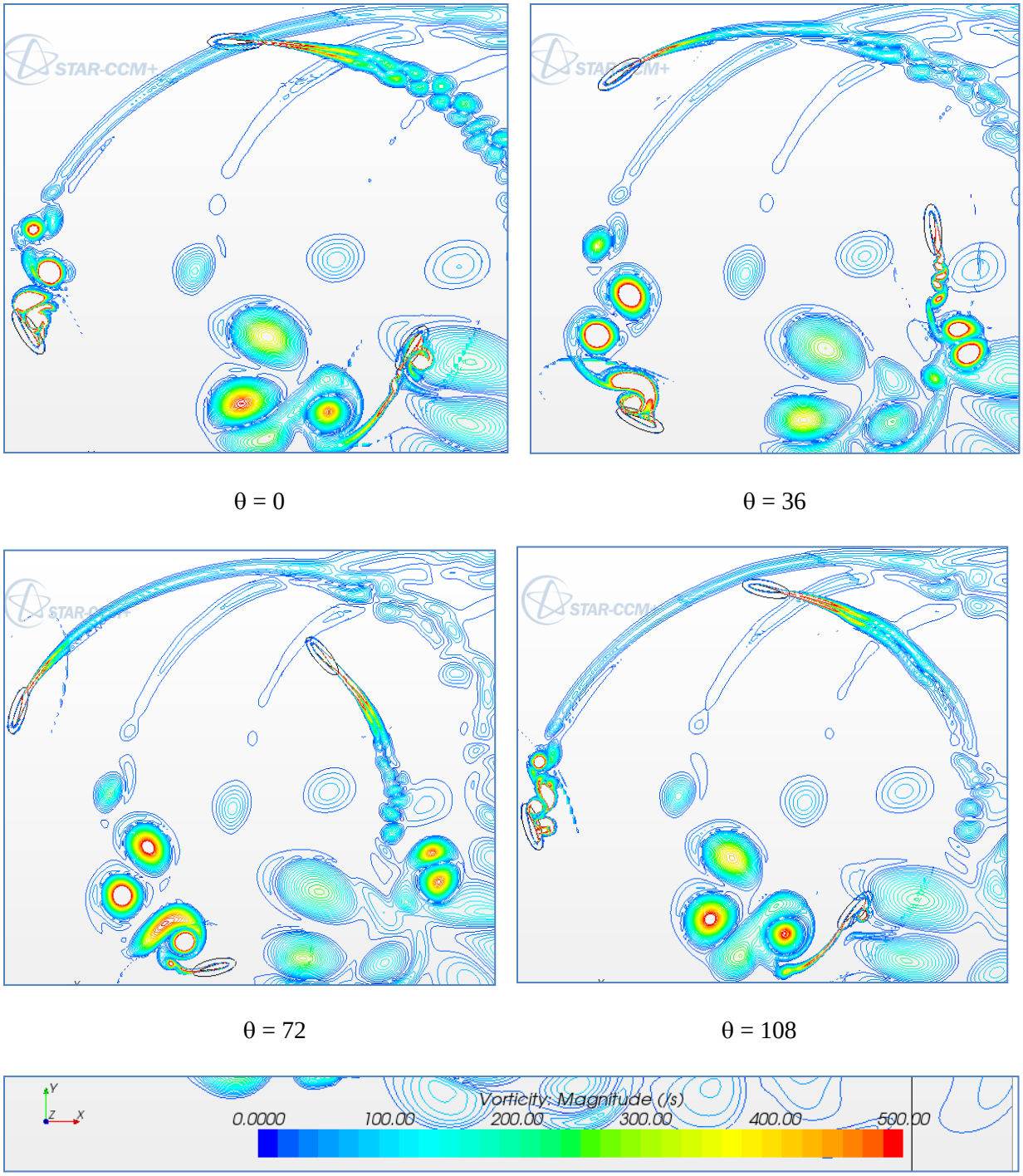

Figure B.2: Vorticity plot sequence of a VAWT (Rempfer, 2012)

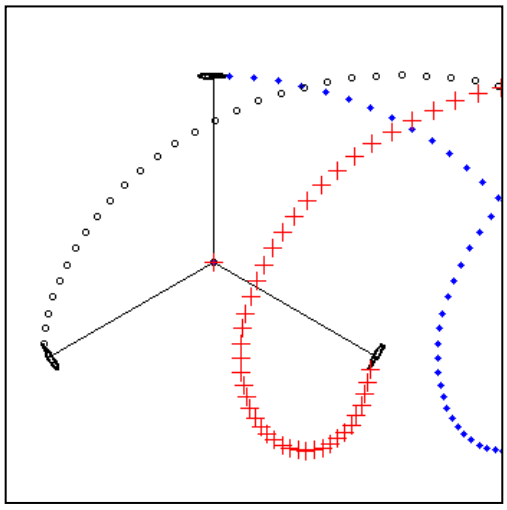

θ = 0

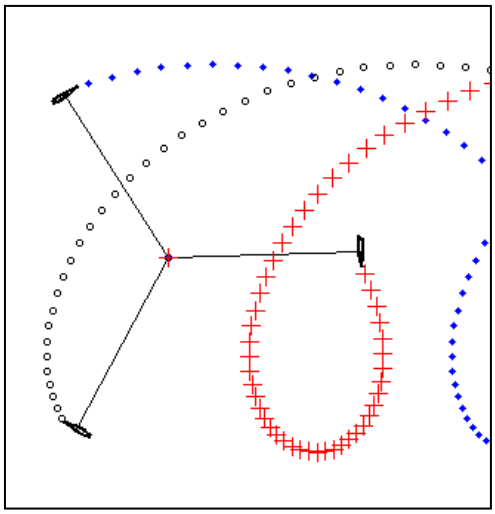

θ = 36

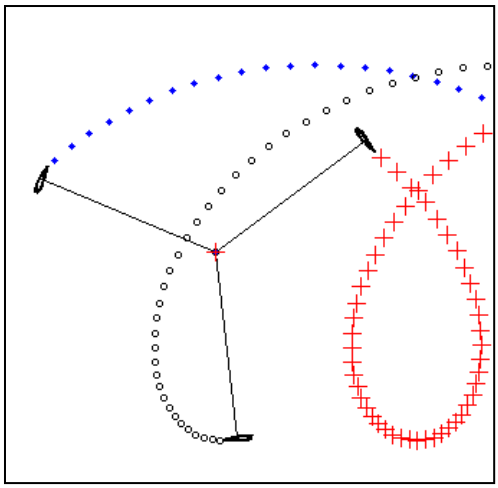

θ = 72

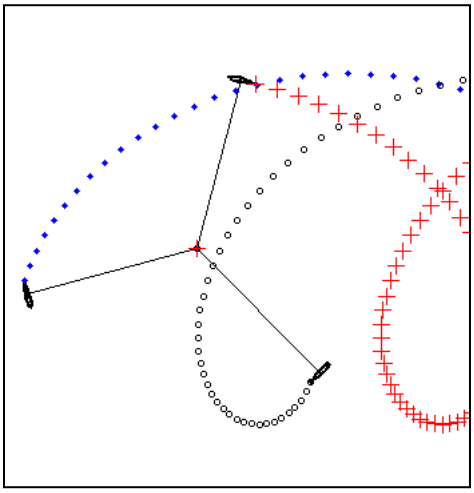

θ = 108

Figure B.3: Simple wake interference model sequence

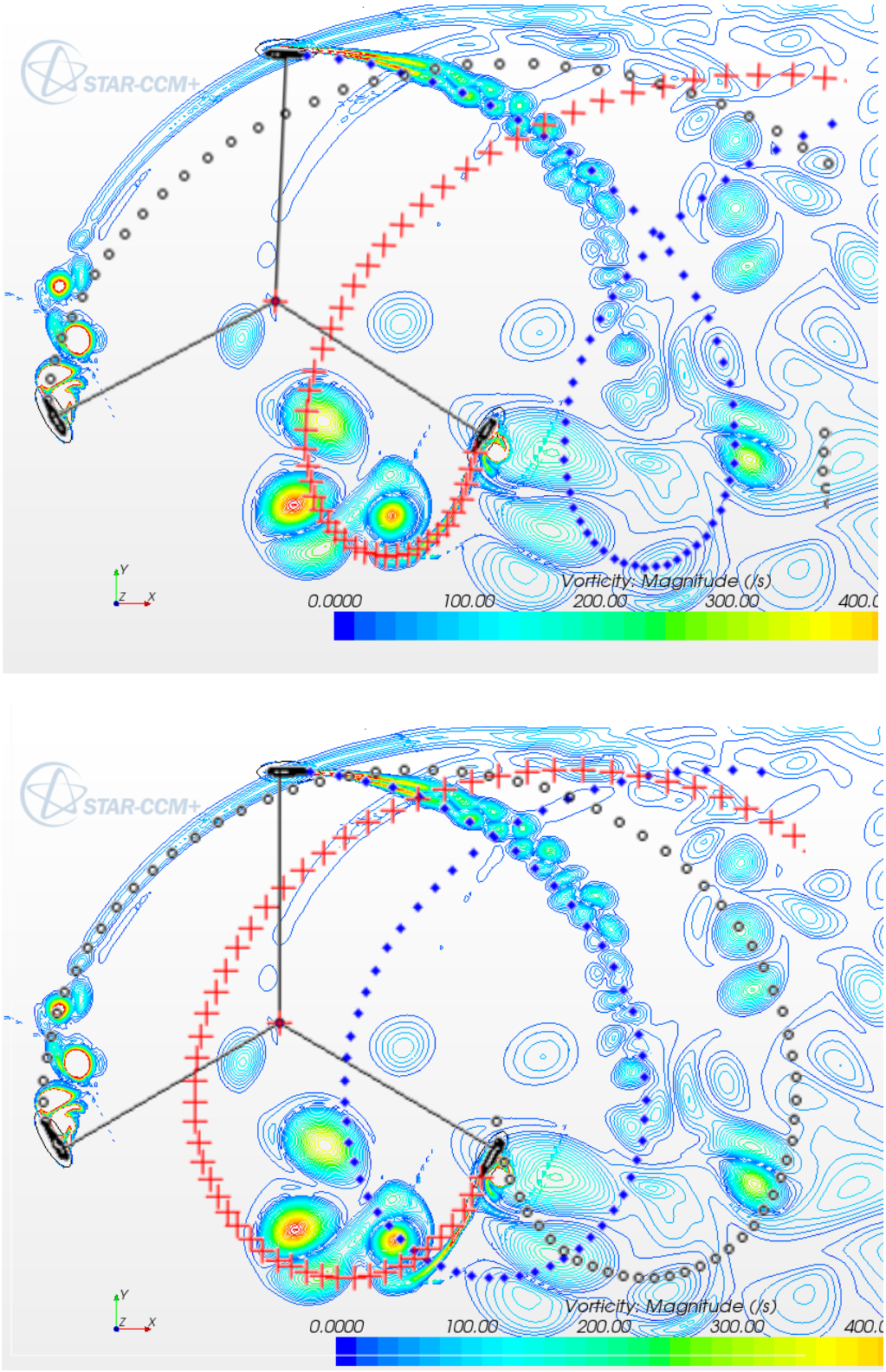

Figure B.4. (a) Two wake simulations superimposed at θ = 0. TSR = 2.0 **(b)** Two simulations are a visual match at TSR = 2 (Rempfer) and TSR = 3.5 (simple wake model)

The next step in understanding blade wake interference was to quantitatively mark the wake interference regions. Once the second model was verified with the first simple wake model, the results were combined with torque data in the form of polar plots of $T(\theta)$ or $C_P(\theta)$. This provides visualization of the locations where wake interference and high torque occur; optimal mini-turbines may be designed to prevent these two flow phenomena from occurring at the same locations.

The quantitative polar plot presentation uses a series of wake points convecting downstream in addition to torque and power values. The model calculates the positions of all three blades as a function of time. It also calculates the position of each wake point as a function of time. Using the point-slope-formula, a line segment is calculated between the blade's current position and the blade's next position in time. Similarly, a line segment is also calculated for each wake point position and the wake's next position in time. If the two line segments intersect, the location is recorded as an interference and plotted.

The results of the second wake interference code were verified against the qualitative diagrams of the old graphical user interface program. In Figure B.5, a sequence of diagrams produced by the old GUI program shows a blue airfoil (blade 1) passing through four distinct wake interference regions produced from the wakes of other two blades as well as its own wake, at TSR = 2. In comparison, Figure B.6 shows a polar diagram quantitatively showing the same four wake interference regions determined from the second code. The θ-axis of the polar graph is the same as the azimuth position angle of a blade and the shaded regions indicate where interference occurs. The radial-axis represents time and the points are locations of interference. Marker styles correspond to the blade where the wake originated and colors represent the location on the blade the wake intersected it. The colors range from blue to red, corresponding to

the leading edge of the blade to the trailing edge. These marker points help illustrate the time history of the system and create an image of how interference occurs. For example, it can be seen that two intersection regions do not occur until after the first revolution, once enough wakes have been produced and convected downstream.

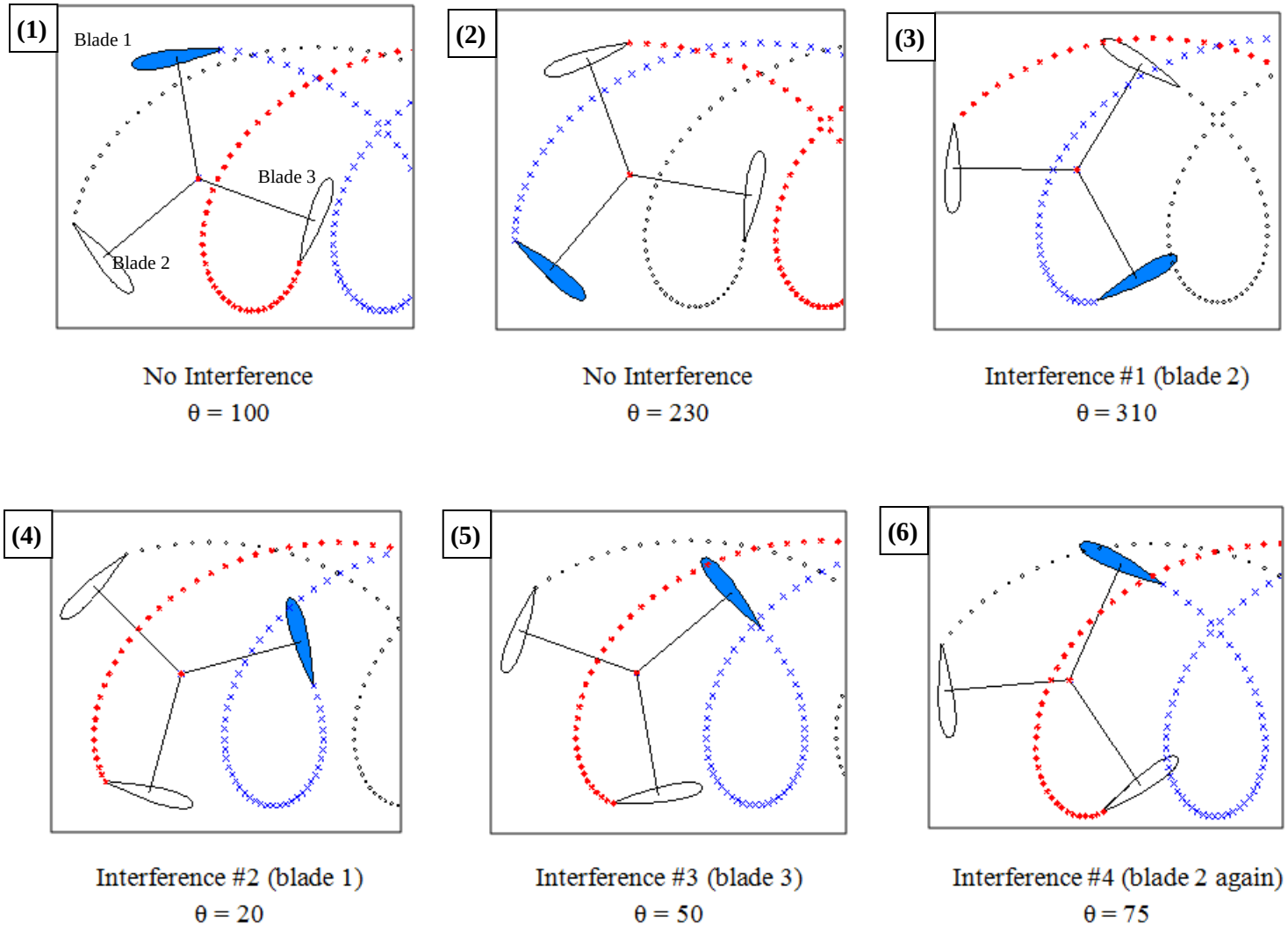

Figure B.5. Wake Interference Diagrams for TSR = 2. The blue airfoil passing through 4 distinct wake interference regions produced from the wakes of other blades as well as its own wake. In (1) and (2) the blue airfoil hits no wakes. In (3) it hits the wake formed from blade 2. In (4) it hits its own wake. (5) The airfoil goes through the wake formed by blade 3 and in (6) it hits the wake formed from blade 2 again.

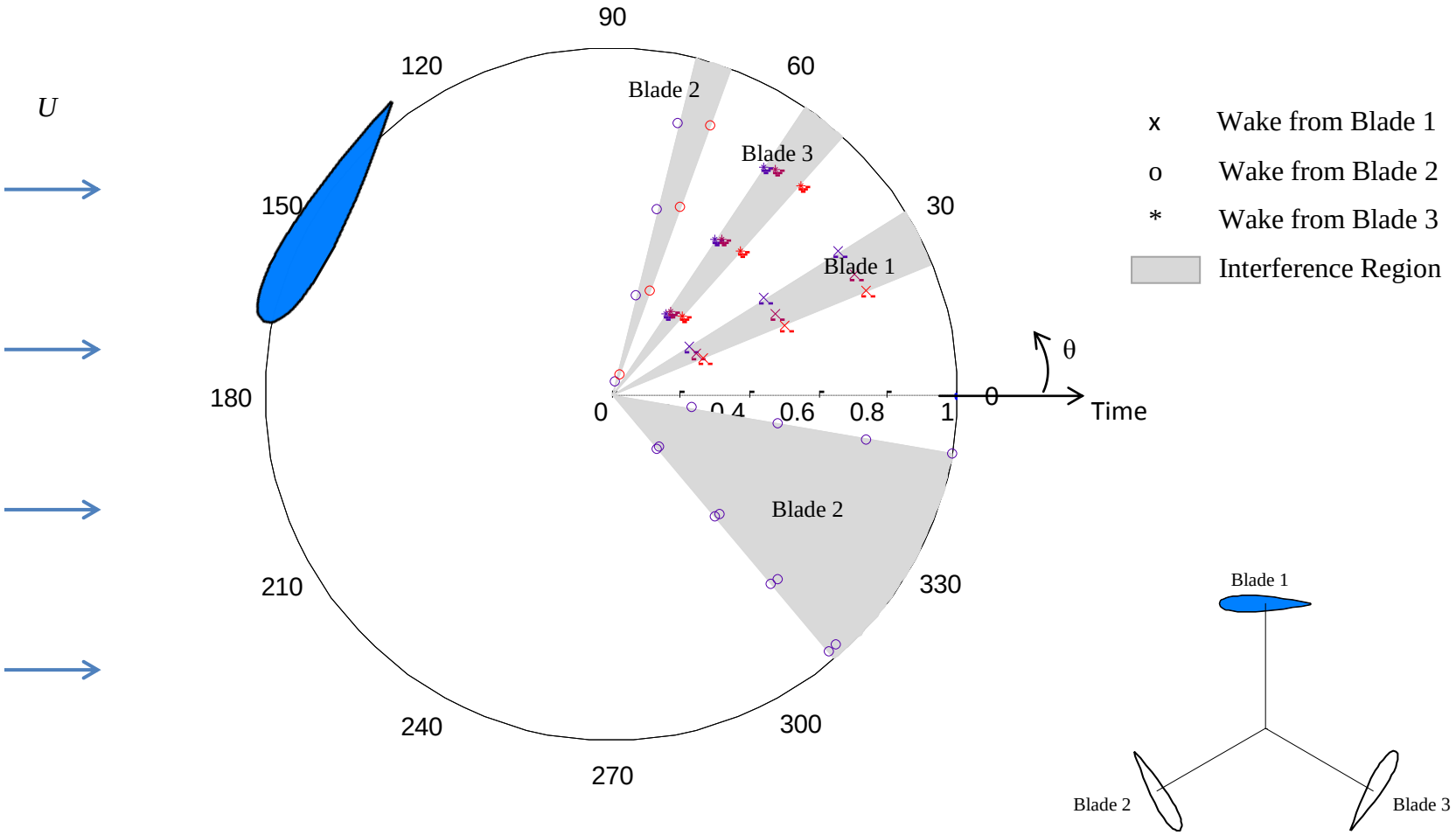

Figure B.6. Wake Interference Polar Diagram for a tip speed ratio of 2. This polar diagram quantitatively shows the 4 wake interference regions that the blue airfoil passes through. The radial axis is time, showing that two interference regions do not occur until after the first revolution. Blue pointsi correspond to the leading edge of the blade while red is the trailing edge.

Furthermore, the torque data can be added to the wake interference polar plots, as seen in Figure B.7a. There are two primary positive torque peaks located at the "top" of the blade trajectory, when the blade is moving into the freestream velocity. Figure B.7b shows that the peak torque values occur when the angle of attack of the blade is less than the static stall angle of 12 degrees, when there is high lift and low drag. The symmetry of the torque polar plots is also reflected in the angle of attack polar plot. Table B.1 below shows the simulation parameters used in polar plots to calculate the torque, angle of attack, and C_P.

Table B.1. Simulation parameters for polar power plots

Parameter Name	***Value Used***
Simulation Model	Freestream Analysis (No Streamtube)
Number of Blades	1
Airfoil Type	NACA 0018
Reynolds Number	80,000
Chordlength	6 cm
Turbine Diameter	16 cm
Pitch	0
Shear	0

For a given windspeed, tip speed ratio, and turbine geometry, the torque is proportional to the coefficient of power as follows:

$$C_P(\theta) = \frac{T(\theta) * \Omega}{\frac{1}{2}\rho U^3 A} = \frac{T(\theta) * \left(TSR\frac{U}{R}\right)}{\frac{1}{2}\rho U^3 DL}$$

$$C_P(\theta) \propto T(\theta)$$

Hence, the coefficient of power polar plot in Figure B.8 shows the same features as the torque polar plot in Figure B.7a but scaled differently. Wake interference regions in grey show that downstream positive Cp may be reduced by blade interference.

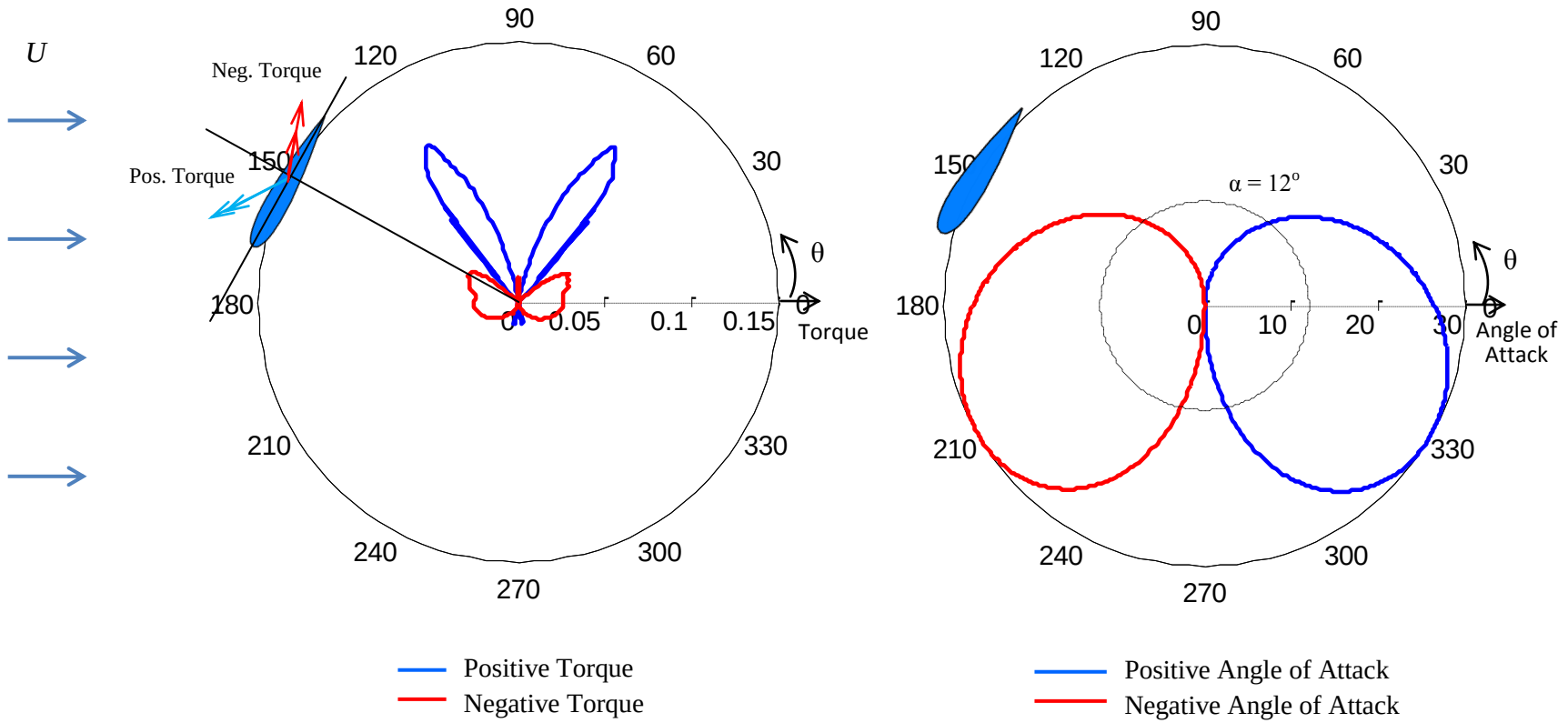

(a) Torque vs θ

(b) Angle of attack vs θ

Figure B.7 –Polar Plots of Torque vs θ and Angle of attack vs θ for one blade at TSR = 2. As expected, peak torque values occur when the angle of attack is less than the static stall angle of 12 degrees. Parameters: NACA 0018, Re 80,000, chord 6 cm, diameter 16 cm, 1 blade.

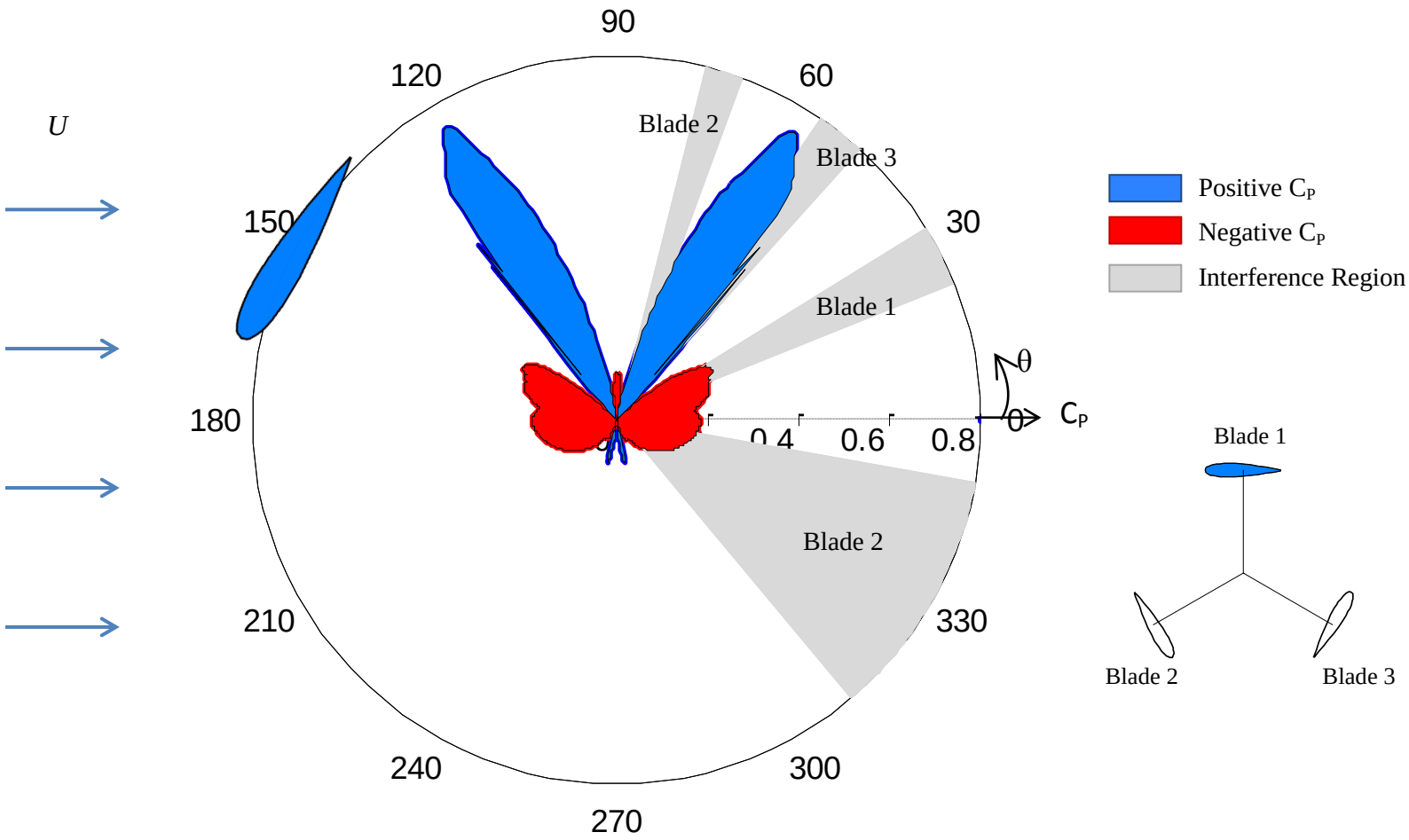

Figure B.8. Power Polar Plot: Cp vs θ values for one blade, at TSR = 2. $C_P(\theta)$ is proportional to T(θ) and the area within the curve is proportional to the total C_P of the turbine. Wake interference regions in grey show that downstream positive C_P may be reduced by blade interference. Parameters: NACA 0018, Re 80,000, chord 6 cm, diameter 16 cm.

In addition, the area within the C_P vs θ curve is proportional to the total average C_P as follows:

$$C_P = \frac{1}{2\pi}\int_0^{2\pi} C_p(\theta)\, d\theta = \frac{1}{2\pi}(Area\ Under\ Curve)$$

$$C_P \propto Area\ Under\ Curve$$

Thus, we can compare power polar plots of varying TSR in Figure B.9 by comparing the areas under the curves. Increasing TSR increases power performance while wake interference remains comparable; it is expected that downstream blade wake interference will reduce power. "Spikey" fluctuations in the power also occur, seen most noticeably in Figure B.9d at TSR = 4. Figure B.10 shows that these fluctuations occur when the blade passes through the static stall angle of 12 degrees. A lift coefficient plot shows that the lift is compromised for a few angles after stall before recovering into a "flat plate" regime (The flat plat regime is where the lift force increases as a function of angle of attack post-stall). Note that the average step size of the airfoil data used in the near pre- and post-stall angle is about 0.37, suggesting that the power fluctuations are due to the effect of stall and not poor airfoil data.

This wake interference study has given additional insights into the flow dynamics of mini-turbines. A more sophicated model could perhaps replace the simple wake points with point vortices representing wake vorticity. Furthermore, the model can be confirmed by placing a one-bladed mini-turbine in the towing tank or water channel and doing dye visualization. These findings can be incorporated into a new model to better design and predict the performance of mini-turbines.

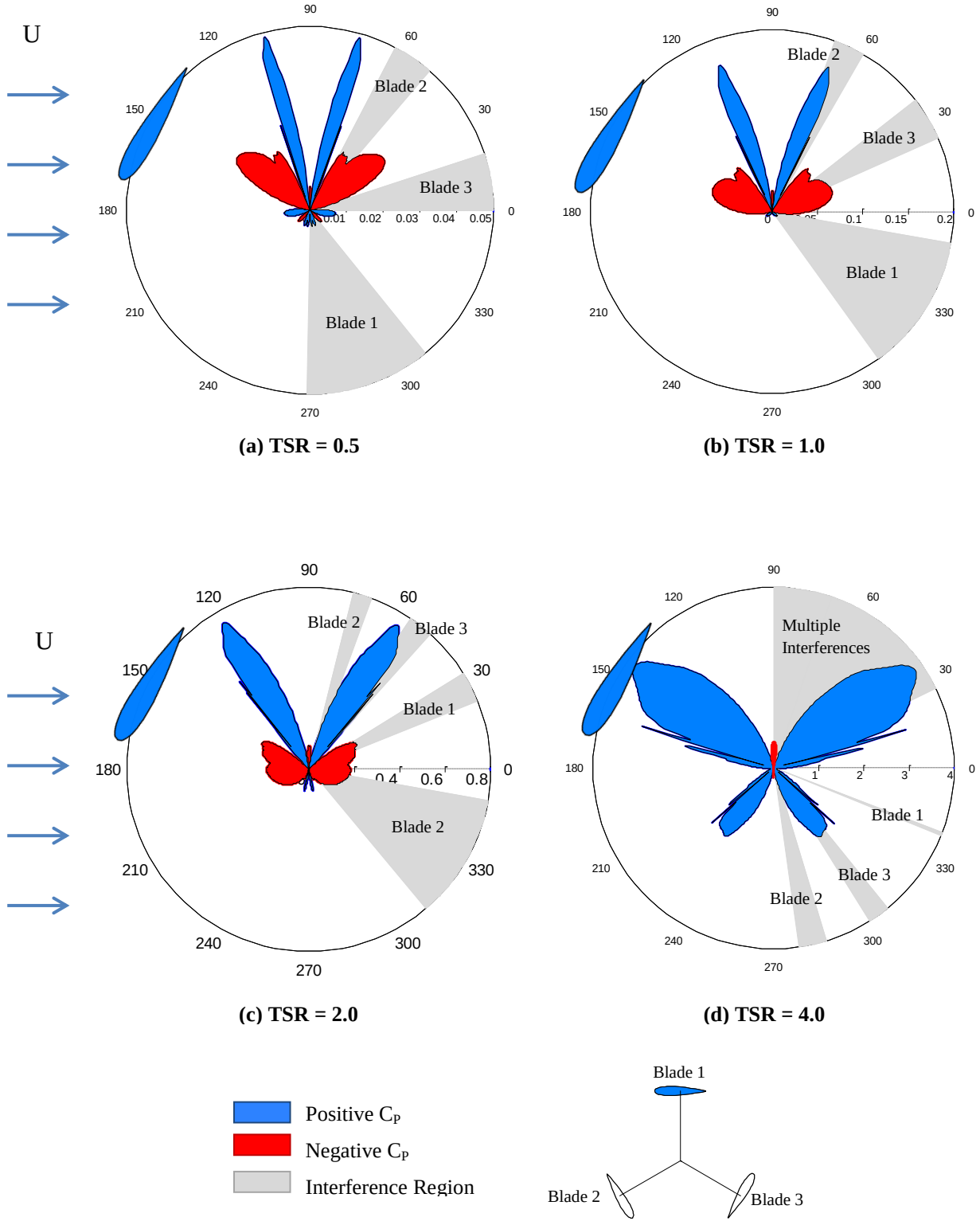

(a) TSR = 0.5

(b) TSR = 1.0

(c) TSR = 2.0

(d) TSR = 4.0

Figure B.9. **Power Polar Plot:** C_P vs θ values for one blade, at a range of TSRs. Area within the curve is proportional to the total C_P of the turbine. Increasing TSR increases performance while wake interference remains comparable. Parameters: NACA 0018, Re 80,000, chord 6 cm, diameter 16 cm.

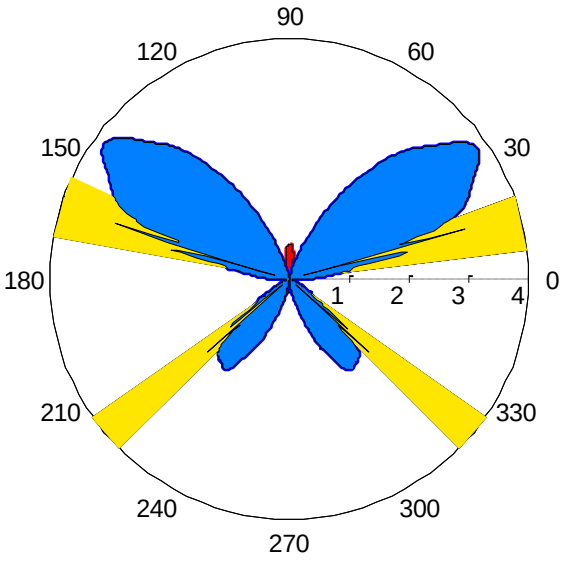

(a) Power Polar Plot for TSR = 4

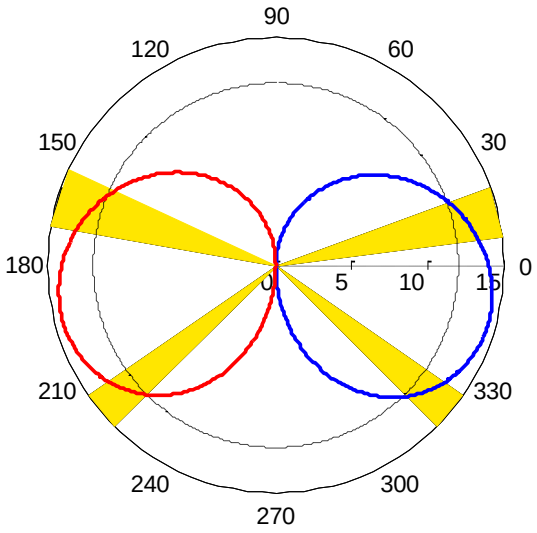

(b) Angle of Attack for TSR = 4

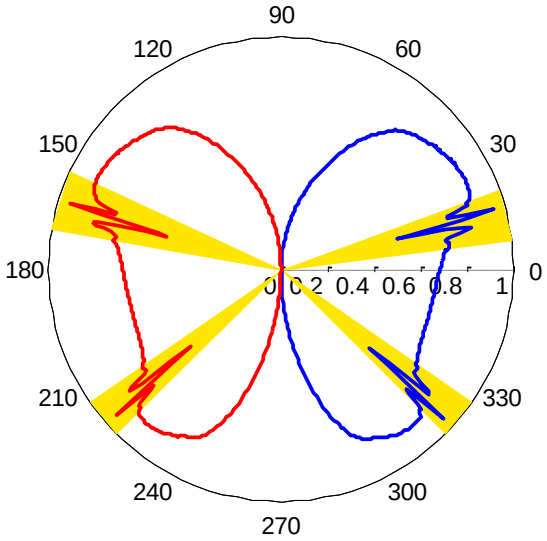

(c) Lift Coefficient vs θ for TSR = 4

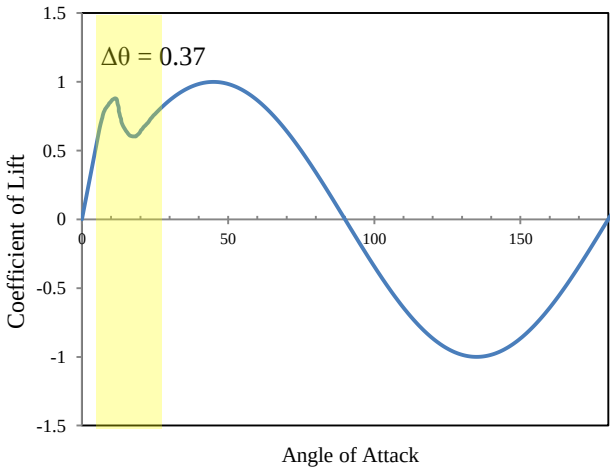

(d) Lift Coefficient vs Angle of Attack for NACA 0018, Re 80,000

Figure B.10 – Fluctuations in C_P polar plot due to the effect of stall. At TSR = 4, (a) C_P vs θ values for one blade (b) Angle of attack vs θ (c) C_L vs θ (d) C_L vs α airfoil data. C_P fluctuations correspond to locations where blade passes through stall (highlighted in yellow), decreasing lift, before recovering into flat plate regime. Note that the average step size of the airfoil data used in the near pre- and post-stall angle is about 0.37, suggesting that the power fluctuations are not due poor airfoil data. Parameters: NACA 0018, Re 80,000, chord 6 cm, diameter 16 cm.